2013

Theoretical And Computational Studies Of Diffusion Of Adatom Islands And Reactions Of Molecules On Surfaces

Syed Islamuddin Shah
University of Central Florida

THEORETICAL AND COMPUTATIONAL STUDIES OF DIFFUSION OF ADATOM ISLANDS AND REACTIONS OF MOLECULES ON SURFACES

by

SYED ISLAMUDDIN SHAH
M.Sc. Systems Engineering, Quaid-i-Azam University, Islamabad, Pakistan, 1998
M.Sc. Physics, Islamia University Bahawalpur, Pakistan, 1994

A dissertation submitted in partial fulfillment of the requirements
for the degree of Doctor of Philosophy
in the Department of Physics
in the College of Sciences
at the University of Central Florida
Orlando, Florida

Summer Term
2013

Major Professor: Talat S. Rahman

ABSTRACT

The work presented in this dissertation focuses on the study of post deposition spatial and temporal evolution of adatom islands and molecules on surfaces using *ab initio* and semiemperical methods. It is a microscopic study of the phenomena of diffusion and reaction on nanostructured surfaces for which we have developed appropriate computational tools, as well as implemented others that are available. To map out the potential energy surface on which the adatom islands and molecules move, we have carried out *ab initio* electronic structure calculations based on density functional theory (DFT) for selected systems. For others, we have relied on semiempirical interatomic potentials derived from the embedded atom method. To calculate the activation energy barriers, we have employed the "drag" method in most cases and verified its reliability by employing the more accurate nudged elastic band method for selected systems. Temporal and spatial evolution of the systems of interest have been calculated using the kinetic Monte Carlo (KMC), or the more accurate (complete) Self Learning kinetic Monte Carlo (SLKMC) method in the majority of cases, and *ab initio* molecular dynamics simulations in others. We have significantly enhanced the range of applicability of the SLKMC method by introducing a new pattern recognition scheme which by allowing occupancy of the "fcc" and "hcp" sites (and inclusion of "top" site in the pattern recognition as well) is capable of simulating the morphological evolution of

three dimensional adatom islands, a feature not feasible via the earlier - proposed SLKMC method.

Using SLKMC (which allows only fcc site occupancy on fcc(111) surface), our results of the coarsening of Ag islands on the Ag(111) surface show that during early stages, coarsening proceeds as a sequence of selected island sizes, creating peaks and valleys in the island-size distribution. This island size selectivity is independent of initial conditions and results from the formation of kinetically stable islands for certain sizes as dictated by the relative energetics of edge atom detachment/attachment processes together with the large activation barrier for kink detachment.

On applying the new method, SLKMC-II, to examine the self diffusion of small adatom islands (1-10 atoms) of Cu on Cu(111), Ag on Ag(111) and Ni on Ni(111), we find that for the case of Cu and Ni islands, diffusion is dominated by concerted processes (motion of island as a whole), whereas in the case of Ag, islands of size 2-9 atoms diffuse through concerted motion whereas the 10-atom island diffuses through single atom processes. Effective energy barriers for the self diffusion of these small Cu islands is 0.045 eV/atom, for Ni it is 0.060 eV/atom and for Ag it is 0.049 eV/atom, increasing almost linearly with island size.

Application of DFT based techniques have allowed us to address a few issues stemming from experimental observations on the effect of adsorbates such as CO on the structure

and stability of bimetallic systems (nanoparticles and surfaces). Total energy calculations of Ni-Au nanoparticles show Ni atoms to prefer to be in the interior of the nanoparticle. CO molecules, however, prefer to bind to a Ni atom if present on the surface. Using *ab initio* molecular dynamics simulations, we confirm that the presence of CO molecule induces diffusion of Ni atom from the core of the Ni-Au nanoparticle to its surface, making the nanoparticle more reactive. These results which help explain a set of experimental data are rationalized through charge transfer analysis.

Similar to the case of Ni-Au system, it is found that methoxy (CH_3O) may also induce diffusion of inner atoms to the surface on bimetallic Au-Pt systems. Our total energy DFT calculations show that it is more favorable for methoxy to bind to a Pt atom in the top Au layer than to a Au atom in Au-Pt system thereby explaining experimental observations.

To understand questions related to the dependence of product selectivity on ambient pressure for ammonia decomposition on $RuO_2(110)$, we have carried out an extensive calculation of the reaction pathways and energy barriers for a large number of intermediate products. On combining the reaction energetics from DFT, with KMC simulations, we show that under UHV conditions, selectivity switches from N_2 (~ 100 % selectivity) at T = 373K to NO at T = 630K, whereas under ambient conditions, N_2 is still the dominant product but maximum selectivity is only 60%. An analysis based on thermodynamics alone shows a contradiction between experimental data at UHV with those under ambient pressure. Our calculations of the reaction rates which are essential for KMC simulations removes this ap-

parent inconsistency and stresses the need to incorporate kinetics of processes in order to extract information on reaction selectivity.

to my brother

ACKNOWLEDGMENTS

I would like to thank my major advisor, Prof. Talat S. Rahman, for her assistance and support during this work. Her continuous guidance and perfectionist approach, always helped me to explore for better. I would also like to acknowledge her efforts for providing an atmosphere in which one can seek knowledge freely without strict obligations, and her trust and believe in each individuals effort. Her ever generous and understanding attitude always encouraged me and my family during our stay here.

I would like to thank Dr. Giridhar Nandipati for his guidance and help towards the completed and continuing projects related to SLKMC and Growth. I thank Dr. Abdelkader Kara for his friendship, support and guidance throughout this time. I would also like to thank Dr. Sampyo Hong, Dr. Volodymyr Turkowski, Dr. Duy Le who always helped me during my research in general and in particular for the projects i worked with them. I also thank to Dr. Alfredo, Dr. Sergey Stolbov and Marisol Alcntara Ortigoza.

I would also like to thank Professor Donna A. Chen at University of South Carolina, USA and Professor Pavel Jelinek of Institute of Physics of the AS CR, Prague, Czech Republic for their help and support during my collaborative work with them. I am also thankful to Dr. Oleg Trushin of Institute of Microelectronics and Informatics of Russian Academy of Sciences.

I thank my Committee members, Prof. Abdelkader kara, Prof. Patrick Schelling and Prof. Kevin Coffey for their time to evaluate this dissertation.

I would also like to thank my fellow group members Dr. Ahlam Al Rawi, Handan Yaldrim, Maral Aminpour, Alamgir Kabir, Neha Nayyar, Takat Rawal and Shree Ram for providing nice working environment and good time in and out of office.

I would like to express my appreciation to Prof. Lyman Baker for helping me to structure my sentences, correcting my mistakes and teaching how to write efficiently.

I feel obliged to express my gratitude towards my elementary teacher Syed Muhammad Nawaz, who inspired me throughout my educational career.

I also want to thank Dr. Muhmmad Salim who changed me completely, it is his continuous support and love, that i have achieved this goal.

I remember the passionate encouragement and contributions of my parents, brothers, and sisters throughout my life.

Most of all I am grateful to my wife Naima Saleem and my sons: Ayan, Muhammad and Taha for their love, patience, sacrifices and encouragement throughout this journey which meant the world to me.

TABLE OF CONTENTS

LIST OF FIGURES

LIST OF TABLES

CHAPTER 1
INTRODUCTION

Simulations of materials behavior are an important component of materials science research because information coming from experimental measurements are indirect and require theoretical analysis and interpretation. The first step in simulations is to find the interaction between the atoms and molecules that constitute the system. With the interactions in hand, one may determine the geometrical structure (configuration of all atoms) of the system through determination of the total energy as accurately as possible. For relatively small ($\backsim$ few hundred atoms) systems, an accurate method for the calculation of the electronic structure based on density functional theory (DFT) can be applied, while for larger systems semiempirical many body interaction potentials are computationally more efficient. Once the stable geometrical structure of the system is known, the spatial and temporal evolution of the system can be studied by methods like kinetic Monte Carlo (KMC) or molecular dynamics (MD).

In this thesis, the focus is on developing and implementing accurate and reliable computational techniques that enable understanding of dynamical phenomena such as atom-cluster (called adatom islands hereon) and molecular diffusion (and reaction) on solid surfaces. In the case of adatom islands the aim is to reveal the atomistic processes responsible for their diffusion as a function of island size, shape and composition. Furthermore, we want

to extract the role of these processes in early stages of island coarsening as a function of surface temperature. The long term goal of this project is to provide a set of descriptors for the diffusion of small two dimensional adatom islands on metal surfaces which eventually lead to the prediction of surface morphological evolution. Clearly, diffusion of these islands proceeds through a number of competing processes whose kinetics and energetics together control their relative importance. These and related studies are critical for a systematic understanding of thin film growth processes, for which much proceeds to date through trial and error.

As in the case of adatom islands, we are also interested in examining the pathways for diffusion and, ultimately, for chemical reaction of molecules on surfaces. Here also there is the need to implement/develop techniques which allow competing processes to proceed naturally under ultra high vacuum (UHV) on ambient conditions, as a function of temperature and pressure which depict laboratory conditions. In this thesis, we will use a combination of theoretical and computational techniques to address the two sets of problems mentioned above: adatom island diffusion, and molecular adsorption, desorption and reaction on solid surfaces. While the choice of the specific technique is driven by its feasibility and validity for the issue at hand, the specific systems that we study are motivated by experimental observations in the laboratories of our collaborators, particularly Professor Chen's group at University of South Carolina and Professor Ertl's group at the Fritz Haber Institute in Berlin.

Of particular relevance to this thesis is the KMC technique [2–7] which is extremely efficient for carrying out dynamical simulations of a wide variety of stochastic and/or thermally activated processes when the relevant atomic-scale processes are known. In standard KMC, rates of allowed processes, through which the system evolves, are provided as an input. If this input is accurate and complete, KMC simulations will give accurate results. Standard KMC simulations are performed with a set of preconceived single atom or concerted (motion of all atoms) processes as input, and all others are ignored or included in approximate ways. For these reasons and also because of experimental observations of complex and unforeseen processes, *a priori* chosen catalog (lack of completeness) of process needs to be replaced by a continuous identification of possible processes during the course of simulations, as the environment changes.

To overcome above mentioned issues, various schemes were introduced into the KMC method [8, 9], including the Self Learning KMC (SLKMC) method[10] which employs a pattern-recognition scheme that allows on-the-fly identification, storage and retrieval of information about diffusion processes based on the local neighborhood of each active (undercoordinated) atom, consequently speeding up simulations by several orders of magnitude as well as making it more reliable and complete. As will be discussed in chapter 3, the SLKMC method was used to generate the database for the diffusion of Ag islands consisting 1-19 atoms and larger on Ag(111) [11]. We have performed KMC simulations with this database to examine the coarsening of deposited Ag adatom islands on Ag(111) (chapter 3). Our

results show the growth of larger islands at the expense of smaller islands. It also points to the relative stability of certain island size in the initial stages.

On the fcc(111) surface, however, there are two types of threefold adsorption sites: the normal fcc site and the fault hcp site. The pattern recognition scheme used in previous studies[1, 10–12] for fcc(111) surface was restricted to the occupation of fcc sites only and hence was unable to account for processes that involve movement of atoms to or from hcp sites [13, 14]. We have developed a pattern-recognition scheme that does allow occupation of fcc, hcp and also the top sites in order to uniquely identify environment of an atom in 2-D as well as 3-D systems, as we shall see in chapter 4.

We have applied SLKMC-II to study the self-diffusion of small islands (containing 1-10 atoms) of Ni on Ni(111), Ag on Ag(111) and Cu on Cu(111), as elaborated in chapter 5. We find that for the case of Cu and Ni islands diffusion is mainly dominated by the concerted processes for islands of size 1-10 atoms, whereas in the case of Ag, islands of size 2-9 diffuse through concerted processes while the 10-atom island diffuse mostly through single atom processes. Effective energy barriers for these small islands increase almost linearly with island size.

For the second project in which the focus is on the diffusion and reaction of molecules on catalytic surfaces, we need to employ techniques which provide an accurate description of bonds at the nanoscale. *Ab initio* electronic structure calculations are thus essential as

they provide a detailed understanding of the nature of bonding between molecules adsorbed on a surface (adsorbates) and of the adsorbate with the surface: a fundamental step in the study of heterogeneous catalysis. As for many chemical reactions, thermodynamically favorable reaction suffers by large activation barrier associated with intermediate/final product. Therefore increasing the reaction rate by introduction of a catalyst is of enormous technological importance. One of the impacts of the catalyst is to influence the adsorption of the adsorbate resulting in weakening of adsorbate bonds to reduce the activation barriers (or brings in the thermodynamic favorability) involved during different stages of the chemical reaction. In this thesis, we have included results of our examination of the adsorption, desorption, diffusion and reaction of molecules such as CO and CH_3OH on bimetallic surfaces and of NH_3 on $RuO_2(110)$, in connection with issues raised in related experimental studies.

We present in chapter 6 using total energy DFT calculations and *ab initio* molecular dynamics simulations, the effect of adsorbate (in this case CO molecule) on the bimetallic cluster (Ni-Au). Our results agree with experimental findings [15] that in the absence of adsorbates, Ni atoms prefers to be in the core of the bimetallic clusters. On the other hand, the energetically favorable configuration for CO adsorption is on top of Ni atoms at the surface of the bimetallic cluster. We show from *ab initio* molecular dynamics simulations that in the presence of the CO molecule on the the surface of bimetallic cluster, Ni atoms diffuse to the surface.

The above results raise the question: do molecules such as methanol (CH_3OH) or its product methoxy (CH_3O) cause Pt atoms in Pt-Au nanoclusters to also diffuse to the surface. A positive answer would rationalize experimental observations. However, as we show in section 6.4, on the basis of total energy calculations and reaction energetics from DFT, CH_3O may cause diffusion of Pt atoms to the surface in Pt-Au nanoclusters. We also map out the reaction barriers for the dissociation of CH_3O to CO to provide guidelines for conditions under which Pt atom may diffuse to the surface of the bimetallic system.

Conclusions based on reaction energetics alone can be made for very simple systems discussed above, where as in reality there are many reaction pathways along with rates of different time scales. Also, due to the fact that each process may also have different prefactor, situation becomes even more complex and simple analysis of reaction energetics cannot provide information about competing rates of reactions. MD simulations can not be used either because of the long time scales of the different reaction processes involved. One way to predict the long time behavior of the competing events is to use KMC simulations. In chapter 7, we present a detailed analysis of the selectivity in ammonia oxidation on $RuO_2O(110)$ surface on which a recent experimental finding [16], carried out under ambient pressures, has raised some issues about a prior finding of high product (NO vs N_2) selectivity in UHV [17, 18].

Using activation barriers and prefactors (for some of the processes, for others we use standard prefactor) from DFT, in chapter 7, we present results for DFT + KMC study of

NH_3 oxidation on $RuO_2(110)$ in UHV and ambient conditions and provide a good rationale for both sets of experimental observations.

This dissertation is organized as follows.

In chapter 2, some general details of theoretical methods are presented.

In Chapter 3 (taken from Ref [12]), we have shown that during early stages of Ag island coarsening on Ag(111), coarsening proceeds as a sequence of selected island sizes, creating peaks and valleys in the island-size distribution (ISD). This island-size selectivity is independent of initial conditions and results from the formation of kinetically stable islands for certain sizes as dictated by the relative energetics of edge atom detachment/attachment processes together with the large activation barrier for kink detachment.

Chapter 4 (taken from Ref [19]) provides details of Extended pattern recognition scheme that takes into account both fcc and hcp adsorption sites in performing self-learning kinetic Monte Carlo (SLKMC-II) simulations on the fcc(111) surface. In this scheme, the local environment of every under-coordinated atom in an island is uniquely identified by grouping fcc sites, hcp sites and top-layer substrate atoms around it into hexagonal rings. Using this pattern recognition scheme, all possible processes, including those such as shearing, reptation and concerted gliding, which may involve fccfcc, hcphcp and fcchcp moves are automatically found, and their energetics calculated on the fly. We apply this new pattern

recognition scheme to the self-diffusion of 9-atom islands (M9) on M(111), where M = Cu, Ag or Ni.

In chapter 5 on self-diffusion of small clusters on the fcc(111) surface, we found that, in the temperature range of 300 K 700 K, small islands of Cu/Cu(111), Ag/Ag(111) and Ni/Ni(111) surface diffuse primarily via concerted motion. In these islands, single-atom processes play an important role in ensuring that diffusion is random for islands containing 5 or more atoms, while multiatom processes (shearing and reptation) come into play for noncompact islands. Results on small Ni islands diffusion on Ni(111) surface in Chapter 5 are from Ref [20].

Chapter 6 is dedicated to the density functional theory based calculation of the adsorption of molecules on bimetallic systems. In section 6.3 (adapted from Ref [15]), it is shown that in unsupported Ni_1Au_{121} clusters, in the presence of CO molecule, the lowest energy structure involves CO bonded to a Ni atom at the surface. In contrast, in the absence of CO, the most stable cluster surface is pure Au with all of the Ni atoms in the interior of the cluster. Ab initio molecular dynamics simulations show that Ni will migrate to the cluster surface at 300 K in the presence of CO, but Ni migration to the surface does not occur even at higher temperatures in the absence of CO from density functional theory calculations. In section 6.4, it is shown from total energy calculations, that presence of CH_3O on the surface of AuPt(111) surface may induce diffusion of Pt atom from the sub-surface

layers of AuPt(111) to its surface. Section 6.4.2 describes the decomposition of CH_3O to CO on Au12Pt1 nano-cluster.

Finally in chapter 7, our DFT+KMC results for ammonia oxidation on $RuO_2(110)$ show that NO is the dominant product in UHV conditions at or above the peak NO desorption temperature whereas in ambient conditions N_2 is the dominant product.

CHAPTER 2
THEORETICAL BACKGROUND

Accuracy of atomistic simulations rely on how accurately the interatomic forces between the constituents of the system under study are represented. These forces determine the potential energy surface that control the energetics and dynamics of phenomena such as diffusion, adsorption, desorption and chemical reaction. The first step in any calculation is the determination of the most stable geometric structure i.e. the positions of the ion cores of all atoms in the model system. For this purpose we calculate the total energy of the system and through ionic relaxation determine the configuration with the lowest total energy. In the work here we have used a combination of density functional theory [21] and semiempirical interaction potentials from the embedded atom method [22] to calculate the system total energy. Below we provide some details of these two techniques.

2.1 Methods for Determining the Total Energy

2.1.1 Density Functional Theory

The main goal of most approaches in solid state physics and quantum chemistry is the solution of the time-independent, non-relativistic Schrödinger equation:

$$\hat{H}\Psi_i(\vec{x_1}, \vec{x_2}, ..., \vec{x_N}, \vec{R_1}, \vec{R_2}, ..., \vec{R_M}) = E_i\Psi_i(\vec{x_1}, \vec{x_2}, ..., \vec{x_N}, \vec{R_1}, \vec{R_2}, ..., \vec{R_M}) \tag{2.1}$$

where $\hat{H}$ (Eq 2.1) is the Hamiltonian for a system consisting of N electrons and M nuclei.

$$\hat{H} = -\frac{1}{2}\sum_{i=1}^{N}\nabla_i^2 - \frac{1}{2}\sum_{A=1}^{M}\frac{1}{M_A}\nabla_A^2 - \sum_{i=1}^{N}\sum_{A=1}^{M}\frac{Z_A}{\vec{x_{iA}}} + \sum_{i=1}^{N}\sum_{j>i}^{N}\frac{1}{\vec{x_{ij}}} + \sum_{A=1}^{M}\sum_{B>A}^{M}\frac{Z_A Z_B}{R_{AB}}. \tag{2.2}$$

The first two terms on the R.H.S of Equ. 2.2 describe the kinetic energy of the electrons and nuclei respectively. Third term is the electron-nuclei interaction and the last two terms represent the electron-electron and ion-ion repulsion respectively.

As Eq 2.1 is many body equation with 3N+3M coupled degrees of freedom, it is very impossible to solve exactly. Owing to the fact that nuclei are much heavier that electrons by Born-Oppenheimer approximation, Eq 2.2 can be written as set of equations with electronic Hamiltonian as:

$$\hat{H}_e = -\frac{1}{2}\sum_{i=1}^{N}\nabla_i^2 - \sum_{i=1}^{N}\sum_{A=1}^{M}\frac{Z_A}{\vec{x_{iA}}} + \sum_{i=1}^{N}\sum_{j>i}^{N}\frac{1}{\vec{x_{ij}}} \tag{2.3}$$

and its solution as:

$$\hat{H}_e\Psi_e = E_e\Psi_e \tag{2.4}$$

Hence total energy E_t of the system is given by:

$$E_t = E_e + E_{nuc} \tag{2.5}$$

where

$$E_{nuc} = \sum_{A=1}^{M} \sum_{B>A}^{M} \frac{Z_A Z_B}{R_{AB}} \tag{2.6}$$

Note that the nuclear kinetic energy term in Eq 2.2 is considered to be zero.

Eq 2.4 is still an N-particles equation with 3N degrees of freedom, which is also difficult to solve. To overcome this problem, the independent electron approximation (Hartree approximation [23]) may be invoked which states that the electrons interact via a mean-field Coulomb potential. The many-body wave function can now be written as:

$$\Psi(\vec{x_1}, \vec{x_2}, ..., \vec{x_N}) = \Psi_1(\vec{x_1})\Psi_2(\vec{x_2})...\Psi_N(\vec{x_n}) \tag{2.7}$$

The resulting one electron Schrödinger equation is given by:

$$-\frac{1}{2}\nabla^2\Psi_i(\vec{x}) + V(\vec{x})\Psi_i(\vec{x}) = \epsilon_i\Psi_i(\vec{x}) \tag{2.8}$$

where V($\vec{x}$) is the nuclear-electron interaction given by:

$$V_{nucleus}(\vec{x}) = -e^2 \sum_R \frac{1}{\mid \vec{x} - \vec{R} \mid} \tag{2.9}$$

and mean field arising from the N-1 other electrons, with a potential of the form:

$$V_{electron}(\vec{x}) = -e \int d\vec{x'} \rho(\vec{x'}) \frac{1}{\mid \vec{x} - \vec{x'} \mid} \tag{2.10}$$

where

$$\rho(\vec{x}) = \sum_i \mid \Psi(\vec{x}) \mid^2 \tag{2.11}$$

Next, from Pauli exclusion principle, we know that the many-body wave function for fermions must be antisymmetric with respect to interchange of any two electrons. This particle exchange condition is satisfied by forming a Slater determinant [24] of single-particle orbitals as:

$$\Psi(\vec{x_1}, \vec{x_2}, ..., \vec{x_N}) = \frac{1}{\sqrt{N}} \acute{A} \mid \Psi_1(\vec{x_1}) \Psi_2(\vec{x_2}) ... \Psi_N(\vec{x_n}) \mid \tag{2.12}$$

where $\acute{A}$ is the anti-symmetry operator. This leads to Hartree-Fock [25] equation of the form:

$$-\frac{1}{2}\nabla^2 \Psi_i(\vec{x}) + V_{nucleus}(\vec{x})\Psi_i(\vec{x}) + V_{electron}(\vec{x})\Psi_i(\vec{x}) - \sum_j \int d\vec{x'} \frac{\Psi_j^*(\vec{x'})\psi_i^*(\vec{x'})\psi_j(\vec{x})}{\mid \vec{x} - \vec{x'} \mid} = \epsilon_i \Psi_i(\vec{x}) \tag{2.13}$$

The Hartree-Fock equations describes exchange exactly; but correlations due to many-body interactions are neglected. The theory which successfully incorporates the effects of exchange and correlation is the density functional theory (DFT).

In DFT, the electron density, rather than the many-body wave function, is the central variable. This leads to a reduction in complexity: the density is a function of three variables rather than the 3N variables of the many-body wave function.

An early version of DFT proposed by Thomas and Fermi [26, 27] assumes the kinetic energy to be a functional of the electron density, but electron-electron interactions are treated via a mean field potential and it neglects both exchange and correlation. On the other hand, Dirac [28], suggested an expression for the exchange energy in terms of the electron density but failed to significantly improve the method.

The most successful DFT, routinely applied in electronic structure theory calculations, ranging from quantum chemistry and condensed matter physics is based upon the following theorems by Hohenberg and Kohn [21]:

2.1.1.1 Hohenberg-Kohn Theorems

The first theorem states that: The external potential is a unique functional of the electron density only. Thus the Hamiltonian, and hence all ground state properties, are determined solely by the electron density.

And second theorem says that: The ground state energy may be obtained variationally: the density that minimizes the total energy is the exact ground state density.

2.1.1.2 The Kohn-Sham Equation

The Kohn-Sham formulation maps the full interacting system with the real potential, onto a fictitious non-interacting system whereby the electrons move within an effective "Kohn-Sham" single-particle potential. In Kohn-Sham formalism, total energy of the ground state of a system of N interacting electrons in a external field is given as:

$$E_0[\rho(\vec{r})] = T[\rho(\vec{r})] + V[\rho(\vec{r})] + E_{ee}[\rho(\vec{r})] \tag{2.14}$$

$\rho(\vec{r})$ being electron density of the system. The potential energy V$[\rho(\vec{r})]$ is given by:

$$V[\rho(\vec{r})] = \int \rho(\vec{r}) V_{ext}(\vec{r}) d\vec{r} \tag{2.15}$$

Replacing the kinetic energy T$[\rho(\vec{r})]$ of the system of N interacting electron with that of N non-interacting electrons with the same electron density $\rho(\vec{r})$, and replacing the electron-electron interaction energy E$_{ee}[\rho(\vec{r})]$ with the electron-electron interaction energy, the total energy can be written as:

$$E_0[\rho(\vec{r})] = T_{KS}[\rho(\vec{r})] + E_H[\rho(\vec{r}) + V[\rho(\vec{r})] + E_{XC}[\rho(\vec{r})] \tag{2.16}$$

where

$$T_{KS}[\rho(\vec{r})] = -\frac{1}{2}\sum_{i=1}^{N} < \phi_i \mid \Delta_i^2 \mid \phi_i > \tag{2.17}$$

and

$$E_H[\rho(\vec{r})] = -\frac{1}{2}\int\int \frac{\rho(\vec{r_1})\rho(\vec{r_2})}{\mid \vec{r_1} - \vec{r_2} \mid} d\vec{r_1} d\vec{r_2} \tag{2.18}$$

and $\mathrm{E}_{XC}[\rho(\vec{r})]$ is the exchange-correlation energy.

The resulting effective external filed $\mathrm{V}_{ext}^{eff}(\vec{r})$ is given by:

$$V_{ext}^{eff}(\vec{r}) = V_{ext}(\vec{r}) + V_H[\rho(\vec{r})] + V_{XC}[\rho(\vec{r})] \tag{2.19}$$

The resulting Schröndinger equation (Kohn-Sham equation) is:

$$[-\frac{1}{2}\nabla^2 + V_{ext}^{eff}(\vec{r})]\phi_i = \epsilon_i \phi_i. \tag{2.20}$$

The solution of Eq. 2.20 are the Kohn-Sham orbitals (ϕ_i) and Kohn-Sham eigenvalues (ϵ_i) of the Kohn-Sham quasi-particles. Knowing the exchange-correlation functional $\mathrm{E}_{XC}[\rho(\vec{r})]$, the single particle Kohn-Sham equations can be solved iteratively.

Density functional theory based approaches are computationally expensive and are suitable only for small systems involving couple of hundreds of atoms and only for short time scale applications.

2.1.2 Embedded Atom Method (EAM)

In order to be able to find the energetics of system, the total energy of the system must be known for an arbitrary arrangement of the atoms. A simple description of the total energy of the solid can be treated as the sum of pair interactions between the atoms. While this approximation is useful in many cases, it has certain shortcomings. The EAM is an attempt to provide a new method of determining the total energy that is computationally simple like the pair interaction approach.

In EAM formalism, the total energy of an arbitrary arrangement of atoms can be written as a unique functional of the total electron density. The starting point of the embedded atom method is the observation that the total electron density in the vicinity of a given atom can be thought of as the electron density of the atom in question plus a background electron density contributed by the surrounding atoms. The contribution to the total electron density, from the surrounding atoms is a slowly varying function of position, and so it is reasonable to approximate this contribution to the local electron density by a constant. The energy of this atom can then be approximated by the energy associated with the electron density of the atom plus this constant background density. This defines an embedding

energy for that atomic species as a function of the background electron density. There is an additional electrostatic energy contribution due to core-core overlap. These ideas have been developed by Daw and Baskes [22, 29], who show that the total energy of a system can be written approximately as:

$$E_t = \sum_i F_i(\rho_i(r_i)) + \frac{1}{2}\sum_{i,j} \Phi(r_{i,j}) \tag{2.21}$$

Here total energy of an atom i is given by:

$$E_i = F_i(\rho_i(r_i)) + \frac{1}{2}\sum_{j} \Phi(r_{i,j}) \tag{2.22}$$

where Φ is the core-core pair potential between atom i and all other j atoms separated by distance $r_{i,j}$.

The host atom's electron density ρ_i is given by the superposition of electron densities of all other j atoms separated by distance $r_{i,j}$:

$$\rho_i = \sum_{j \neq i} f_j(r_{i,j}) \tag{2.23}$$

We use EAM potentials for the three fcc metals Ni, Cu and Ag. These potentials are known to be good at reproducing many of the observed properties of bulk and surface systems.

2.2 Transition State Theory

Dynamically evolving systems often have long-lived preferred conformation states (energy basins) between which the systems only switch once in a while. Examples of such systems include chemical reactions, conformational changes of molecules, nucleation events in phase transition, diffusion etc. The reason is the existence of dynamical bottlenecks (called transition states) which confine the system for very long periods of time in an energy basin. In many cases, the waiting times in these energy basins are very long compared to the typical vibration time scale. In these situations, the main objective become the identification of the mechanisms by which the system hops from one energy basin to another i.e., the identification of the transition state between these energy basins and of the rate constants at which transitions occur. From the point of view of atomic motion, at the scale of $1\mathring{A} = 10^{-10}$ m, a given system is composed of atoms. The thermal energy of atoms cause them to vibrate and collide with each other. In a typical system, atoms oscillate on a time scale of 10^{-15} s in a very chaotic way around their average positions (called energy basin). Only once in a while, circumstances are right enough that an atom is able to make a transition (say from one position on the lattice to the next one). These transitions usually take place on a timescale which is much longer than the vibrational timescale of femto seconds. Such transitions are called rare events. Even an event that one would consider quick, say taking on average some milliseconds, is incredibly slow compared to atomic vibrations. The atoms

will vibrate on average 10^{12} times in between such events. Even using simplest description of forces, simulating these events will take years before a transition happens. Most solid state systems are rare event systems and their dynamical evolution is difficult to study through MD simulations.

In Transition state theory (TST), only those rare events that lead to a transition are described in a statistical way at the cost of detailed atomic vibrations. TST can only be applied to the situations in which system must spend a long time on average in each basin before moving to an adjacent basin. A transition state is a state (on the potential energy surface) through which the system must pass to get to another basin, which is mostly true for solid state systems. Harmonic TST (hTST) [30] is employed to calculate the rate of a transition in such systems. In hTST, the rate of a transition for a system of N atoms is expressed as:

$\mathrm{K} = \frac{\Pi_i^{3N}(\omega_i^{IS})}{\Pi_i^{3N-1}(\omega_i^{TS})}\ \mathrm{e}^{-(\Delta E)/kT}$ where ω_i are the harmonic vibrational frequencies and ΔE is the energy barriers of the transition (total energy difference between transition state (TS) and initial state (IS) of the system). Since the frequency mode along the reaction coordinate is negative in TS, this negative frequency is missing in the denominator.

2.3 Methods for Determining Activation Energy Barriers

Various methods [31–33] exists for the calculations of energy barriers. In our studies we mainly used the "Drag" method and Nudged elastic band (NEB) [31] for the projects where we have used EAM based interactions, whereas for DFT based projects we have employed Climbing Image NEB (CI-NEB) method.

2.3.1 The Drag Method

The Drag method is one of the simplest method to find transition states. In this method, one degree of freedom, the drag coordinate, is chosen and is held fixed while all other N-1 degrees of freedom are relaxed, i.e. the energy of the system minimized in a N-1 dimensional hyperplane. In small, stepwise increments, the drag coordinate is increased and the system is dragged from reactants to products. The maximum energy obtained is taken to be the saddle point energy. Sometimes, a guess for a good reaction coordinate is used as the choice for drag coordinate. This could be the distance between two adsorption sites for an atom, for example, in the case of monomer diffusion on fcc(111) surface, this would be the distance between an fcc and hcp site. In the absence of such an intuitive choice, the drag coordinate can be simply chosen to be the straight line interpolation between the initial and final state. This is a less biased way and all coordinates of the system then contribute in principle to the drag coordinate. In the system of our interest, namely island diffusion, we

found drag method to be efficient and accurate as we did compare energy barriers obtained from drag with a more detailed and accurate method like NEB.

2.3.2 Nudged Elastic Band Method

If initial and final state of a system are known, the Nudged Elastic Band (NEB) [9] method can locate the transition state with high accuracy. In NEB, the initial state and the final state are connected through different images of the system linked via springs (representing an elastic band) to keep them equidistant. Generally, images are generated along the straight line interpolation between initial and final state. The optimization algorithm is then applied to relax the images down towards the minimum energy path (MEP). Each image feel the forces due to the springs as well as due to the potential so that each image tries to minimize its potential energy. The force on each image can be written as:

$$F(i) = F_i^s + \Delta V(R_i) \tag{2.24}$$

where $\mathrm{V(R}_i\mathrm{)}$ is the potential energy and R_i are the coordinates of i'th image. The spring force F_i^s is given as:

$$F_i^s = K_{i+1}(R_{i+1} - R_i) - k_i(R_i - R_{i-1}) \tag{2.25}$$

where k is the spring constant.

The spring forces are only allowed to act along the band so that constant image spacing is ensured, and the potential forces are only allowed to act in all directions perpendicular to the band, ensuring that the band comes to rest on the MEP between the minima.

2.4 Methods for determining the Spatial and Temporal Evolution

As mentioned earlier, MD simulations can accurately describe the spatial and temproal evolution of a system, but can only be used for very small systems (upto 100 atoms). On the other hand KMC simulations, equipped with the processes and their activation energies, can be used to study experimental length and time scales.

2.4.1 Kinetic Monte Carlo Method

Generally, in solid state systems, the dynamical evolution occurs through a series of *rare events*, where system spends a long time in one potential-energy minimum before escaping to another one. Since the localized motion in the potential-energy minima is not significant, the dynamical evolution can be simulated as a series of jumps between potential-energy minima. This is the aim of kinetic Monte Carlo (KMC) simulations.

In KMC, the system is evolved stochastically using the energy barriers that govern the evolution of a system and that translates to a real time scale[34]. The KMC time for a given step is scaled by the average time required to observe the particular stochastic event

chosen to occur at that iteration. Thus, each KMC step will have widely different magnitudes depending on the temperature and energy-barrier height.

2.4.1.1 KMC Algorithm

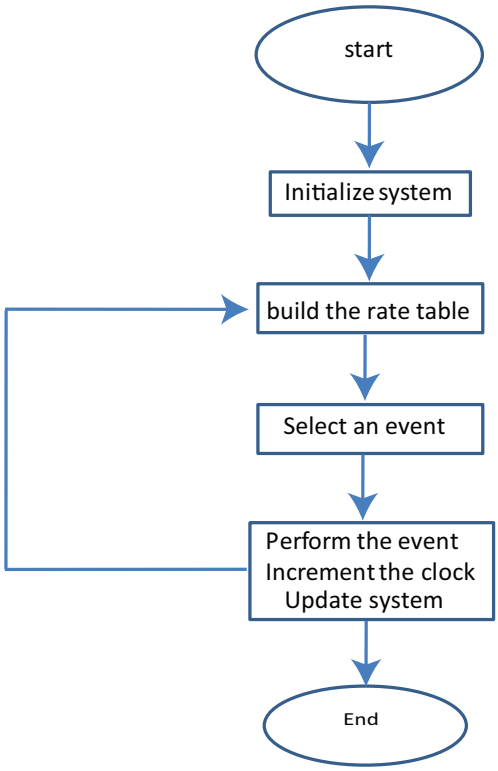

Figure 2.1 A KMC algorithm. (see text for details).

A general flow chart of a KMC algorithm is given in Figure 2.1, with its more elaborated version presented below.

The KMC algorithm we implement is based on the so called "rejection free" algorithm, also known as Bortz-Kalos-Lebowitz(BKL) [2] or residence-time algorithm. This algorithm is described as below:

Step 1. Set the start time t = 0.

Step 2. Update list of all possible events (and their rates) that can occur in the system:

rate r_i of an event i at temperature T, having energy barrier E_b is:

$r_i \propto e^{-E_b/KT}$

Step 3. Calculate the partial cumulative event rates: $S_i = \sum_{j=1}^{i} r_j$

for i = 1,2,3...,N where N is the total number of events. Here $S_0 = 0$ and total rate is $R_T = S_N$.

Step 4. Obtain uniform random number u ϵ [0,1].

Step 5. Select event j to occur with probability:

$S_{j-1}/R_T < u \leq S_j/R_T$

Step 6. Perform event j.

Step 7. Update time t = t - ln(r)/R_T

where 0 < r < 1 is uniform random number.

Step 8. Go to Step 2 and repeat.

At each KMC step, an event is performed, that makes KMC very efficient method and can be used for long time scale simulations. On the other hand, major disadvantage of KMC is that all parameters, such as the complete set of event rates r_i, have to be known in advance. As KMC itself doesn't have the capability of finding the events, most KMC simulations rely ont event rates obtained either from experiments or MD simulations or ab initio calculations. Despite this limitation, KMC remains the most powerful approach available for making dynamical predictions at the mesoscale.

2.4.1.2 Building and Searching Rate List

One of the main steps, where KMC spends most of its time is updating the list of processes and calculating partial cumulative event rates at each KMC step (Step 2 and 3 above). In a very simple implementation, the seach algorithm scales as O(N) where N is the total number of events that can happen at that particular KMC step. For SLKMC-II [19], where we study single island diffusion, we have used linear search algorithm, which is suitable as the rate table at each KMC step is small, but for the case of more complex situations like, island coarsening and growth SLKMC, binary search algorithm with $O(\log_2(N))$ search efficiency is used.

CHAPTER 3
ISLAND-SIZE SELECTIVITY DURING 2D AG ISLAND COARSENING ON AG(111)

We report on early stages of submonolayer Ag island coarsening on the Ag(111) surface carried out using kinetic Monte Carlo (KMC) simulations for several temperatures. Our simulations were performed using a very large database of processes identified by their local environment and whose activation barriers were calculated using the semi-empirical interaction potentials based on the embedded-atom method. We find that during early stages, coarsening proceeds as a sequence of selected island sizes, creating peaks and valleys in the island-size distribution (ISD). This island-size selectivity is independent of initial conditions and results from the formation of kinetically stable islands for certain sizes as dictated by the relative energetics of edge atom detachment/attachment processes together with the large activation barrier for kink detachment. Our results indicate that by tuning the growth temperature it is possible to enhance the island size selectivity

3.1 Introduction

The phenomenon of coarsening or ripening plays an important role in a wide variety of processes in many branches of physical sciences. Particular attention has been paid to Ostwald ripening (OR) [35] which is a general feature at late stages of phase separation,

driven by lowering of excess surface free energy associated with island edges. In OR, islands larger than a critical size grow at the expense of smaller ones. Scanning tunneling microscopy (STM) studies at room temperature have revealed that during the late stages, Ag/Ag(111) coarsening is dominated by Ostwald ripening [36, 37]. What has not been studied in depth so far is the initial stage of the coarsening process which may point to certain features that could be used to tune growth patterns of thin films.

3.2 Simulations

Here we present results of kinetic Monte Carlo (KMC) simulations of the initial stages of coarsening of two-dimensional Ag islands on Ag(111). These simulations made use of a very large database of processes which was obtained from previous self-learning KMC (SLKMC) [1, 10, 38] simulations of small and large Ag/Ag(111) island diffusion carried out at 300 K and 500 K. All processes in this database move atoms from one fcc site to another. We examined the dependence of island-size distribution (ISD), as coarsening proceeds, on the choice of initial ISD and shape of the islands, and the surface temperature. Although most of the results shown here are for a Gaussian ISD, we have also carried out simulations starting with random and delta ISDs.

In an SLKMC simulation, rather than using a fixed catalog of processes with given activation barriers, processes and their energetics are obtained on the fly and stored in the

database, whenever a new configuration is detected. In an earlier study [11], we used this database to carry out long timescale (few hundred seconds) KMC simulations of Ag(111) island coarsening at room temperature. In determining activation energies we used interaction potentials based on the embedded-atom method (EAM) as developed by Foiles *et al* [29]. A simplification was introduced by assuming a "normal" value for all diffusion prefactors, although we are aware that multiatom processes may be characterized by high prefactors [39–41]. Rates are, however, not expected to be strongly affected in the explored low/moderate temperature regime. More details about database acquisition/types of processes frequented and recipes for speeding KMC simulations can be found in Ref.[11].

3.3 Results

The initial configuration for these coarsening simulations was created by dividing the empty lattice into boxes and placing islands of different sizes randomly at the center of the box to prevent overlap of islands. The number of islands of a particular size depends on whether the starting ISD is a Gaussian or a delta function. We ran our simulations using both Gaussian and delta initial ISDs. In the delta initial distributions, we set all 742 islands at a given size (repeating the simulation for islands of all sizes between 10 and 30). For a Gaussian distribution the total number of islands depends on the number of islands (a) of average size that is, the number of islands at the peak of the distribution (μ) and the

width of the distribution (σ). All island sizes between $\mu \pm \sigma\sqrt{2\ \ln(a)}$ are present in the distribution so that the distribution is uniform around the average island size. Figure 3.1 shows an example of a Gaussian initial island-size distribution, this one with peak of 100 islands at size 12 and width of 3.

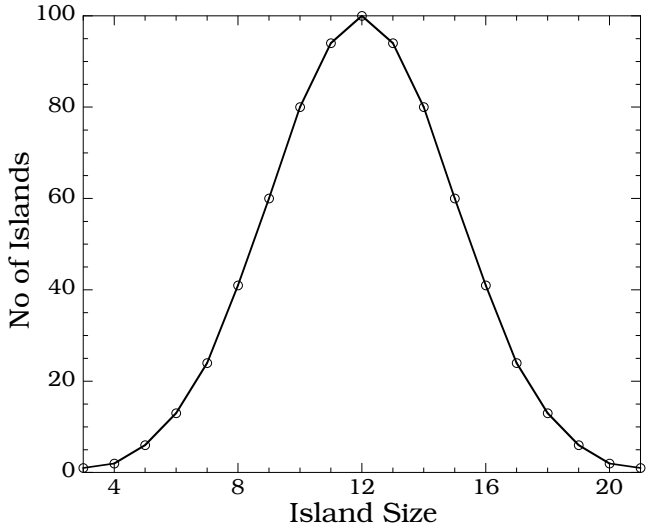

Figure 3.1 Gaussian initial island size distribution with peak of 100 island at size 12 and width of 3.

To avoid finite-size effects we carried out simulations using a relatively large system size of 1024×1024 fcc lattice units with periodic boundary conditions, and in order to obtain good statistics we averaged our results over 10 runs

Our starting ISD with a Gaussian distribution has a total of 742 islands with a peak of 100 islands at the average island size and a width of 3. The total number of islands is kept constant (742) for all further simulations by keeping the peak island count and the width of the Gaussian distribution constant regardless of the average island size. We also take the

total number of islands in the initial delta ISD to be 742, as in all others. For simplicity the initial shapes of islands are chosen arbitrarily and islands of same size are assigned the same shape. For the results presented here, most of the island shapes are either compact or close to compact. In addition, we have carried out coarsening simulations with fractal island shapes and initial random ISD, and also initial random distribution of monomers.

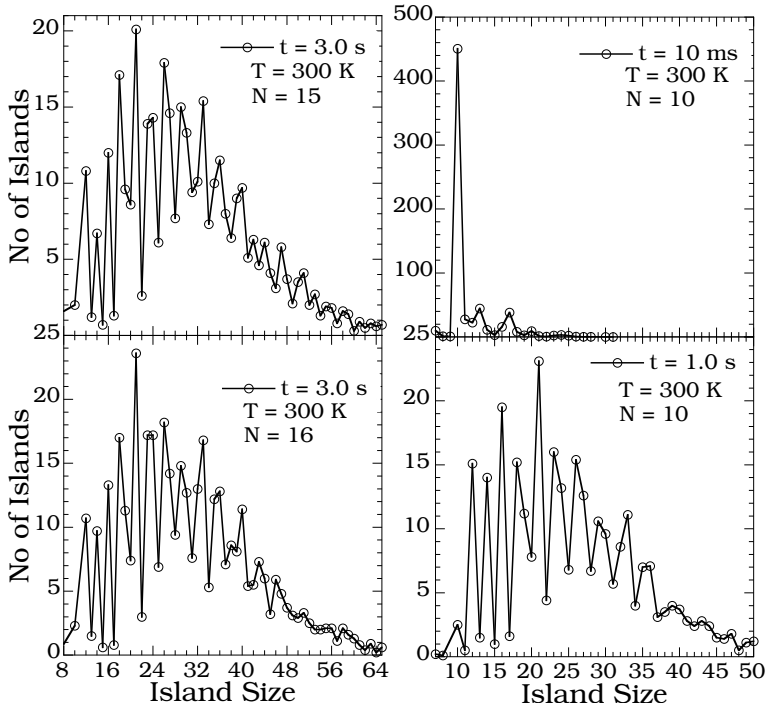

Figure 3.2 ISDs at T = 300 K after 3.0 s for average island sizes (a) $N = 15$ and (b) $N = 16$ when initial ISD is a Gaussian. (c) 10.0 ms (d) 1.0 s when initial ISD is a delta function for average island size $N = 10$.

To capture features dominating the early stages of coarsening we carried out simulations for 3.0 s. Figure 3.2 (a)-(b) show ISDs after 3 s of coarsening for initial average island sizes of 15 and 16 atoms for Gaussian initial ISDs, while Figure 3.2 (c)-(d) displays ISDs after 10.0 ms and 1.0 s of coarsening for initial average island size of 10 atoms when the

initial ISD is a delta function. As is evident, during coarsening there is a dramatic change in the ISD from a smooth Gaussian or delta distribution to a non-smooth distribution with peaks and valleys at specific island sizes. From Figure 3.2 it can be seen that island sizes whose populations are either a peak or a valley in the ISD remain so as the coarsening proceeds. Furthermore the behavior of ISD with peaks and valleys is independent of the initial configuration and the initial averages island size. Table 3.1 summarizes island sizes up to 35 atoms according to whether they constitute a peak, a valley or neither in the ISD after 1.0 s of coarsening. Some island sizes (19, 27 and 30 atoms) correspond to neither a peak nor a valley (Table 3.1). Islands containing either 23 or 24 atoms, may constitute a peak, but for the most part, the 23-atom one is a peak, while the 24-atom one is neither a peak nor a valley. Note that at much later times all islands will follow Ostwald ripening, resulting in one large island; the total energy of the system will decrease as more bonds are formed until it saturates when one large island is formed.

Table 3.1 List of island sizes for which the ISD is a peak, valley or neither after 3.0 s coarsening.

Feature	Sizes of Islands									
Valley	11	13	15	17	20	22	25	28	31	34
Peak	12	14	16	18	21	23(24)	26	29	33	35
neither				19			27	30	32	

We note from Figure 3.2 that the characteristics of coarsening are independent of whether the initial ISD is Gaussian or a delta function. We also observed the same behavior when coarsening simulations were started with an initial configuration created by depositing

atoms at very low temperature (135 K). At this temperature islands are fractal and ISD is random. Thus, in what follows we concentrate our discussion on the results only for the Gaussian distribution. Figure 3.3 shows the decay in the number density of islands with $11 - 14$ atoms with time. It is clear that 11-atom and 13-atom (valleys) islands decay exponentially in the very first few microseconds of coarsening. The densities islands with 12 and 14 atoms (peaks) increase for the first few microseconds before starting to decay at a much slower rate. The same pattern emerges for all island sizes constituting peaks or valleys. Similar decay of island densities is also observed when the initial ISD is a delta function.

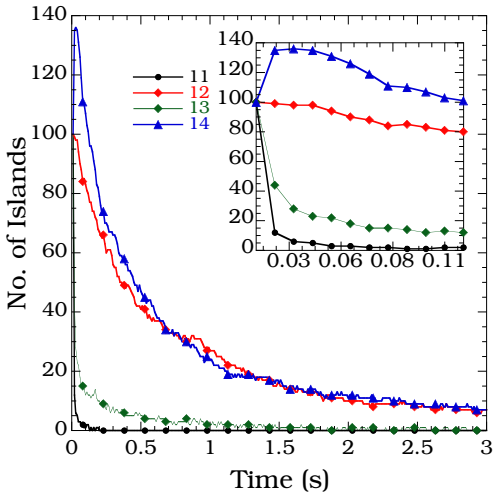

Figure 3.3 Decay of the number of islands with time for several island sizes at T = 300 K. At $t = 0$ number of islands is 100. Inset shows the same at very early stages.

Peaks and valleys in the ISD during coarsening and differences in the rate of decay of densities of corresponding island sizes shows that coarsening occurs through a sequence of selected island sizes, which form kinetically stable islands. In addition, ISD exhibits the same characteristic behavior even when the shapes of islands are altered in the initial configuration:

all islands with kinetically stable (or low-energy) or fractal or other irregular shape lead to the same results for ISD [42]. This shows that island-size selectivity is independent of parameters of initial configuration including shapes of the islands, and hence the broader implications of our results.

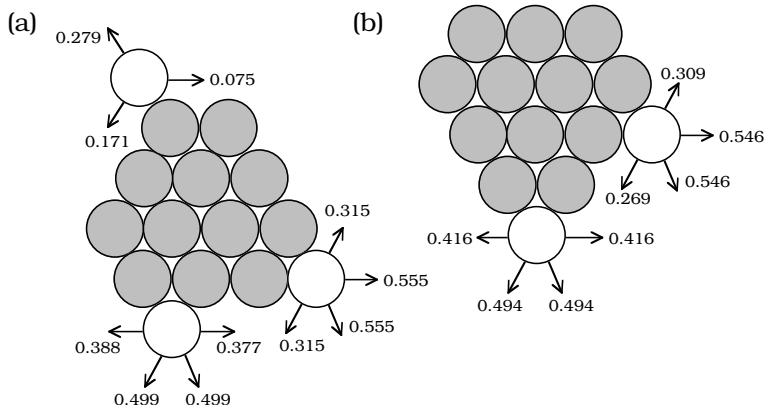

Figure 3.4 Activation barriers (in eV) for the most frequent detachment and edge diffusion processes.

From experimental [36, 43] and theoretical studies [11], it is known that 2D Ag/Ag(111) coarsening is due to evaporation-condensation mediated by monomer diffusion between islands. For further investigation into island-size selectivity, we examined the energetics of detachment processes on the basis of island size. We find that for all island sizes larger than 8 atoms, the most frequent detachment process is an atom detaching from a step edge to create a monomer. For island sizes smaller than 8 atoms, the energy barrier for concerted diffusion is quite small ($0.1 - 0.3$ eV) compared to single atom detachment process, causing these islands to diffuse and coalesce with others. In addition, we find that the number of events of edge atom detachment for island sizes whose populations are valleys in the ISD is

higher than for island sizes whose populations are peaks. Figure 3.4 shows the most frequent detachment processes (of edge atoms) for islands along with their corresponding activation barriers. Because the detachment barrier for an atom with at least 3 nearest neighbor atoms is greater than 0.7eV, they rarely detach to create monomers at room temperature.

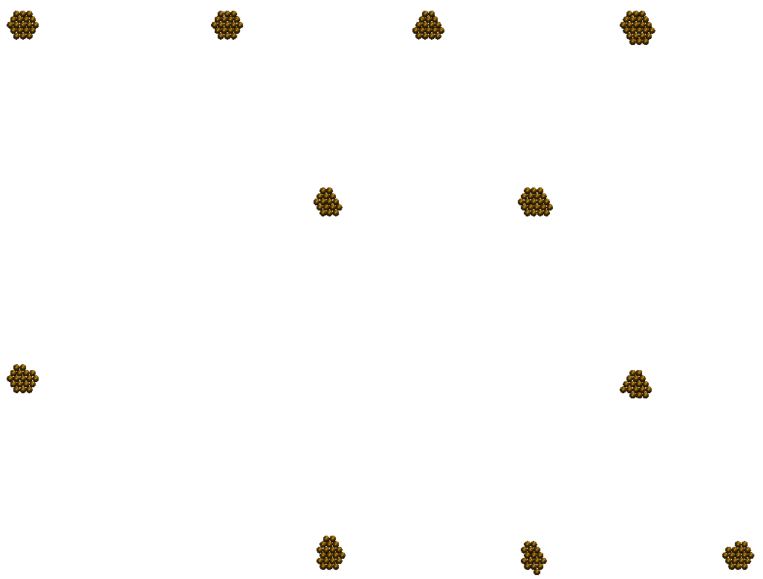

Figure 3.5 Island morphology during room-temperature coarsening for initial average island size of 19 atoms with Gaussian initial ISD. Pictures correspond to 128×128 portion of a 1024×1024 system.

These arguments based on system energetics confirm findings in our KMC simulations that islands whose populations are valleys in the ISD usually have an edge atom in their shapes. From Figure 3.4 it can also be seen that difference between an edge diffusion barrier and an edge-atom detachment barrier is quite small, especially on a B-type step edge, making detachment of an edge atom relatively easy and hence a frequent process. Any island with an edge atom either loses this atom through detachment (leaving a smaller island of selected

size) or attracts (less frequently) a nearby monomer (creating a bigger island of selected size), the overall result being the creation of island sizes whose populations show up either as peaks or valleys in the ISD. Consequently, island sizes whose populations are peaks in the ISD do not have edge atoms: all atoms have at least 3 nearest neighbors, making them kinetically stable islands: a result again confirmed by our KMC simulations. Consider, for example the non-selected island set of sizes 11, 13, 15 and 17 atoms whose densities are zero in Figure 3.2, and the other of sizes 20, 22, 25, 28, 31 and 34 atoms whose densities are small but non-zero. The former set rarely forms kinetically stable shapes, while latter does, albeit less frequently than the ones that show up as peaks in the ISD.

We have also carried out simulations in which barriers for the most frequent detachment processes were increased, thereby increasing the difference between edge-diffusion and detachment barriers. We find that with the increasing difference, on set of island selectivity shifted to latter times. This shows that difference in energy barriers between edge atom detachment and edge diffusion processes controls the on set of island-size selectivity. Accordingly, we conclude that island-size selection is primarily due to adatom detachment and attachment processes at island boundaries owing to the relative ease with which atoms can detach in comparison with the relative difficulty for the detachment of atoms with at least 3 neighbors. Fig. Figure 3.5 is a snap shot of morphology of Ag(111) surface after coarsening at room temperature when the initial average island size was 19 atoms with Gaussian initial ISD. This snap shot corresponds to 128×128 portion of a 1024×1024 system. Note the

survival of compact 18-atom, 19-atom and 21-atoms islands. Accordingly, we conclude that island-size selection is primarily due to adatom detachment and attachment processes at island boundaries owing to the relative ease with which edge atoms can detach in comparison with the relative difficulty for the detachment of atoms with at least 3 nearest neighbors. Elsewhere we show that these factors also restrict the shapes of island that may form during coarsening [42]. Certain non-selected island sizes (valleys in ISD), which may otherwise form kinetically stable shape do not persist in the simulations since their formation by adatom attachment or detachment is not found to be followed by shape rearrangement due to high kink detachment barrier.

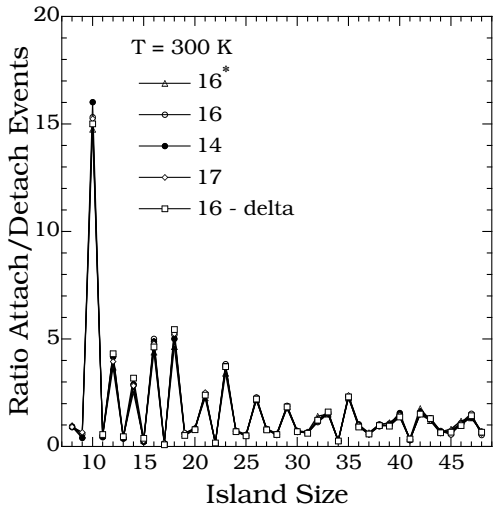

Figure 3.6 Ratio of number of attachment to detachment events at 300 K after 3 s of coarsening for Gaussian initial ISD ($N = 14, 16, 17$), delta initial ISD (N = 16) and Gaussian initial ISD with islands either have kinetically stable or low-energy shapes ($N = 16^*$).

Figure 3.6 shows the variation of the ratio of number of attachment to detachment events at 300 K after 3.0 s of coarsening with initial average island size for initial Gaussian

and delta ISDs. Figure 3.6 also shows the ratio for average island size of $N = 16^*$ when the coarsening is started with a Gaussian initial ISD in which all islands have shapes that are either low-energy [44] or kinetically stable. It can be seen that peaks and valleys are exactly at the same island size as in the island-size distributions. This shows that densities of selected island sizes decay because of attachment events while non-selected island sizes decay because of detachment of edge atoms. Interestingly, they all collapse to a single curve, indicating that this ratio is independent of all parameters for initial ISD and also of the shapes of the islands in the initial configuration. From this we conclude that island-size selectivity is the behavior of the early stages of Ag/Ag(111) coarsening and is independent of initial configuration used to start the coarsening.

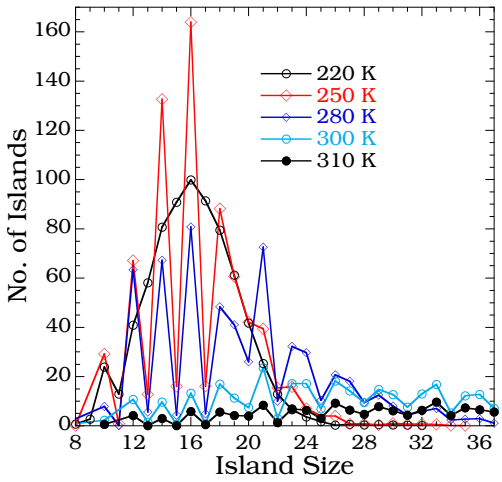

Figure 3.7 ISD at 220, 250, 280, 300 and 310 K after 3 s for average island size of 16 atoms when initial ISD is a Gaussian.

We also investigated how island-size selectivity depends on temperature after 3.0 s of coarsening. Figure 3.7 shows island-size distributions for initial average island size of 16

atoms in the temperature range $200 - 310$ K when the initial ISD is a Gaussian. It is easy to see that while the island-size selectivity is independent of temperature, the strength of selectivity is temperature dependent and is particularly strong in the range $250 - 270$ K. This can be seen in Fig Figure 3.7 for 250 K for which the population of island sizes which correspond to peaks in the ISD increases beyond their magnitude in the initial configuration, at the expense of those which constitute valleys in the ISD. As the system coarsen further, the selectivity will eventually decay and those will look similar to ISDs after coarsening for shorter time scales at higher temperatures. At temperatures below 240 K coarsening occurs at a slower rate such that the island-size selectivity does not emerge during initial 3.0 s of coarsening. Above 270 K coarsening happens at a faster rate and even though island density decays rapidly, island-size selectivity is still detected. In the temperature range $250 - 270$ K, coarsening occurs at an optimal rate enabling island-size selectivity to be observed during the data taking. We also find that the smaller the average island size in the initial configuration, the more quickly the ISD changes to peaks and valleys.

3.4 Conclusions

In summary, we find that during the early stages, 2D Ag/Ag(111) island coarsening proceeds as a sequence of selected island sizes, whose densities decay at rates slower than that of the others because of the formation of kinetically stable island shapes. The

densities of non-selected sizes (valleys) decay at a faster pace due to frequent adatom attachment/detachment processes. We also find that this behavior is independent of all parameters of initial configuration showing that it is a characteristic of early stages of Ag island coarsening on Ag(111). Finally, we find that strength of island-size selectivity depends on temperature and is strongest between $250 - 270$ K, though the peaks and valleys in the ISD are independent of temperature. It is thus possible to tune the growth temperature so as to take advantage of the enhanced island-size selectivity. We await experimental findings to validate our predictions.

CHAPTER 4
EXTENDED PATTERN RECOGNITION SCHEME FOR SELF-LEARNING KINETIC MONTE CARLO(SLKMC-II) SIMULATIONS

4.1 Introduction

Kinetic Monte Carlo (KMC)[2–7] method is an extremely efficient method for carrying out dynamical simulations of a wide variety of stochastic and/or thermally-activated processes when these are known in advance. Accordingly, KMC simulations have been successfully used to model a variety of dynamical processes ranging from catalysis to thin-film growth. However in many cases it is difficult to know *a priori* all the relevant processes that may be important during simulation. To overcome this problem, on-the fly KMC[8, 9] methods were developed that allow the calculation of all possible processes at each KMC step. But the fact that on-the fly KMC methods do not store these calculated processes results in redundancies and repetitions in the calculations of energetics of the system dynamics. In order to avoid repeated calculation of energetics of the processes previously encountered, self-learning KMC (SLKMC) method[10] was developed, which introduces a pattern-recognition scheme that allows the on-the-fly identification, storage and retrieval of information about processes based on the local neighborhood of each active (under-coordinated) atom consequently speeding up simulations by several orders of magnitude.

On the fcc(111) surface there are two types of threefold adsorption sites: the normal fcc site and the fault hcp site. The pattern recognition scheme used in previous studies[1, 10–12] for fcc(111) surface was restricted to the occupation of fcc sites only and hence was unable to account for the processes that involve movement of atoms to or from hcp sites.[13, 14]. In this chapter we present a pattern-recognition scheme that does allow occupation of hcp as well as fcc sites on the fcc(111) surface. We then illustrate its use by applying it to the self-diffusion of three different systems.

4.2 Pattern Recognition Scheme

In order to accommodate hcp as well as fcc sites, SLKMC-II modifies both the pattern recognition scheme and the saddle-point search for finding processes and calculating their energetics. A pattern-recognition scheme allows unique identification of the local neighborhood of an atom by assigning a unique combination of an index number or key, enabling SLKMC simulations to store and retrieve on the fly information about processes from a database that in traditional KMC simulations must be hardwired.

As mentioned earlier, an adatom island on an fcc(111) surface may occupy either an fcc or an hcp site or a combination of fcc and hcp sites, but the pattern-recognition scheme used in SLKMC simulations up to now is limited to identifying adatom islands on fcc sites only. We have now improved the scheme to enable identification of adatom islands occupying

hcp sites as well. This pattern-recognition scheme is simple, fast and capable of handling 2-D on-lattice fcc(111) systems. We call this SLKMC method with new pattern recognition scheme SLKMC-II.

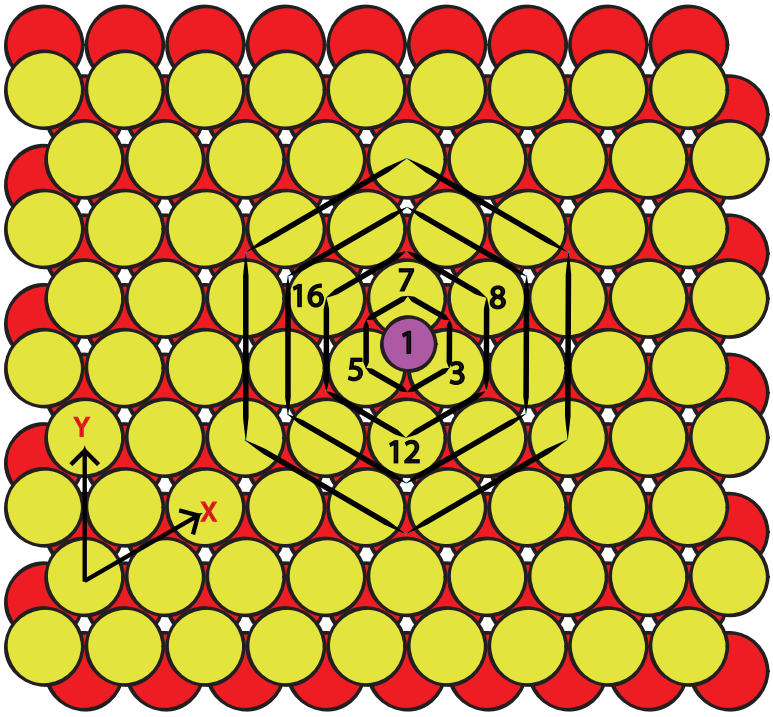

Figure 4.1 Grouping different sites into hexagonal rings on the fcc(111) surface.

Like the previous fcc-only scheme, the pattern-recognition scheme used in SLKMC-II groups adsorption sites into hexagonal rings, generates a unique binary bit-pattern based on the occupancy of those sites, and stores it in a database along with the processes associated with that configuration or local neighborhood. In order to uniquely identify whether an atom is on an fcc or hcp site, we include the top-layer substrate atoms (henceforth referred to as substrate atoms) in the pattern-recognition scheme.

Figure 4.1 shows the grouping of fcc, hcp and substrate atoms into the first 4 such hexagonal rings around a monomer (represented by the purple-colored circle) on an fcc site marked as 1. It can be seen that, except for the first ring, which is a combination of hcp sites and the substrate atoms, the rings are combinations of fcc sites, hcp sites and substrate atoms. We note that for a monomer on an hcp site, the first ring is a combination of fcc sites and substrate atoms.

The X and Y arrows in Figure 4.1 show the directions on the fcc(111) surface that we map onto a square lattice for our simulations. To represent the fcc(111) surface, we assign each substrate atom a height of 1, each unoccupied fcc or hcp site a height of 0, and each occupied fcc or hcp site a height of 2. (Note that any site to the left of a substrate atom along the X-axis in Figure 4.1 is an hcp site, while any site to the right of the substrate atom along that axis is an fcc site.) The set of rings in Figure 4.1 are further elaborated in Figure 4.2(a) with numbering scheme that we have used. With the diffusing atom at an fcc site labeled as 1, we mark the hcp sites and substrate atoms surrounding it in ring 1 clockwise starting from the X-axis from 2 to 7, as shown in Figure 4.2(a). The sites in the second ring are similarly labeled from 8 to 19. The same procedure follows for the other rings. In the binary bit pattern (cf. Figure 4.2(b)), substrate atoms are always represented as 1, while fcc or hcp sites are represented as either 1 or 0 depending on whether the site is occupied or not. As in the numbering of the sites, the binary digits for a ring (cf. Figure 4.2(b)) begin at the X-axis (cf. Figure 4.1) and proceed clockwise. Resulting binary bit

sequence is recorded (starting from right to left) as shown in Figure 4.2(b). Ring numbers for a monomer at an fcc site in a three-ring system are as shown in Figure 4.2(b & c). For convenience we have shown only two rings, although more rings are required to cover the neighborhood of larger islands. Following this method, ring numbers for every active atom in an island are generated on the basis of the occupancy of sites in its surrounding rings. For each configuration thus identified, a saddle-point search is initiated to find all possible processes and the activation energy for each. The result: configuration representing local neighborhood of the active atom, its processes, and their activation energies are then stored in the database. For the case of monomer on an fcc site as shown in Figure 4.2(c), the configuration is represented by three rings as 42, 273, 83220, it has three processes each having an activation barrier of 0.058 eV, for each process only one atom is involved and finally the actual move for process 1 is that atom at position 1 moves to position 2.

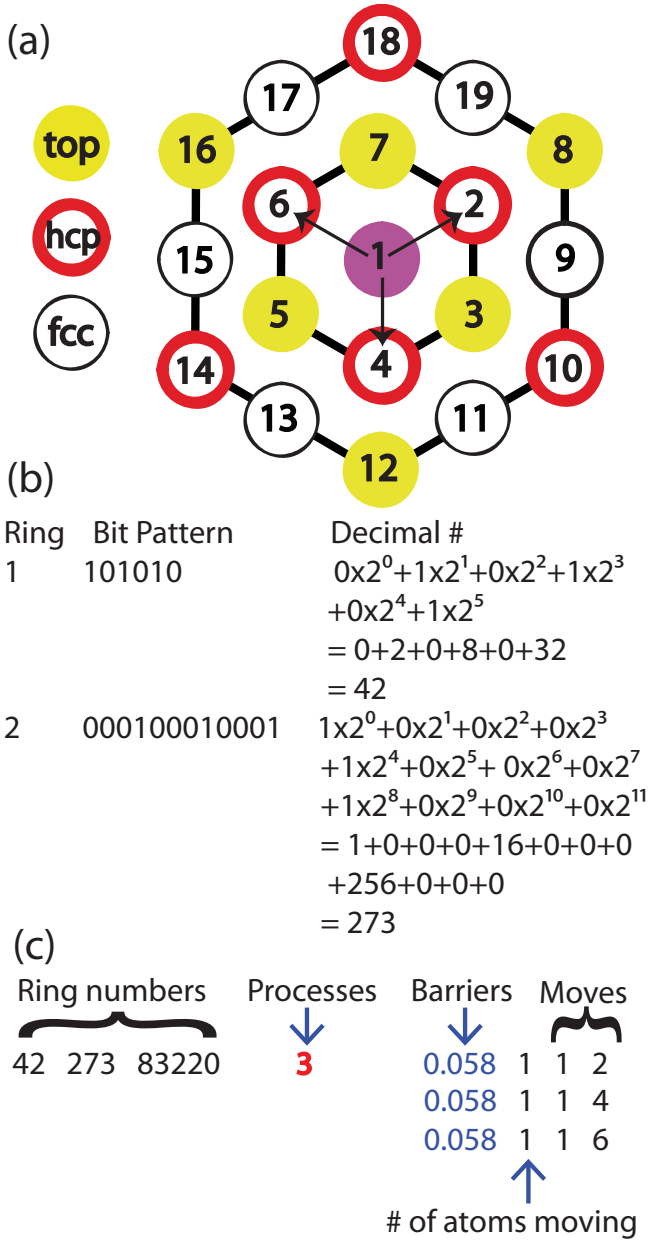

Figure 4.2 (a) Gold (light filled) circles represents substrate atoms while black and red (thick) circles represent fcc and hcp sites respectively. Purple (dark filled circle) represents an atom on fcc site while arrows show possible processes for such an atom. (b) Assignment of binary bit pattern and corresponding conversion into decimal number. (c) Format of the database for this configuration.

An atom is considered to be active if there is at least one vacant site in the second ring. As in the previous (fcc-only) pattern-recognition scheme, a process is identified as the motion of an active atom to a neighboring ring, accompanied by the motion of any other atom or atoms in the island. We note that in this scheme an atom can move more than one ring, namely when it moves from an fcc to a nearest fcc site or from an hcp to a nearest hcp site. The format of the database is exactly the same as in the fcc-only pattern recognition scheme[10, 11], except that the new scheme requires more rings to identify the same neighborhood than does the fcc-only method.

In order to minimize the size of the database we exploit the sixfold symmetry of the fcc(111) surface. In particular, the following five symmetry operations were used in recognizing equivalent configurations: (1) 120° rotation, (2) 240° rotation, (3) mirror reflection, (4) mirror reflection followed by 120° rotation and (5) mirror reflection followed by 240° rotation. At each KMC step, only if neither a given configuration nor its symmetric equivalent is found in the database, is a saddle-point search carried out to find the possible processes along with their activation energies for subsequent storage in the database. Note that for an atom on an hcp site, the first ring is always equal to 21 while for an atom on an fcc site it is 42.

The difference in the value of the first ring for an atom on an fcc and that for hcp site is due to the fact that substrate atoms are oriented differently around the fcc or hcp sites. This fact facilitates in the unique identification of whether an atom is on an fcc or

hcp site. Thus for 2-D pattern recognition, inclusion of substrate atoms in the first ring is sufficient. Accordingly all substrate atoms beyond the first ring can be assigned 0's instead of 1's without any ambiguity in the identification of the local neighborhood. This custom modification to our 2-D simulations reduces computational effort in matching ring numbers when neither fcc nor hcp sites are occupied in a given ring. It also reduces storage of large numbers in the database. For example in the case of a monomer on an fcc site, the ring numbers would be 42, 0, 0 instead of 42, 273, 83220 (as they appear in Figure 4.2(b)).

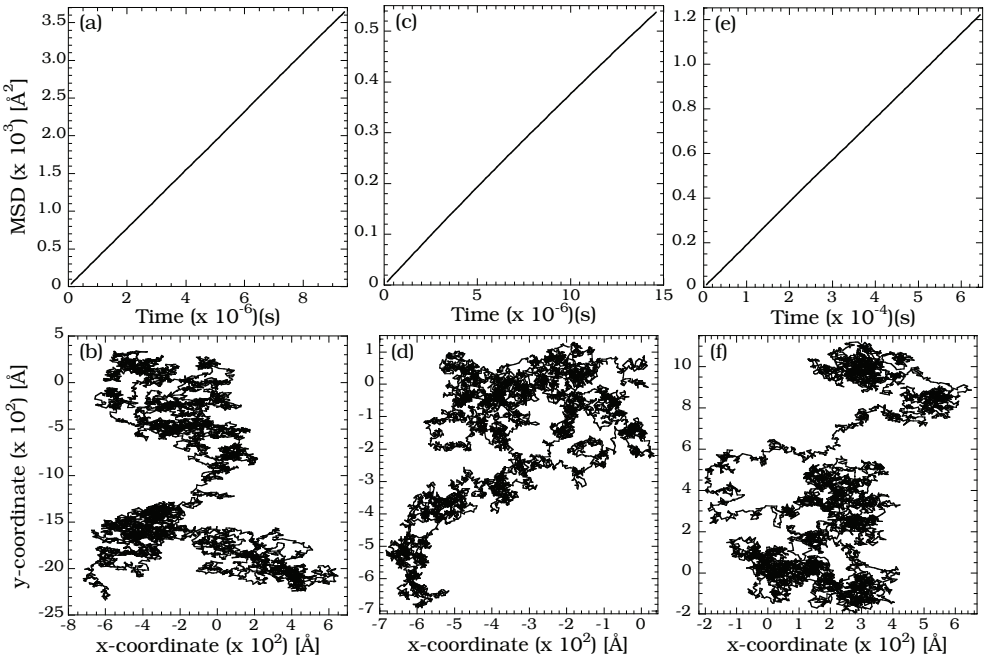

Figure 4.3 Mean square displacements and center of mass trajectories for Cu((a)&(b)), Ag((c)&(d)) and Ni(e)&(f)) at 500K

To find the processes of a given configuration and their respective energy barriers, saddle-point searches are carried out using the drag method. In this method a central atom

is dragged (i.e., moved in small steps) towards a probable final position. If the central atom is on an fcc site, then it is dragged towards a vacant fcc site in the second ring; if it is on an hcp site, it is dragged towards a vacant hcp site in the second ring. Since hcp sites are allowed, the atom being dragged from an fcc site to a neighboring one can relax to an hcp site in between the two (Similarly, an atom being dragged from an hcp to a neighboring vacant hcp site can end up on an intermediate fcc site). In other words, processes are possible in which atoms in an island may occupy fcc, hcp or fcc-hcp sites. The dragged atom is always constrained along the reaction coordinate while it is allowed to relax along its other two degrees of freedom (perpendicular to this direction) and all the other atoms in the system are allowed to relax without constraint. Once the transition state is found, the entire system is completely relaxed to find the island's final state. The activation barrier of the process is the difference between the energies of the transition and initial states. We verified the energy barriers of the some of the key processes found by the drag method using the nudged-elastic band (NEB) method and found little difference. For inter-atomic interactions, we used interaction potential based on the embedded-atom method (EAM) as developed by Foiles *et al*[29]. In all our calculations we use the same pre-exponential factor (10^{12}), this has been proven to be a good assumption for the systems like the present one [41, 45].

Table 4.1 Diffusion coefficients at various temperatures and effective energy barriers for 9 atom islands of Cu, Ag and Ni. Values in brackets are for Cu from reference [1]

System	300K	400K	500K	600K	700K	E_{eff} (eV)
Cu	1.43×10^6	4.53×10^6	3.88×10^6	1.64×10^9	4.82×10^9	0.367
	(7.72×10^4)		(7.20×10^7)		(1.45×10^9)	(0.444)
Ag	6.62×10^4	3.36×10^6	3.67×10^7	1.95×10^8	6.43×10^8	0.414
Ni	5.48×10^2	8.77×10^4	1.89×10^6	1.35×10^7	6.23×10^7	0.525

4.3 Results

We have used SLKMC-II to study the self-diffusion of a 9-atom island of Cu, of Ag and of Ni on the corresponding (111) surface. To account for all types of processes (for compact and non-compact 9-atom islands), especially concerted processes and multi-atom processes, we used 10 rings to cover the same neighborhood that required 5 rings in the predecessor scheme, which was capable of recognizing only fcc sites. We begin our simulation for a given system with an empty database. The database is then filled up as new processes are encountered during the simulation. In most cases database accumulation is nearly complete after the first couple of hundred KMC steps, after which the simulation only occasionally performs a calculation of new processes (namely, when a previously un-encountered configuration is detected) and stores the result in the database. In what follows we first present the diffusivities for these three systems at various temperatures and the corresponding effective energy barriers. In discussing the Cu system, we compare our results with those obtained earlier using the fcc-only pattern recognition scheme [1]. We then highlight some frequently picked processes (and their energy barriers) encountered during

these simulations that were impossible to detect under the previous-pattern recognition scheme [10].

4.3.1 Diffusion Coefficients and Effective Energy Barriers

We performed SLKMC-II simulations for 10^7 KMC steps in the case of Cu and Ag and 10^8 KMC steps in the case of Ni and recorded the trace of the center of mass of a 9-atom island for each system along with the real time of simulations for the temperature range of 300 K-700 K. Figure 4.3(a-f)) shows the mean square displacement and center of mass trajectories for all three systems at 500 K. Table 4.1 shows the diffusion coefficients and effective energy barriers derived, respectively, from the mean square displacements (Figure 4.3(a, c & e)) and Arrhenius plots (Figure 4.4) for each of the three systems. (Values in parentheses there are those for Cu from Ref. [1]). Table 4.2 shows the energy barriers for various types of processes which are picked during the simulations. Some of the details of these types of processes are explained later in the section. We note that for all three systems, a 9-atom island incorporates a compact 7-atom hexagon with two extra atoms at different positions on the boundary of the hexagon (see Figure 4.8). The most frequently-picked processes are the single-atom processes (non-diffusive) – namely edge running and corner rounding – whereas kink detachment (diffusive) processes, which are responsible for change in island shape and hence change in the island's center of mass, are less frequent than the most diffusive concerted processes (cf. Figure 4.9 & Figure 4.5). We note that in our

simulations of island diffusion, we disallowed any type of detachment processes resulting in the formation of a monomer although they are detected and stored in the database.

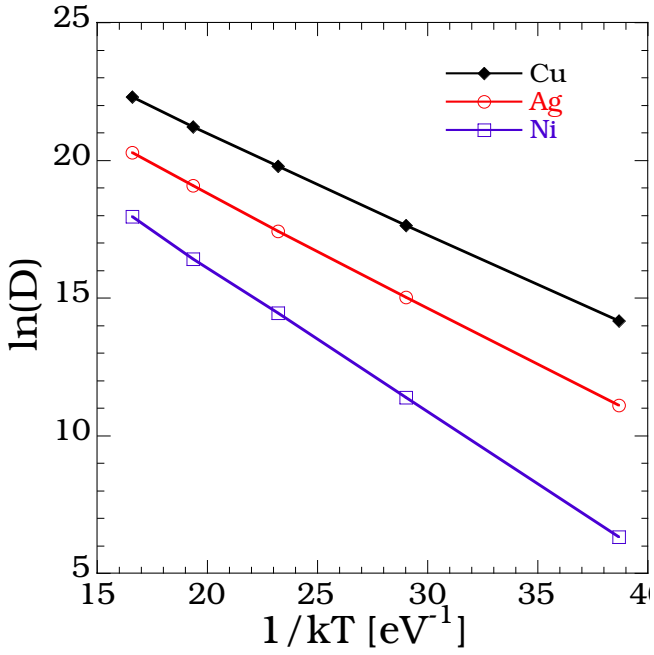

Figure 4.4 Arrhenius plot of diffusion coefficients as a function of inverse temperature for 9-atom Cu, Ag and Ni island.

As to Cu, from Table 4.2, it can be seen that the energy barriers for concerted processes (cf. Figure 4.5(a & b)) are roughly in the range of $0.265 - 0.400$ eV (see text below for details), whereas for single-atom edge-running processes (cf. Figure 4.9), the energy barriers are roughly in the range of $0.245 - 0.285$ eV. Single atom processes, especially edge-running and corner-rounding processes are the most frequently picked processes during simulations. These processes do not contribute to island diffusion except when preceded by kink-detachment processes. The next most frequently picked processes are the concerted

processes in which all atoms in an island move together either from fcc to hcp or vice versa. Concerted process cause maximum displacement of the center of mass and hence contribute the most to the diffusion of the island. After concerted processes, multi-atom processes like reptation (cf. Figure 4.6(a & b)) and shearing (cf. Figure 4.7(a & b)) contribute most to the island diffusion. These processes are picked only when island becomes non-compact, as happens but rarely in the temperature range under study here. As mentioned earlier, kink detachments which occur very rarely at low temperature becomes the frequent events at high temperatures and are responsible for island diffusion through island shape change. For Cu 9-atom island diffusion we obtained effective energy barrier of 0.370 eV, which is close to diffusion barriers for concerted processes. Accordingly we conclude that Cu 9-atom island on fcc (111) surface diffuses via concerted processes. As can be seen from Table 4.1, because of the inclusion of fcc and hcp adsorption sites in our simulations, diffusivity of Cu is higher and correspondingly effective energy barrier is almost 0.077 eV less than that obtained using SLKMC[1] with fcc-only pattern recognition scheme.

For the case of Ag 9-atom island, it can be seen from the Table 4.2 that the gap in the energy barrier between edge running and concerted processes is large as compared to the case of Cu 9-atom island. Accordingly concerted processes being picked are less frequent for the same number of KMC steps as for Cu 9-atom island resulting in lower diffusivity of Ag 9-atom island (compare Figure 4.3 (b)&(d)). Also kink detachment processes are picked more often as compared to the case of Cu. For Ag 9-atom island diffusion we obtained an

effective energy barrier of 0.414 eV which is close to the energy barrier of concerted processes indicating that island diffusion mainly proceeds via concerted processes.

Table 4.2 Energy barriers for different types of processes. A(B)2→A(B)2 represents A(B) edge running, A(B)2→C1 represents A(B) corner rounding and K3→C1 represents kink detachment processes

Processes	Ni (eV)	Cu (eV)	Ag (eV)
Concerted	0.530	0.265-0.400	0.420
Reptation	0.400	0.320	0.348
A(B)2→A(B)2	0.322(0.440)	0.245(0.285)	0.260(0.330)
A(B)2→C1	0.400(0.540)	0.310(0.390)	0.300(0.350)
K3→C1	0.730	0.590	0.555

4.3.2 Example Processes

As mentioned earlier, the database generated by SLKMC-II records all of the single-atom and multi-atom processes captured by its fcc-only predecessor, but register as well a number of processes that were outside that predecessor's grasp: concerted processes, two types of multi-atom processes - shearing and reptation[46, 47] as well as single atom processes involving moves from fcc to hcp, hcp to fcc and hcp to hcp.

4.3.2.1 Concerted Processes

It is already well known that small islands on fcc(111) surface diffuse via concerted processes,[48–50] in which all atoms in the island move simultaneously. In these processes, atoms in the island move from fcc to hcp if the island is initially on fcc or from hcp to

fcc if on hcp. SLKMC-II automatically finds all such processes. Interestingly enough all three systems under study here exhibit such concerted diffusion processes. Some examples of compact shapes frequently diffusing through concerted processes for Cu, Ni and Ag are shown in Figure 4.5(a & b). Energy barriers for these processes are different among the three materials. As can be seen from Table 4.2, the energy barrier for concerted processes for the 9-atom Cu island is in the range $0.265 - 0.400$ eV: 0.265 eV for diffusion from hcp to fcc; above 0.350 eV for fcc to hcp, depending on the shape of the island; 0.400 eV for concerted diffusion of non-compact shapes.

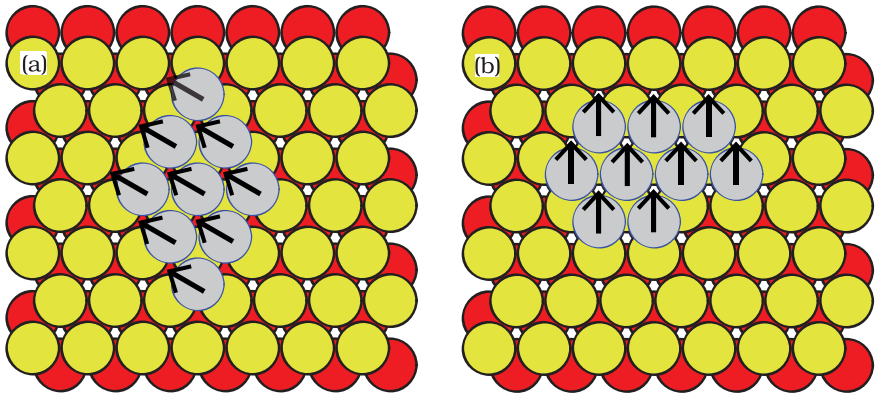

Figure 4.5 Examples of 9-atom islands with compact shape that often undergo concerted processes as marked by the arrows (Only one concerted process is shown for each case). (a) for Cu & Ag. (b) for Cu & Ni.

For the 9-atom Ag island, the activation barrier for concerted diffusion processes is around 0.420 eV, with little difference whether the island moves from hcp to fcc or vice versa; non-compact 9-atom Ag island diffuses not through concerted but through multi-atom or single atom processes (discussed in the next sections). The activation barrier for concerted

diffusion of the 9-atom Ni island is around 0.530 eV; as in the case of Ag, it makes little difference whether this diffusion begins on hcp or on fcc sites; and non-compact shapes diffuse not through concerted but through multi- or single-atom processes.

4.3.2.2 Multi-atom Processes

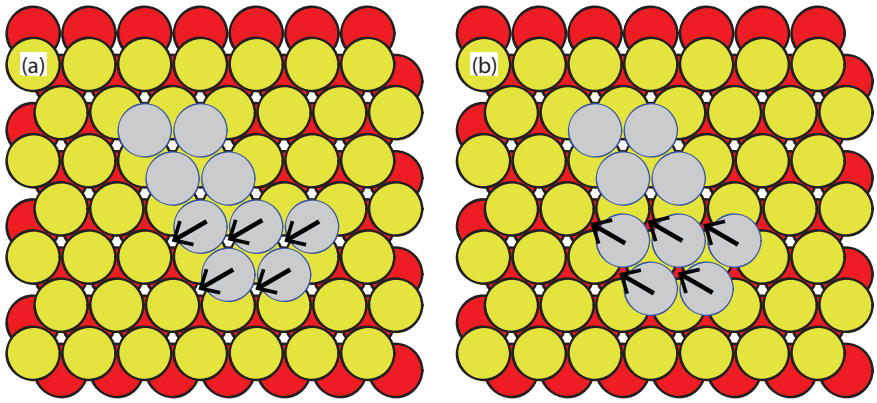

Figure 4.6 An example of reptation mechanism, where part of the island moves from hcp to hcp via fcc in two steps. (a) Step1: Initial state where 9-atom island is on the hcp sites with arrows on 5 atoms showing the reptation direction. (b) Step 2: Final state after step 1 with arrows showing next step of reptation process.

SLKMC-II finds a variety of multi-atom processes, which can be classified into two types: reptation[46, 47] and shearing. Shearing is a single-step process: if the island is on fcc sites, some part of it consisting of at least 2 atoms moves to its nearest fcc sites (If the island sits on hcp sites, some part of it larger than a single atom moves to the nearest hcp sites). Reptation, in contrast, occurs in two steps. In the first step part of the island (larger that one atom) moves in such a way as to create a stacking fault (that is, from fcc to hcp or vice versa). In the second step, parts of the island moves in some way that eliminates the

stacking fault. Figure 4.6 offers an example of a reptation process occurring in a 9-atom island occupying hcp sites. Part of the island, in this case consisting of 5 atoms moves along the path indicated by arrows in Figure 4.6(a) to neighboring fcc sites as shown in Figure 4.6(b). Step two could be completed in four different ways where either the 4 atoms in the island or 5 atoms in the island joins the rest of the island with all atoms occupying the same kind of sites (hcp or fcc). One of the possibilities is shown by arrows in Figure 4.6(b). It should be noted that although energy barrier for reptation processes is lower compared to concerted processes(see Table 4.2), these type of processes are possible only if island changes its shape from compact to non-compact, which is rare at room temperature. Contribution of reptation processes to the island diffusion increases with temperature since the probability of island changing into a non-compact shape also increases with temperature. We note that the two steps of reptation process are stored as individual configurations in the database.

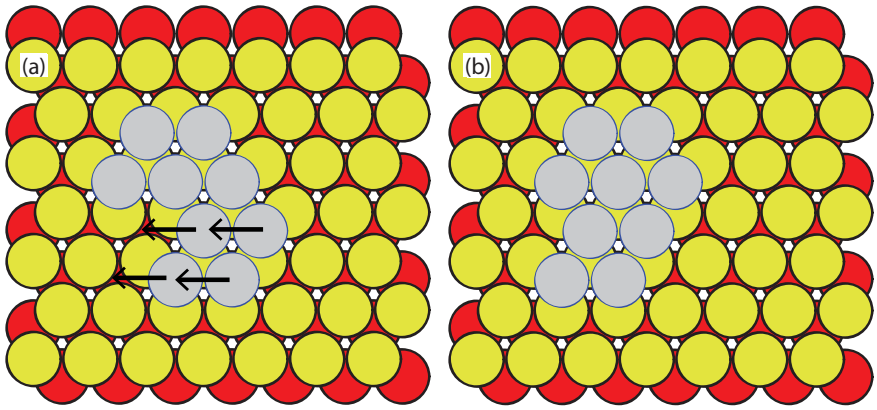

Figure 4.7 Example of a shearing mechanism in which 4 atoms move simultaneously. (a) Initial state of a 9-atom island on hcp sites. The arrows showing the direction of shearing. (b) Final state of the island.

Figure 4.7 shows an example of a shearing process observed during SLKMC-II simulations. In this example, a group of 4 atoms move from hcp to neighboring hcp sites (The simulations also found shearing to occur in islands on fcc sites). A variety of other multi-atom processes are also revealed during our SLKMC-II simulations, specifically, a dimer diffusing around the corner of the island as shown in Figure 4.8. For Ni island diffusion, this process has an activation barriers of 0.320 eV; for Cu it is 0.460 eV and for Ag it is 0.470 eV. Although this process is one of the most frequently picked for 9-atom Ni islands, it does not result in diffusion of the island as a whole.

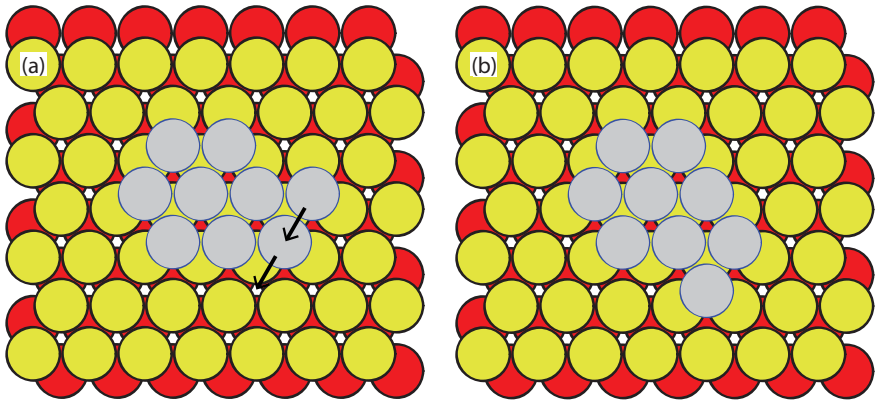

Figure 4.8 Dimer diffusing around the corner of the 9-atom island. (a) Initial state of 9-atom island on fcc sites with arrows on the lower right dimer on the corner of compact hexagon showing the shearing process. (b) Final state of the 9-atom island after dimer on the corner glides to the other side of the hexagon.

4.3.2.3 Single-atom Processes

All single-atom processes possible for the systems under study – edge running, monomer detachment from different steps and corners, kink-detachment, kink-attachment, corner

rounding and whether fcc to fcc or hcp-hcp were also found and stored during our simulations. On fcc(111) surface, there are two types of micro facets, namely (100) micro-facet (also called A step) and (111) micro-facet (also called B step). In all single atom processes, we use the notation Xn→Yn, where X and Y can be different types of steps (A, B), Kink (K), Corner (C) and n represents the number of bonds the atom has before and after the process. One type of single-atom process is an atom's movement along an A (alternatively a B) step edge of the island represented in Table 4.2 as A(B)2→A(B)2. Cu has the lowest barrier for these 2 types of diffusion processes and Ni the highest, the difference between the barriers along the A- and B-step edge is smallest for Cu (0.040 eV) and largest for Ni (0.118 eV). Another type of single-atom process is corner rounding, denoted in Table 4.2 as A(B)2→C1, in which an atom moves from one type of step having 2 bonds to the other (A to B or B to A) by traversing a corner having single bond. Various types of kink attachment and detachment processes, Table 4.2 includes only one: K3→C1, in which an atom detaches to form a corner. Our SLKMC-II database incorporates other types of Kink involving processes like C1→K3, K3→A(B)2, (A(B)2→K3) as well. Figure 4.9 illustrates various types of single atom processes that find a place in our database.

4.4 Conclusions

In KMC simulations, the processes an atom or a collection of atoms can perform depend on the local environment. A pattern-recognition scheme allows KMC simulations to identify this environment, together with the processes possible within it and their respective energy barriers, for on-the-fly storage in and retrieval from a database. Unlike its predecessor, in which only fcc processes were allowed, our new pattern-recognition scheme (which makes possible what we call SLKMC-II) is designed to include processes that involve both fcc and hcp sites on the fcc(111) surface. A key innovation is the inclusion in of top-layer substrate atoms in the recognition scheme, which enables it to distinguish whether a site is hcp or fcc. There are some trade-offs to be taken into account. Because it requires twice the number of rings to cover the same neighborhood as required by its predecessor, additional computational effort is called for during identification (in matching ring numbers). Still, the new scheme is quite simple and easy to implement, quite apart from its enablement of considerably more realistic simulations.

As mentioned earlier, the usage of pattern recognition scheme allows speed up of on-the-fly KMC method by avoiding repetition of saddle point (SP) searches. For example, in the case of the Cu 9-atom island, the database has 2420 configurations with a total of 4041 processes and a total of 10^7 KMC steps were carried out to obtain converged results. One way to interpret these numbers is that each configuration on an average has 2 processes,

which also means that each configuration requires 2 SP searches and each SP search using the drag method takes approximately 54 s. Assuming recycling of events [8], without the pattern recognition scheme 2 SP searches are needed at each KMC step and a total of approximately 10^9 s ($2\times54\times10^7$) will be spent on SP searches. While with the use of the pattern recognition scheme a total of 2.2×10^5 s (4041×54) is spent on SP searches regardless of the number of KMC steps carried out during a simulation. Since the computational time for a KMC step itself is negligible in comparison, a speed up of 4 orders of magnitude is obtained with the usage of pattern recognition scheme.

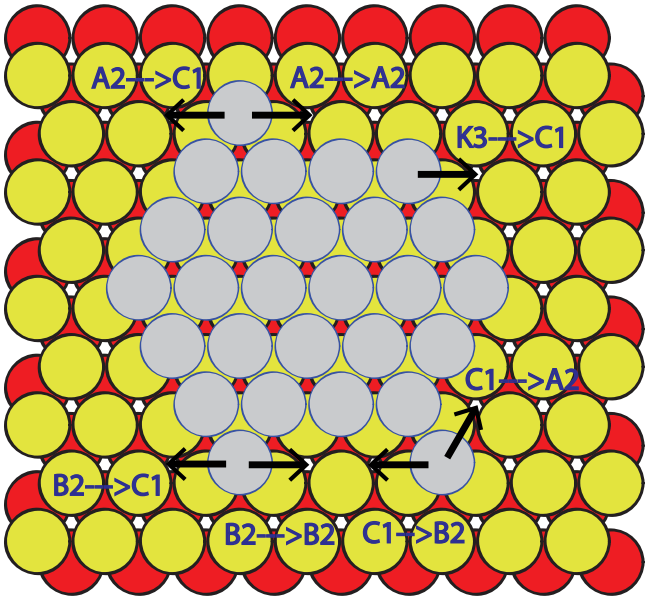

Figure 4.9 Various types of single atom diffusion processes.

We have tested this new pattern recognition by studying 2-D self-diffusion of 9-atom islands of Cu, Ag and Ni on fcc (111) surface. These achievements open the way for further development of pattern-recognition strategies in ways that will extend the reach of KMC

simulation. Although rarely, atoms in small clusters may even in homo epitaxial systems [38] sit on bridge sites. We have found this to be so even in our simulations of small clusters [51]. One way to incorporate such processes is to resort to an off-lattice pattern-recognition scheme [52]. But a better way would be to further refine the pattern-recognition scheme reported here, so as to include bridge sites as well. Though this approach would increase computational expense because more rings would be required in order to identify the neighborhood than are required for distinguishing between fcc and hcp occupancy, it would still be faster than carrying out off-lattice KMC simulations. Secondly, although the pattern-recognition scheme we have described is essentially used to capture 2D neighborhood of an atom, it can be used to describe on-lattice 3D processes as well. Thirdly, as a study we are currently completing will show, the pattern-recognition scheme described here is suitable for doing SLKMC simulations of growth on fcc (111) surfaces. Finally, we note that the idea behind the scheme we have described for the study of self-diffusion on fcc(111) surfaces can be adapted to the study of other surfaces namely (110) and (100). We can also use this method to study hetero systems where adatom-adatom interactions are weaker than adatom-substrate interactions.

CHAPTER 5
SELF-DIFFUSION OF SMALL CLUSTERS ON THE FCC(111) SURFACE: AN SLKMC-II + DFT STUDY

Surface diffusion is of interest not only because it is so different from diffusion in bulk solids [53] but because diffusion of adatoms on metal surfaces, individually or as a group via multi-atom or concerted diffusion processes plays an essential role in a wide variety of such surface phenomena as heterogeneous catalysis, epitaxial crystal growth, surface reconstruction, phase transitions, segregation, and sintering [54]. A precise knowledge of diffusion mechanisms is essential for understanding and control of these phenomena[55]. Adatoms can diffuse on a substrate in a variety of ways, and competition between various types of diffusion processes (due to the differences in their rates) determines the shapes of the islands formed and (on macroscopic times scales), the morphological evolution of thin films. Hence a great deal of effort has been devoted to investigation of self-diffusion of adatom islands on metal surfaces, initially using field ion microscopy (FIM)[56–61] and more recently scanning tunneling microscopy (STM)[62–70]. Because of inherent differences in the microscopic processes responsible for island diffusion on different metal surfaces, this is still an on-going research problem. Both experimental and theoretical studies for various systems have succeeded in finding the activation barriers and prefactors for a single-adatom diffusion processes [14, 71–82]. Ref [53] provides a good survey of those efforts. Here in this chapter, we describe, in a systematic way, the diffusion mechanisms responsible for diffusion of small 2D islands on

the fcc(111) surface of Ni (Cu and Ag have similar mechanisms but their energy barriers are different) and calculate the effective activation barriers for Ni, Cu and Ag. In this work we report our results of doing so for such islands, ranging in size from 1 to 10 atoms.

Arrangement of atoms in the substrate of an fcc(111) surface results in two types of three-fold hollow sites for an adatom: the regular fcc site (with no atom beneath it in the second layer), and an hcp site (with an atom beneath it in the second layer). Occupancy of adatoms at fcc sites maintains the crystal stacking order (ABC stacking) of fcc structure, while occupancy of hcp sites leads to a stacking fault. Depending on its relative occupation energy, which is material dependent, an adatom can occupy one or the other of these sites. Which site is preferred on the fcc(111) surface affects the way diffusion and hence growth proceeds. It is therefore important to understand whether the diffusion proceeds via movement of atoms from fcc-to-fcc or hcp-to-hcp or fcc-to-hcp hcp-to-fcc sites. It has been observed experimetally that for smaller clusters mixed occupancy [13] of fcc & hcp sites is possible.

A host of studies has been devoted to problems of self-diffusion and diffusion mechanisms on metal fcc(111) surfaces, almost exclusively, however, with either a preconceived set of processes or merely approximate activation barriers. It is nevertheless crucial to discover the full range of processes at work and to accurately establish the activation barrier of each. It is also well known that the fcc(111) surface, being atomically flat, has the least corrugated potential energy surface of any fcc surface, resulting in low diffusion barriers even for clusters

to diffuse as a whole. Consequently, studies of diffusion processes on fcc(111) surfaces is a challenging problem for both experiment and simulation even to this day. For a monomer and smaller islands like dimer, trimer and up to certain extent, tetramer, all possible diffusion processes may be guessed. But as islands further increase in size, it becomes more difficult to enumerate all possible diffusion processes *a priori*. An alternative is to resort to molecular dynamics (MD) simulation. But because diffusion processes are rare events, an MD simulation cannot capture every microscopic process possible, as most of the computational time is spent in simulating atomic vibration of atoms. Instead, to do a systematic study of small Ni, Cu and Ag island diffusion on the respective fcc(111) surface we resorted to an on-lattice self-learning kinetic Monte Carlo (SLKMC-II) method, which enables us to study longer time-scales than are feasible with MD yet to find all the relevant atomic processes and their activation barriers on-the-fly, as KMC methods limited to *a priori* set of processes cannot do. Moreover, whereas previous studies have used an on-lattice SLKMC method, [1, 10–12] in which adatoms were restricted to fcc occupancy, in the present study both fcc and hcp occupancies are allowed, and are detectable by our recently developed improved pattern-recognition scheme[19].

The remainder of the chapter is organized as follows. In Section 5.1 we discuss the details of our SLKMC-II simulations, with particular attention to the way we find diffusion processes and calculate their activation barriers using Molecular Static and DFT calculations. In Section 5.2 we present details of concerted, important multi-atom and single-atom

diffusion processes responsible for the diffusion of Ni islands as a function of island size(Cu and Ag islands have similar processes but different energy barriers). In Section 5.3 we present a quantitative analysis of diffusion coefficients at various temperatures and of effective energy barriers as a function of island size for Ni, Cu and Ag systems. In Section 5.4 we present our conclusions.

5.1 Simulation Details

To study small island diffusion on the fcc(111) surface, we carried out SLKMC simulations using the pattern-recognition scheme we developed recently [19] that includes both fcc and hcp sites in the identification of an atom's neighborhood. Various types of diffusion processes are possible, and their activation barrier depends on the atom's local neighborhood. Whenever a new neighborhood around an atom is identified, a saddle-point search (using drag method) 5.1.1 is carried out to find all the possible atomic processes and calculate their activation barriers – provided that it has at least one similar empty site in the second ring [19], since when an atom occupies an fcc (or alternatively an hcp) site, the nearest neighbor (NN) hcp (or, correspondingly, fcc) sites cannot be occupied. In our simulations we used a system size of 16x16x5 with the bottom 2 layers fixed, and carried out saddle-point searches using the drag method 5.1.1.

5.1.1 The Drag Method

In this method a central or active atom is dragged in small steps towards a probable final position. If the central atom is on an fcc (hcp) site, then it is dragged towards a NN vacant fcc (hcp) site in the second ring. Since atoms are allowed to occupy either hcp or fcc sites, an atom being dragged from an fcc (hcp) site to a neighboring similar site is allowed to relax to an intermediate hcp (fcc) site in between the two fcc (hcp) sites. In other words, processes are possible in which atoms in an island may occupy fcc, hcp or both fcc & hcp sites simultaneously.

In the drag method, the atom being dragged is always constrained in the direction of the reaction coordinate but allowed to relax along its other degrees of freedom (those perpendicular to the reaction coordinate), while all the other atoms in the system are allowed to relax in all degrees of freedom. Once the transition state is found, the entire system is completely relaxed to find the final state of the process. The activation barrier of the process is the difference between the energies of the transition and initial states. The current version of drag can automatically detect all types of processes, including shape changing mechanisms for small islands as well, an example of this is the tetramer shearing process mentioned in Sub-section 5.2.4. It should be noted that in a recent study of Cu/Cu(111) [1], the authors did a thorough Molecular dynamics study of small islands from 1-10 atoms making sure that all possible diffusion processes for these islands are indeed mostly concerted processes which

were added by hand in that study. But here in this work all concerted as well as single and multi-atom processes are automatically found by the static calculations with the help of improved pattern recognition scheme.

We have also verified the activation barriers of some of the key processes found by the drag method using the (more accurate but computationally expensive) nudged-elastic band (NEB) method[9] based on EAM interactions as well as using CINEB [32] using *ab initio* DFT calculations, and found no significant difference. For inter-atomic interactions, we used an interaction potential based on the embedded-atom method (EAM) as developed by Foiles *et al.*[29]. In all our SLKMC simulations we used the same pre-exponential factor of 10^{12}s^{-1}, which has been demonstrated to be a good assumption for such systems as the one under examination here.[41, 45]

For the small islands under study here (1-10 atoms), we found that when an atom is dragged rest of the atoms in the island usually follow. For very small islands (1-4 atoms), *all* of the processes identified by the drag method were concerted-diffusion processes. As island size increases we found single-atom and multi-atom processes as well. For islands of size 5-6, even single-atom detachment processes are identified and stored in the database (even though they are not allowed in our simulations). To account for all types of processes associated with both compact and non-compact shapes – especially concerted processes and multi-atom processes – we used 10 rings to identify the neighborhood around an active atom in our SLKMC simulations. Using 10 rings corresponds to including fifth nearest-neighbor

interactions. To make sure we identified all the single-atom processes, we also carried out saddle-point searches with all of the atoms fixed except the atom being dragged. Although there is no infallible method for discovering all possible processes, we did exhaust the search for possible processes identifiable using the drag method. As it is established in a recent work [83, 84] that for larger islands diffusion characteristics are dominated by periphery diffusion, we focus here in this work on the diffusion processes for small islands from 1-10 atoms, which diffuse mainly through concerted processes.

In order to save computational time, we first carried out SLKMC simulations at 700K for each island size, and used the database thus generated to carry out our simulations for the same size at lower temperatures (300, 400, 500 and 600K). The rationale for this approach is that an island goes through many more shapes at higher temperatures: when a simulation is carried out at a lower temperature starting out with a database generated at a higher temperature, it only rarely finds an unknown configuration. It is not possible, however, to economize on computational time by using, for the smaller islands under study here, a database generated for (say) the larger among them, because the types of processes possible (along with their respective barriers) are dependent on an island's particular size.

5.1.2 Energy Barriers Using DFT

As mentioned above, we have verified the energy barriers of some of the concerted processes for the case of Ag/Ag(111) system using CINEB as implemented in the VASP

code [85, 86] employing the projector augmented wave (PAW) [86, 87] and plane-wave basis set methods, setting the kinetic energy cutoff for plane-wave expansion to 500 eV and describing exchange-correlation interaction between electrons by the Perdew-Burke-Ernzerhof functional (PBE) [88]. For all cases, we used slab size of 5x5x4 (for 10 atoms concerted processes we use a 7x7x4 slab) layers with a vaccume of 15 $\mathring{A}$.

We relax all surface structures, using the conjugate-gradient algorithm [89], until all force components acting on each atom smaller than 0.01 eV/Å. In all calculations, after initial relaxation of the slab where all atoms were relaxed, we fix the bottom three layers. In calculating reaction barriers and searching transition states, we first use the Nudged Elastic Band (NEB) method [31] for preliminarily determining a minimum energy path, then apply a Climbing Image Nudged Elastic Band (CI-NEB) [32] calculation. This way of doing NEB and CI-NEB calculations is found to be more efficient for searching transition states than performing CI-NEB alone. Here in, we use the term "(CI-)NEB" to refer a combination of NEB and CI-NEB calculations. In all NEB calculations, we used 7 images in each case.

5.2 Results

As mentioned above, all of the processes for a given island are identified and their activation barriers calculated, and stored in a database on-the-fly. We discuss in this section, however, only key processes of the various general types (concerted, multi-atom and single-

atom) for Ni islands, processes for Cu and Ag are similar except differences in energy barriers and are not reported here, but their diffusivities and effective energy barriers are reported.

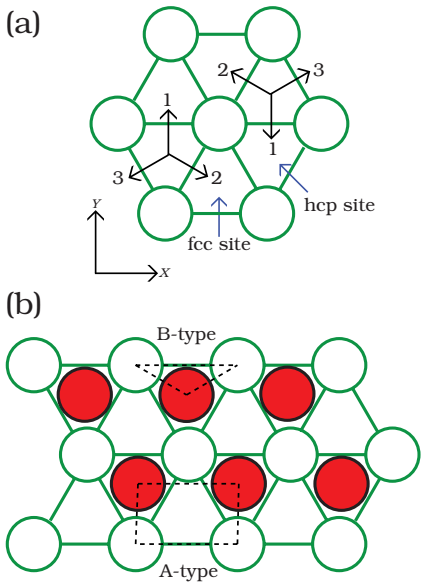

Figure 5.1 (a) fcc and hcp sites on an fcc(111) surface, with corresponding directions for concerted diffusion processes; (b) A-type and B-type step edges (here, for an all-hcp island) for the same surface.

Figure 5.1(a) is a sketch of the fcc(111) surface with its adsorption sites marked as fcc and hcp. Determining whether an adatom is on an fcc or on an hcp site on this surface requires knowledge of at least 2 substrate layers below the adatom layer. In all our figures we show only the adatom layer and the layer below (the top substrate layer) with the convention that the center of an upward-pointing triangle (along the y-axis) formed by the (top layer) substrate atoms is an fcc site, while the center of a downward-pointing triangle is an hcp site. An island on an fcc(111) surface can be on fcc sites or on hcp sites or a combination of both sites (some atoms of the island sitting on fcc sites and the rest on hcp sites). Depending on

the type of material either the fcc or the hcp site will be energetically favorable. As we shall see for each island size under study here, the fcc site for Ni(111) is always at least slightly more favorable than the hcp site.

A compact adatom island on an fcc(111) surface can move in the three directions shown in Figure 5.1(a). Note that the numbering scheme for the directions open to an atom on an fcc site is inverse to that for those open to an atom on an hcp site (see Figure 5.1(a)). We follow the enumeration convention for directions distinguished in Figure 5.1(a) throughout the chapter in tabulating activation barriers for concerted processes for islands of various sizes and shapes. Concerted processes involve all atoms moving together from all-fcc sites to all-hcp sites or vice-versa. In a concerted diffusion process a cluster can either translate in one of the three directions shown in Figure 5.1 (concerted translation) or rotate around an axis (around the center of mass), either clockwise or anti-clockwise (concerted rotation). Since concerted rotational processes do not produce any displacement in the center of mass of an island, they do not contribute to island diffusion. Depending on the size of the island and its shape, activation barriers for the processes in these three directions can be different.

Activation barriers for single-atom processes, however, depend on the type of step-edge along which atom diffuses. Figure 5.1(b) shows, using the example of a 6-atom hcp island, how an A-type step-edge − a (100) micro-step differs from a B-type step-edge − a

(111) micro-step. We discuss important single-atom diffusion processes systematically and in detail in Sub-section 5.2.11.

As island size increases not only does the frequency of single-atom processes increase but the frequency of multi-atom processes does so as well. All multi-atom mechanisms involve shearing. A special case is reptation mechanism[90, 91], a two-step shearing process that moves the cluster from all-fcc to all-hcp sites or the reverse: first, part of the island moves from fcc to hcp sites; then the rest of the island moves from fcc to hcp. Hence at the intermediate stage, the island has mixed fcc-hcp occupancy. In case of Ni-island diffusion, reptation processes occur only when the shape of the island becomes non-compact. We will discuss reptation in detail when we take up islands of size 8-10.

5.2.1 Monomer

As mentioned earlier, much work has been done to determine activation barrier for Ni monomer diffusion on Ni(111) surface[53]. A monomer on fcc(111) surface can adsorb either on an fcc or an hcp site. We find that adsorption of an adatom on an fcc site is slightly favored over than on an hcp site by 0.002 eV – in good agreement with the value reported in Ref [74]. Diffusion of a monomer occurs through hopping between fcc sites via an intermediate hcp site. We find the activation energy barrier for a monomer's hopping from an fcc site to a neighboring hcp site to be 0.059 eV while that for the reverse process is 0.057

eV. The effective energy barrier for monomer is found to be 0.057 eV, which is consistent with the result reported by Liu *et al.*[70] of 0.056 eV.

5.2.2 Dimer

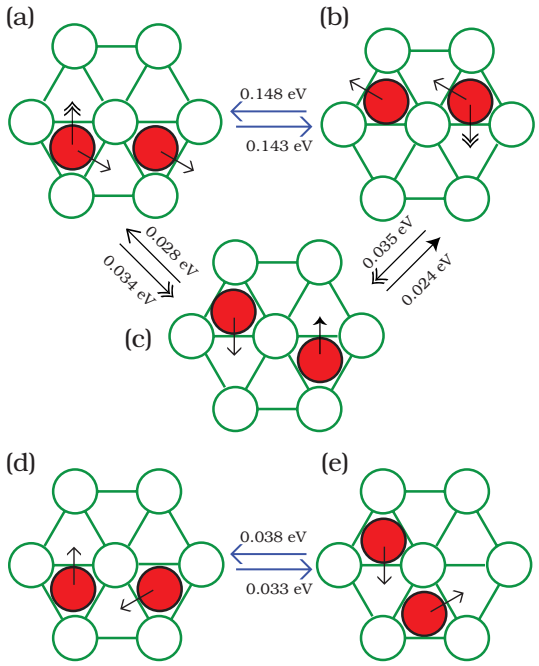

Figure 5.2 Possible configurations for a dimer, with activation barriers for concerted diffusion processes. (a) FF dimer (both atoms on fcc sites); (b) HH dimer (both atoms on hcp sites); (c) FH dimer (one atom on an fcc and the other on an hcp site); (d) FF dimer in concerted clockwise rotation and (e) HH dimer in concerted counter-clockwise rotation.

On any fcc(111) surface a dimer (of the same species) can have three possible arrangements: both atoms on fcc sites (an FF-dimer, Figure 5.2(b)), both on hcp sites (an HH-dimer, Figure 5.2(a)) or one atom on an fcc and the other on an hcp site (an FH-dimer, Figure 5.2(c)). We find that the FF-dimer is energetically more favorable than the HH-dimer

by 0.005eV and the FH-dimer the least favorable by 0.011 eV. We find that both FF and HH dimers diffuse via concerted as well as single-atom processes, whereas the FH-dimer diffuses via single-atom processes only. In concerted diffusion processes, both atoms in a FF (HH) dimer move from fcc (hcp) to the nearest hcp (fcc) sites as shown in Figure 5.2 (a)&(b) and Figure 5.2 (d)&(e), thereby converting an FF (HH) dimer into an HH (FF) dimer. In the case of an FF (HH) dimer, the activation barrier for concerted translational (Figure 5.2 (a)&(b)) is 0.148 eV (0.143 eV) while that for concerted rotation (Figure 5.2 (d)&(e)) is 0.038 eV. In concerted dimer rotation, the activation barriers for both clockwise and anti-clockwise directions are the same, as they are symmetric to each other. Activation barriers for translational concerted diffusion processes in all three directions (see Figure 5.1) both for FF and HH dimers are reported in . Table 5.1. Our results for concerted processes are 0.028 eV higher than the corresponding activation barriers for a dimer reported in Ref. [70]. (This difference − as with those in what follows − may be due to the different inter-atomic potential employed in their study and ours.)

Table 5.1 Activation barriers (in eV) of concerted processes for dimer diffusion.

Direction	fcc	hcp
1	0.071	0.066
2	0.148	0.143
3	0.148	0.143

Single-atom processes transform both FF and HH dimers into an FH-dimer. In this case one of the fcc atoms in an FF-dimer or an hcp atom in an HH-dimer moves to a

nearest-neighbor hcp or an fcc site respectively, as shown in Figure 5.2 (a)&(b) with the double-headed arrow. The activation barriers are 0.034 eV and 0.035 eV for hcp and fcc dimer, respectively. In the case of an FH-dimer, two types of single-atom diffusion processes are possible, as shown in Figure 5.2: an fcc atom moves to the nearest hcp site in the direction of the open arrowhead, forming an HH-dimer, or an hcp atom moves in the direction of the solid arrowhead to the nearest fcc site, forming an FF-dimer. The activation barriers for these processes are 0.028 eV and 0.024 eV, respectively.

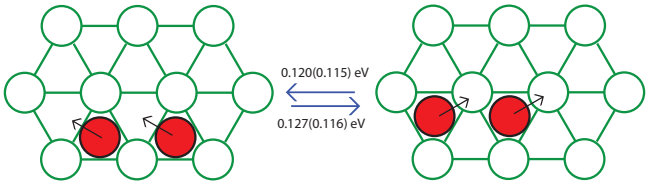

Figure 5.3 Concerted processes for Ag dimer, with activation barriers from CINEB, using DFT calculations. Values in bracket are from EAM calculations. (a) FF dimer, both atoms move from fcc to hcp sites; (b) HH dimer, both atoms move from hcp to fcc sites.

For the case of Ag/Ag(111) and Cu/Cu(111) systems, we find similar processes with different energy barriers. We also did CINEB calculations using DFT for the concerted process for Ag dimer as shown in Figure 5.3. As can be seen from Figure 5.3, the energy barriers using DFT and EAM (values in brackets) based interactions agrees very well.

5.2.3 Trimer

Depending on where a third atom is attached to the dimers shown in Figure 5.2(a & b), there are four possible arrangements of atoms in a compact trimer: two types of fcc timers

– one centered around an hcp site (F3H), the other centered around a top site (F3T) (see Figs. Figure 5.4(a) & (d)) – and two types of hcp trimers – one centered around an fcc site (H3F), the other centered around a top site (H3T) (Figs. Figure 5.4(c) & (b)). Although all four trimers have the same shape, their local environment is different, so that their adsorption energies are distinct, as are the activation barriers for their possible diffusion processes. F3T trimer is the most energetically favorable: F3H, H3T and H3F are less energetically favorable by 0.006, 0.007 and 0.0013 eV, respectively. It should also be noted that although trimers can take on non-compact shapes, the configurations depicted in Figure 5.4 are the most frequently observed in our trimer simulations.

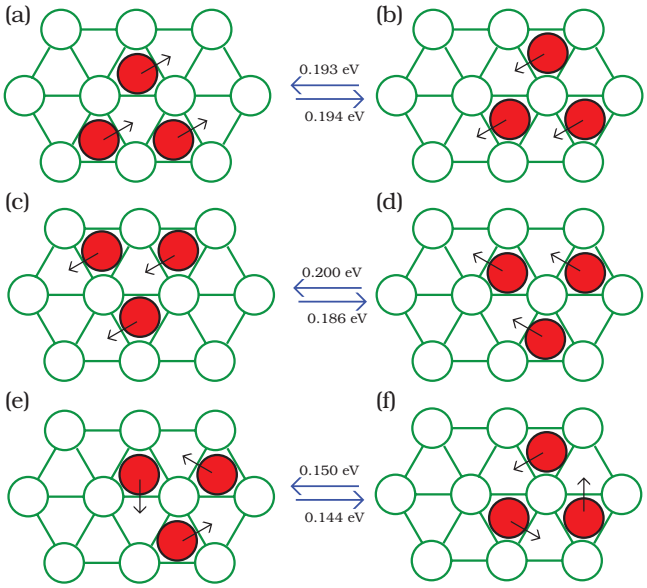

Figure 5.4 Possible arrangements of atoms in a trimer, with possible concerted diffusion processes and their activation barriers. (a)–(d) Concerted translation: (a) F3H-all atoms on fcc sites centered around an hcp site; (b) H3T-all atoms on hcp sites centered around a top site; (c) H3F-all atoms on hcp sites centered around an fcc site; (d) F3T-all atoms on fcc sites centered around a top site. (e) & (f) Concerted rotation: F3T and H3T respectively.

In the case of F3T and H3T trimers, two types of concerted processes were observed, a non-diffusive concerted rotation (clockwise and anti-clockwise) (Fig Figure 5.4 (e) & (f)) and a diffusive concerted translation (in all three directions) (Fig Figure 5.4 (d) & (b)). Concerted rotation processes transform an H3T trimer into a F3T trimer and vice versa. The activation barrier for the concerted rotation processes for F3T trimer is 0.150 eV while that for those of the H3T trimer is 0.144 eV. Translation transforms an F3T timer into a H3F timer and vice versa. The activation barrier for the concerted translations possible for these two trimers are 0.200 eV and 0.193 eV for F3T and H3T, respectively. The activation barrier of 0.200 eV for translational motion of F3T trimer is in agreement with the value reported in Ref [70]. For F3H and H3F trimers, only concerted translation processes are possible; their activation barriers are 0.194 eV and 0.186 eV (the value reported for the same process in Ref [70] is 0.187 eV), respectively. Figure 5.4 (a-b) & (c-d) reveal that these concerted diffusion processes transform an F3H into an H3T trimer and an H3F to an F3T trimer. Since the shape of these trimers is symmetric (see Fig Figure 5.4 (a) & (c)), the activation barriers for their diffusion in all 3 possible directions are the same.

Table 5.2 Activation barriers (in eV) for single-atom diffusion processes for an H3T compact trimer in the directions shown in Figure 5.5.

Type	1	2	3	4
F3T	0.439	0.858	0.858	0.439
F3H	0.432	0.875	0.875	0.432
H3T	0.436	0.856	0.856	0.436
H3F	0.429	0.872	0.872	0.429

As for single-atom processes in the case of a trimer: an atom can move in 4 different directions as shown in Figure 5.5, resulting 2 different types of single-atom processes: directions 1 & 4 correspond to edge-diffusion processes which open up the trimer; directions 2 & 3 correspond to detachment processes (excluded from the present study, which is confined to diffusion of single whole islands, in which an island's integrity [and hence its size] is maintained). We note that these processes move atoms from fcc (hcp) to nearest fcc (hcp) site. Activation barriers for processes in these 4 directions for different types of trimers are given in . Table 5.2. Because these activation barriers are so high relative to those for concerted processes, single-atom processes were rarely observed in our simulations of trimer diffusion.

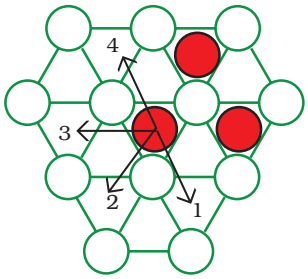

Figure 5.5 Single-atom processes possible for an H3T trimer. Activation barriers for the processes in these 4 directions for the 4 posible trimer configurations are given in . Table 5.2

We note that as island size increases, possible types of single-atom processes increases as well (though with the decamer, basically all possible types have appeared). Accordingly, it is convenient to defer detailed discussion of single-atom processes until later (Sub-section. 5.2.11)

5.2.4 Tetramer

Adding another atom to any of the trimers shown in Figure 5.4 (a - d) results in the formation of a compact tetramer, diamond-shaped − with a long diagonal (along the line joining farthest atoms) and a short one (perpendicular to the long one), as shown in Figure 5.6. Once again the fcc island (Figure 5.6(a)) is energetically more favorable than the hcp one − in this case, by 0.009 eV. Three types of translational concerted diffusion processes are possible for each of the fcc and hcp tetramers, that is, one along each of the three directions specified in Figure 5.1. An example of a concerted fcc-to-hcp process (along direction 1) for a tetramer is shown in Figure 5.6(a); its activation barrier is 0.213 eV. The reverse process (hcp to fcc) is shown in Figure 5.6(b); its activation barrier is 0.204 eV (the value reported in Ref. 18 is 0.210 eV). Because the process in direction 3 is symmetric to that in direction 1, the energy barriers for these processes are identical, as are those for the reverse processes. The energy barrier along direction 2 is 0.313 eV from fcc to hcp and 0.304 eV from hcp to fcc. These values are systematically displayed in Table 5.4.

Table 5.3 Diffusion coefficients (($Å^2$/s) at various temperatures, for 4-atoms island using database with only single atom processes (Row 1) and all processes (Row2) along with effective energy barriers.

Process Types	300K	400K	500K	600K	700K	E_{eff} (eV)
Single atom Only	0.02×10^{00}	4.18×10^{01}	4.55×10^{03}	1.13×10^{05}	1.14×10^{06}	0.807
All	7.33×10^{08}	6.24×10^{09}	2.03×10^{10}	4.80×10^{10}	9.04×10^{10}	0.216

The multi-atom processes shown in Figure 5.6(c & d) have activation barriers lower than those of single-atom processes. In these multi-atom processes, two atoms move together

in the same direction, the result is a shearing mechanism as shown in Figure 5.6(c) & (d) and is automatically revealed during the simulations. For this shearing process, from fcc to hcp, the activation barrier is 0.285 eV; that for the reverse process from hcp to fcc is 0.276 eV. The drag method also finds single-atom processes, but because in tetramers (as in islands of size $3-7$) these have higher activation barriers than those of concerted processes, they were not observed during the simulations.

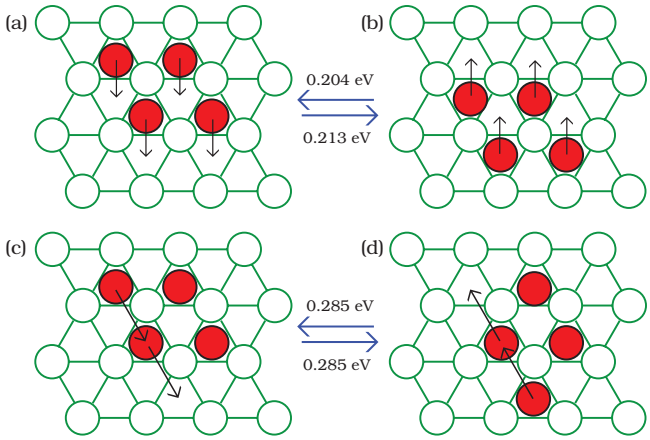

Figure 5.6 Diffusion processes possible for a tetramer: (a) & (b) concerted diffusion along the short diagonal; (c) & (d) shearing processes.

In order to emphasize the importance of different classes of processes for small island diffusion, we present in Table 5.3, the results for diffusion coefficients and effective energy barriers for 4 atoms island in the case when island diffuse through single atoms processes only and when it diffuses through all types of processes, including single atom as well. As can be seen from Table 5.3, the diffusion characteristics for the two cases are entirely different.

Hence in order to get accurate diffusion characteristics, we need to have as complete set of transition rates as possible.

Table 5.4 Activation barriers (eV) for the concerted tetramer translation processes shown in Figure 5.6(a)&(b).

Direction	fcc	hcp
1	0.213	0.204
2	0.313	0.304
3	0.213	0.204

5.2.5 Pentamer

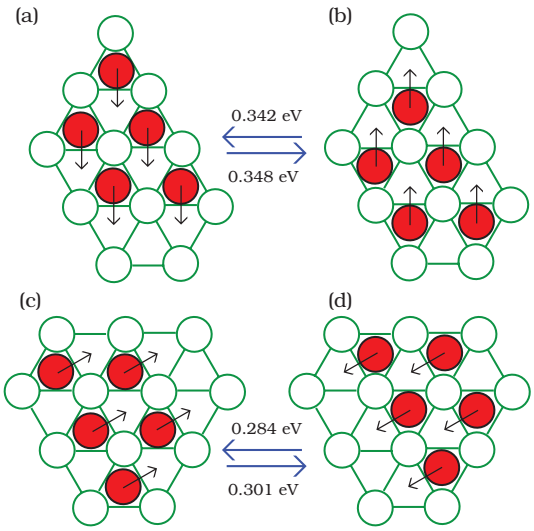

Figure 5.7 Examples of concerted diffusion processes for a compact pentamer, along with their activation barriers.

The compact shapes of a pentamer can be obtained by attaching an atom to a diamond-shaped tetramer. Although the geometries of compact pentamer clusters thus obtained are the same, the island's diffusion is crucially affected by where this additional atom

is placed: attachment of an atom to an A-type step-edge of an fcc tetramer results in the long A-type step-edge pentamer shown in Figure 5.7(c); attachment of an atom to a B-type step-edge of the same tetramer results in the long B-type step-edge pentamer shown in Figure 5.7(a)); the corresponding results of attaching an atom to an hcp tetramer are shown in Figs. Figure 5.7(b) and (d), respectively. The most energetically favorable of these is the fcc pentamer with a long A-type step-edge (Figure 5.7(c)); less favorable by 0.005 eV are the fcc pentamer with a long B-type step-edge (Figure 5.7(a)), by 0.011 eV the hcp pentamer with a long A-type step-edge, and by 0.017 eV the hcp pentamer with a long B-type step-edge. That is: as usual, fcc islands are more s than hcp ones. And, within each of those types, pentamers with a long A-type step-edge are more s than those with a long B-type step-edge.

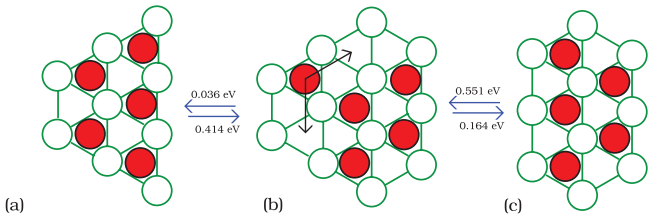

Figure 5.8 The single-atom processes that convert the long A-type step-edge pentamer to the long B-type step-edge pentamer.

In our simulations we found that compact pentamers diffuse mostly via concerted diffusion processes, which displace the island as a whole from fcc-to-hcp or vice-versa. Figure 5.7 shows concerted diffusion processes along direction 1 for the long B-type step-edge pentamer and along direction 3 for the long A-type step-edge pentamer. Table 5.5 displays activation barriers for concerted processes in all 3 directions for both types of pentamer. Figure 5.8 (a),(b) & (c) shows the single-atom processes that transform an fcc pentamer from long A-type (= short B-type) to a short A-type (= long B-type) cluster, with the activation barrier for each.

Table 5.5 Activation barriers (eV) without parentheses are for concerted-translation processes of pentamers with a long A-type step-edge, as shown in Figs. Figure 5.7 (c)&(b); barriers in parentheses are for such processes for pentamers with a long B-type step-edge, as shown in Figs. Figure 5.7 (a)&(d).

Directions	fcc A (B)	hcp A (B)
1	0.348 (0.301)	0.342 (0.284)
2	0.348 (0.353)	0.342 (0.337)
3	0.295 (0.353)	0.289 (0.337)

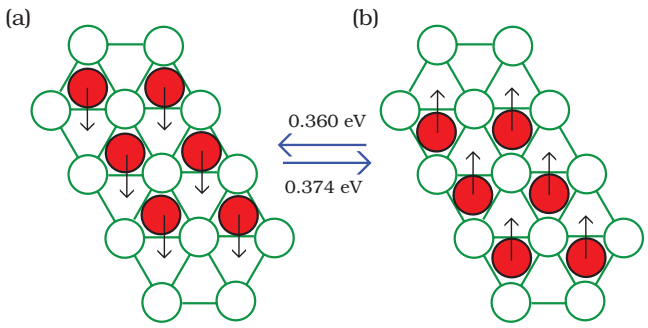

Figure 5.9 Parallelogramic hexamers obtained by extending (by one atom) the shorter edge of either the long A-type or long B-type pentamers: (a) fcc cluster; (b) hcp cluster. The activation barriers indicated are for concerted diffusion in direction 1.

5.2.6 Hexamer

Depending on whether a sixth atom is attached to a long A-type or to a long B-type step-edge pentamer, there are 3 possible compact shapes for a hexamer: (1) when an atom is added in such a way as to extend the shorter edge of either a long A-type or a long B-type step-edge pentamer, the result is one of the parallelogramic hexamers shown in Figure 5.9; (2) when an atom is attached to the long edge of either type of pentamer, the result is the one of the irregular hexamers shown in Figure 5.10; (3) when an atom is added to the shorter edge of either type of pentamer, the result is one of the triangular hexamers with all step edges of either the A-type (Figure 5.11(b) &(c)) or of the B-type (Figure 5.11(a) &(d)). Table 5.6 shows the order of relative stabilities of the hexamers most frequently observed in our simulations. It reveals that, for *a given shape*, hexamers on fcc sites are more energetically favored than those on hcp sites, and that among hexamers on fcc sites (as for those on hcp sites), clusters in which A steps are longer than B steps.

Figure 5.9-Figure 5.11 also show concerted diffusion processes (in direction 1) for these hexamers, together with the activation barriers for each. Table 5.7 & **??** give activation barriers for the hexamers shown in Figure 5.9 & Figure 5.10, respectively. Since triangular hexamers (Figure 5.11) are symmetric, their activation barriers for concerted diffusion are same in all three directions.

Table 5.6 Relative stabilities of the hexamers most frequently observed in our simulations. P = Parallelogram; I = Irregular; T = Triangular.

Type	Shape	Description	Energy (eV)	Reference
fcc	P	equal A & B steps	0	Figure 5.9(a)
fcc	I	edge atom on A step	0.011	Figure 5.10(b)
fcc	I	edge atom on B step	0.011	not shown
hcp	P	equal A & B steps	0.014	Figure 5.9(b)
fcc	T	all A steps	0.019	Figure 5.11(c)
hcp	I	edge atom on B step	0.024	Figure 5.10(b)
hcp	I	edge atom on A step	0.024	not shown
fcc	T	all B steps	0.029	Figure 5.11(a)
hcp	T	all A steps	0.032	Figure 5.11(b)
hcp	T	all B steps	0.042	Figure 5.11(d)

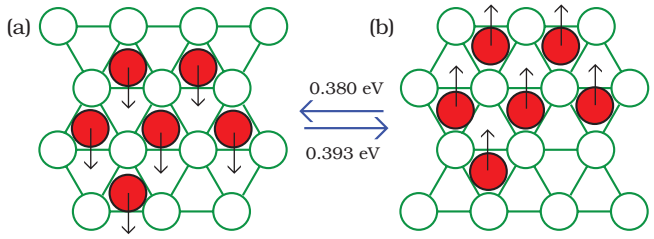

Figure 5.10 Irregular hexamers obtained by attaching an atom to the long edge of a pentamer: (a) fcc cluster; (b) hcp cluster. The activation barriers indicated are for concerted diffusion in direction 1.

Figure 5.13 shows the most frequently observed multi-atom processes for a hexamer – shearing processes in which a dimer moves along the A-type step-edge of the cluster from sites of one type to the nearest-neighbor sites of the same type. Figs. Figure 5.13 (a) & (b) show this kind of diffusion process for an hcp cluster and Figs. Figure 5.13 (c) & (d) for an fcc cluster. Although this dimer shearing process does not much displace the center of mass of a hexamer; it does have a striking consequence: it converts a parallelogramic hexamer (Figure 5.9) into an irregular hexamer (Figure 5.10) and vice-versa.

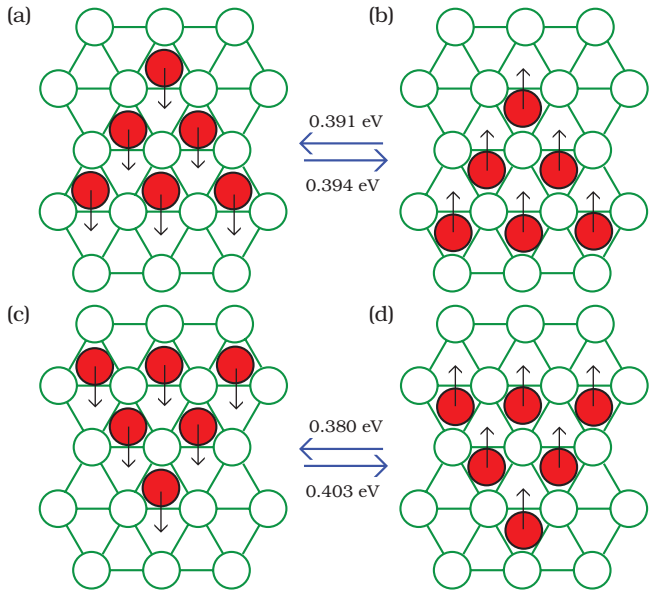

Figure 5.11 Triangular hexamers obtained by adding an atom to the short edge of a pentamer: (a) fcc hexamer with B-type step edges; (b) hcp hexamer with A-type step edges; (c) fcc hexamer with A-type step edges; (d) hcp hexamer with B-type step edges. The activation barriers here are for concerted diffusion in direction 1.

Table 5.7 Activation barriers (eV) of the concerted translation processes in all three directions for the hexamer shown in Figure 5.9

Directions	fcc	hcp
1	0.374	0.360
2	0.466	0.451
3	0.254	0.240

5.2.7 Heptamer

On an fcc(111) surface, an heptamer has a compact closed-shell structure with each edge atom having at least three nearest-neighbor bonds, as shown in Figure 5.14. Our SLKMC simulations (keep in mind here the range of temperatures to which they were confined) found that heptamer diffuses exclusively via concerted diffusion processes, which dis-

place the cluster from fcc-to-hcp and vice versa; the barriers for which are shown in Figure 5.14. That these processes will predominate can also be concluded from the fact that the effective energy barrier for heptamer diffusion (cf. Table 5.12) is close to the average of the activation barriers shown in Figure 5.14.

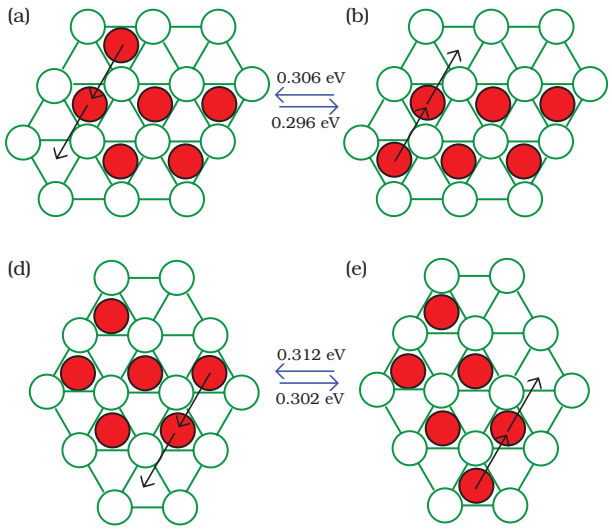

Figure 5.12 Dimer shearing processes in case of a hexamer along with their activation barriers: (a) & (b) all-hcp hexamers; (c) & (d) all-fcc clusters.

Since the compact heptamer has a symmetric shape, activation barriers in all three directions are the same as those shown in Figure 5.14. Again, the fcc island is more energetically favorable than its hcp counterpart – in this case by 0.015 eV.

For the case of Ag heptamer, DFT calculations using CINEB agrees very well with EAM based NEB calculations (values in brackets) as shown in Figure 5.15.

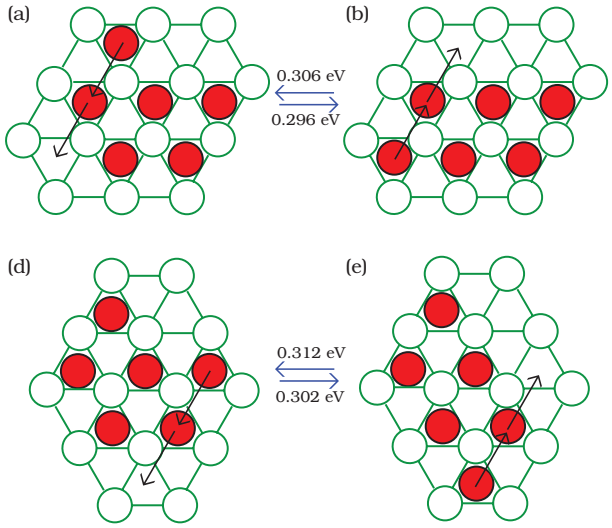

Figure 5.13 Dimer shearing processes in case of a hexamer along with their activation barriers: (a) & (b) all-hcp hexamers; (c) & (d) all-fcc clusters.

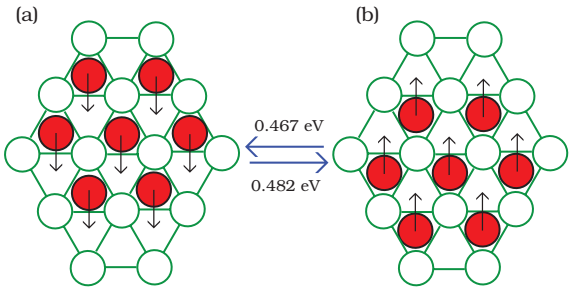

Figure 5.14 Concerted diffusion processes and their activation barriers in direction 1 for a heptamer.

5.2.8 Octamer

Compact octamers have two distinct orientations, one with two long A-type step-edges, the other with two long B-type step-edges, as shown in Figure 5.16 (a) & (b) for an fcc octamer. Octamers with long A-type step-edges (Figure 5.16 (a)) can be obtained by attaching an atom to any B-type step-edge of a compact heptamer, while a compact octamer

with long B-type step-edges results from attaching one to any A-type step-edge. Again: the fcc islands are more energetically favorable than the hcp ones, and within each type, islands with long A-type step edges are more stable than those with long B-type step-edges.

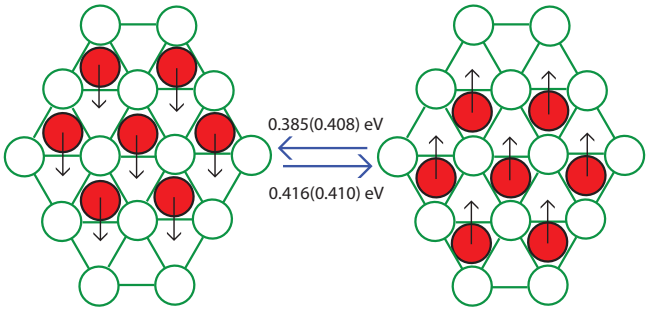

Figure 5.15 Concerted diffusion processes and their activation barriers, using DFT based CINEB and EAM based NEB calculations (values in brackets), in direction 1 for a Ag heptamer.

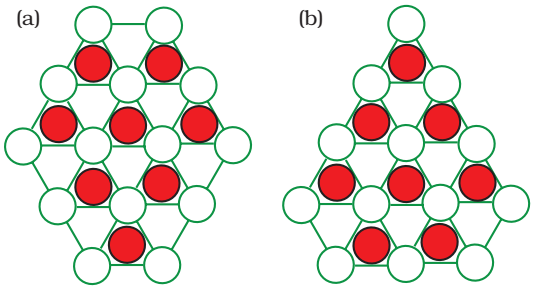

Figure 5.16 Possible orientations for a compact fcc octamer: (a) with long A-type step edges; (b) with long B-type step edges.

A compact octamer diffuses via concerted diffusion processes, as shown in Figure 5.17. The activation barrier of a concerted diffusion process depends on whether the octamer has long A- or long B-type step-edges. As Figure 5.17 shows, a concerted diffusion process converts a long A-type step-edge fcc octamer into a long B-type step-edge hcp cluster, and vice-versa. Table 5.8 reports the activation barriers for concerted diffusion processes in all

3 directions for both orientations for an fcc as well as an hcp (see Figure 5.16) octamer. Concerted diffusion processes in directions 2 and 3 are the most frequently observed processes in octamer diffusion.

Although an octamer diffuses primarily via concerted processes we found in our simulations that both multi-atom and single-atom processes are also relatively common. As mentioned before, we defer comprehensive discussion of single-atom processes to section 5.2.11. Here we discuss multi-atom processes particular to octamers.

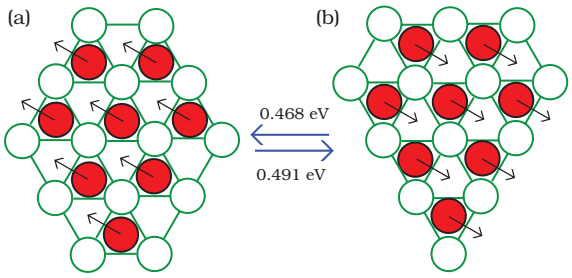

Figure 5.17 Examples of concerted diffusion processes in direction 2 for an octamer: (a) compact fcc octamer with long A-type step-edges; (b) compact hcp octamer with long B-type step-edges.

Table 5.8 Activation barriers (in eV) of the twelve concerted diffusion processes for compact octamers.

Directions	fcc	hcp
	A (B)	A (B)
1	0.589 (0.585)	0.567 (0.571)
2	0.491 (0.484)	0.468 (0.469)
3	0.491 (0.484)	0.468 (0.469)

Multi-atom processes involving shearing and reptation are shown in Figs. Figure 5.18 & Figure 5.19, respectively. In shearing processes, *part* of the island (more than one atom)

moves from fcc to the nearest fcc sites, if all the island is initially on fcc sites – or from hcp to hcp sites, if all of it initially sits on hcp sites. Figure 5.18 (a) & (b) show trimer shearing processes within an octamer, along with their activation barriers, while Figure 5.18 (c) & (d) show dimer shearing processes, with their activation barriers.

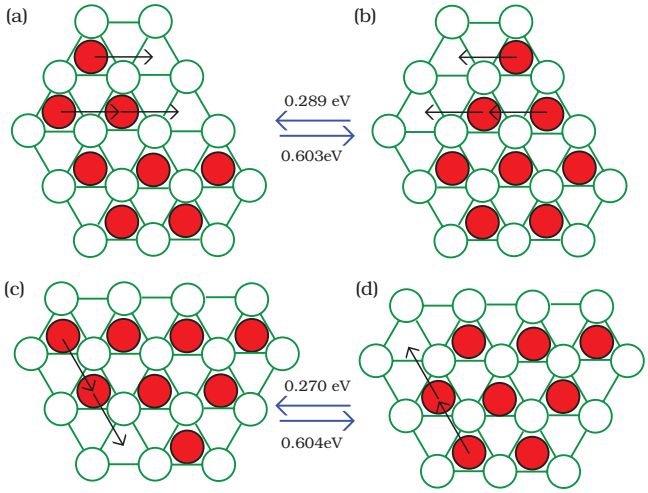

Figure 5.18 Example of shearing diffusion processes within an octamer along with their activation barriers.

Reptation is a 2-step diffusion process. In the case of an fcc island, the entire island diffuses from fcc to nearest-neighbor hcp sites in two steps. In the first, part of the island moves from fcc to nearest-neighbor hcp sites, leaving part of the island on fcc sites and part on hcp sites. In the next, the remainder of the island initially on fcc sites moves to hcp sites. Figure 5.19 (a)-(d) shows various steps (subprocesses) of a reptation process, with their activation barriers.

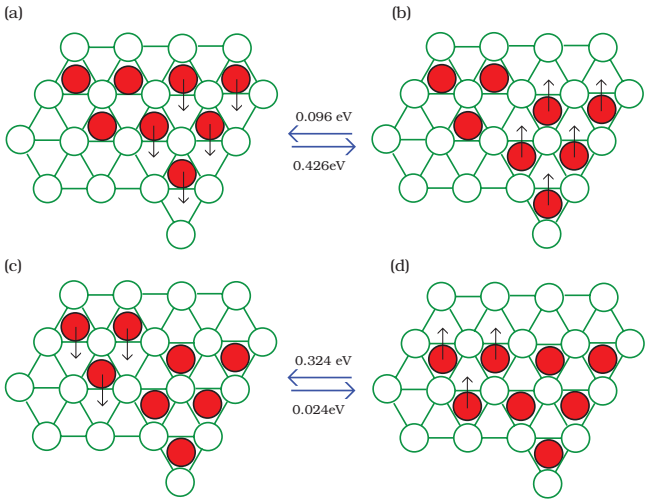

Figure 5.19 Successive sub-processes (or steps) involved in an octamer reptation diffusion mechanism.

5.2.9 Nonamer

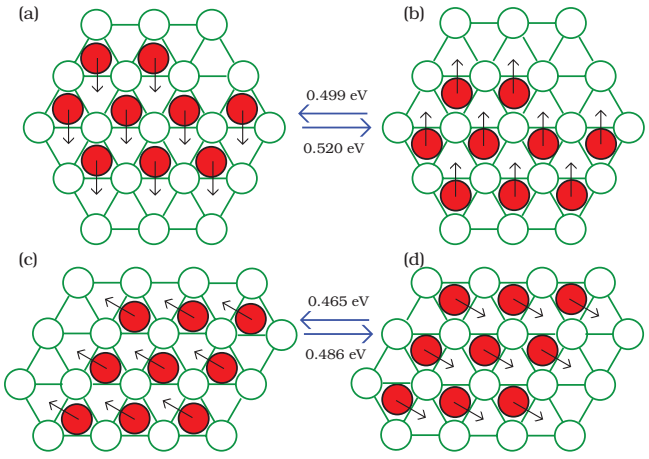

Figure 5.20 Concerted diffusion processes and their activation barriers for nonamers.

For a nonamer, we observed all types of diffusion processes – single-atom, multi-atom and concerted. The most frequently observed were two types of single-atom mechanisms: edge-diffusion processes along an A- or a B-type step-edge and corner rounding (Figure

5.24). The nonamer is the smallest island for which concerted processes are not the most frequently picked (the concerted processes for the most frequently observed nonamer configurations [compact or nearly so] are shown in Figure 5.20). Even so, concerted processes contribute the most to *island* diffusion: that is, the displacement they produce in the nonamer's center of mass is far greater than that produced by single-atom processes, despite the far greater frequency of the latter. This is reflected in the fact that the effective energy barrier for nonamer (cf. Table 5.12) is much closer to the average activation barrier for concerted processes (cf. Table 5.9) than for that of single-atom processes (cf. Table 5.9). The fact that the effective activation barrier is slightly higher than the average energy barrier for concerted processes is due mainly to the contribution of kink processes, which do contribute somewhat to island diffusion.

The most frequently observed multi-atom processes are the four forms of dimer shearing along an A-type step-edge shown in Figure 5.21(c)-(f), as have been discussed above for island of sizes 6 & 8. The activation barriers for these dimer shearing processes are lower than those for single-atom diffusion processes along an edge and also for some corner rounding processes. Reptation processes also show up, but only when the nonamer is non-compact (we do not illustrate these here) [19].

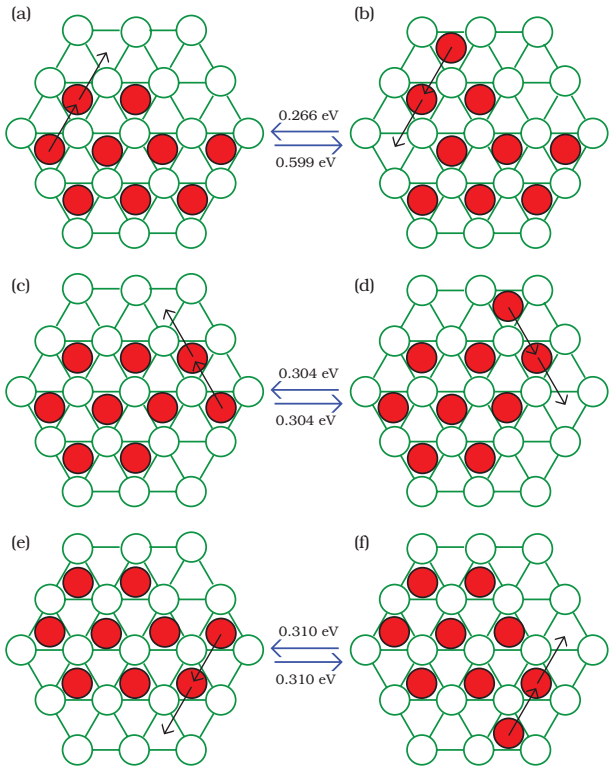

Figure 5.21 Dimer shearing processes and their activation barriers for compact nonamers.

Table 5.9 Activation barriers (eV) of concerted translations processes in all 3 directions for the nonamers shown in Figure 5.20(a–d).

Directions	fcc (a)	hcp (b)	fcc (c)	hcp (d)
1	0.520	0.499	0.486	0.465
2	0.626	0.605	0.486	0.465
3	0.605	0.583	0.693	0.672

5.2.10 Decamer

Even in the case of a decamer, we have observed single-atom, multi-atom and concerted diffusion processes. Single-atom diffusion processes are the most frequently observed.

The most frequently observed compact shape of decamer during our simulations is that shape shown in Figure 5.22, which has the same number of A- and B-type step edges. As usual, an fcc cluster is energetically more favorable than an hcp cluster.

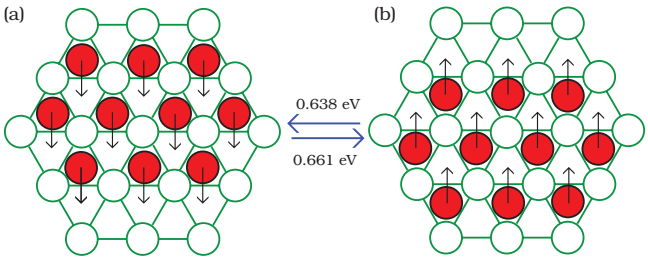

Figure 5.22 Frequent concerted diffusion processes and their activation barriers for compact decamers.

For the shape shown in Figure 5.22, the most frequently observed concerted diffusion processes are those shown in the same figure, along with their activation barriers reported in Table 5.10. It can be seen from the Table 5.12, that the effective energy for decamer diffusion is close to that of the average energy barrier of these concerted processes. That is why decamer diffusion is dominated by concerted processes.

Table 5.10 Activation barriers (eV) of concerted diffusion processes in all 3 directions of decamer as shown in Figure 5.22 (a) & (b).

Directions	fcc	hcp
1	0.661	0.638
2	0.700	0.677
3	0.700	0.677

As with the nonamer, a decamer also undergoes multi-atom processes (shearing and reptation). Of these, the most frequently observed is dimer shearing along an A-type step-

edge, similar to what has been discussed for clusters of size 6, 8 and 9. Figure 5.23 shows the sub-processes in a reptation process, along with the activation barrier of each.

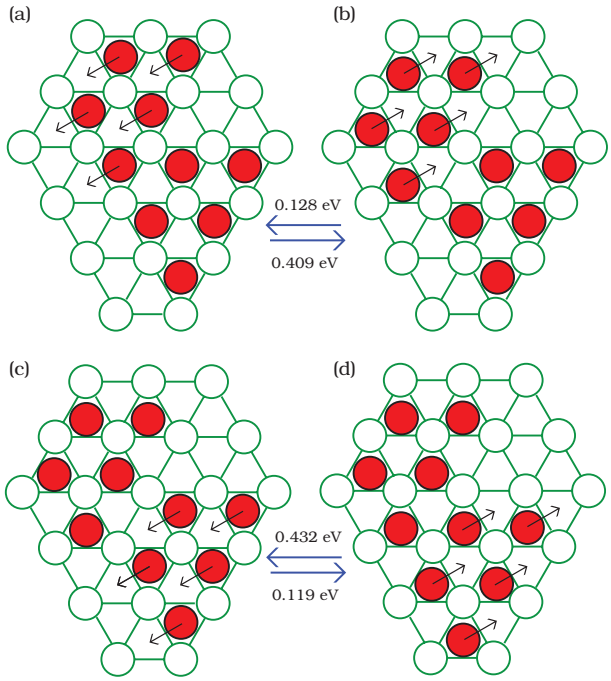

Figure 5.23 Diffusion steps (sub-processes) in decamer reptation. Note that the decamers in (b) and (c) are identical, though the arrows indicate different processes.

5.2.11 Single-atom Processes

In this section we provide detail about single-atom processes: edge-diffusion, corner rounding, kink attachment, and kink detachment, as shown in Figure 5.24 for an hcp island. Their corresponding activation barriers and those for their fcc analogues are given in Table 5.11. In each single-atom process, an atom on an fcc site moves to a nearest-neighbor fcc site, while an atom on hcp site moves to a nearest-neighbor hcp site. The activation barriers

for single-atom processes depend not only on whether the atom is part of an fcc island or an hcp island, but also on whether the diffusing atom is on an A-type or a B-type step-edge.

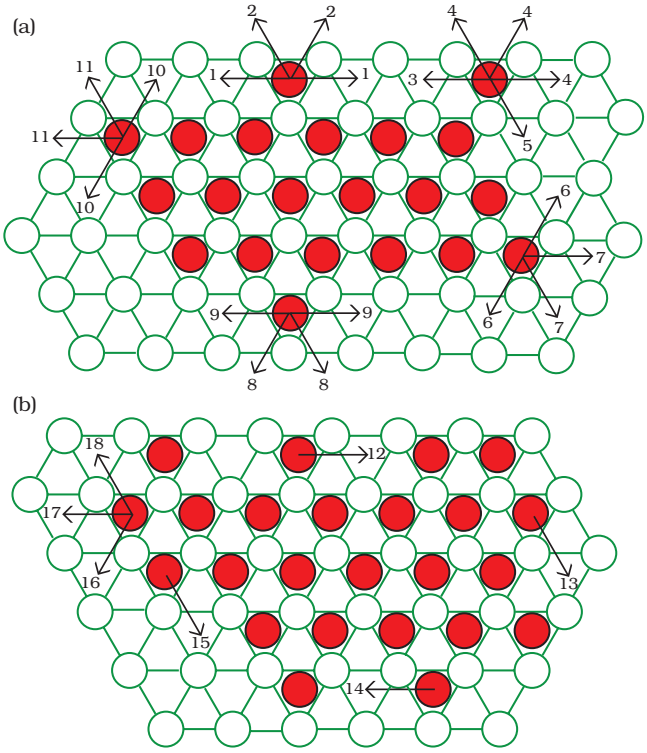

Figure 5.24 Single-atom processes for an hcp island (Though analogous processes occur for an fcc island, we do not illustrate them here). The index numbers designate the processes described in Table 5.11, which gives the activation barriers for each.

In classifying single-atom processes in Table 5.11 we have used the notation $X_{n_i}U \rightarrow Y_{n_f}V$, where where X or Y = A (for an A-type step-edge) or B (for a B-type step-edge) or K (for kink) or C (for corner) or M (for monomer); n_i = the number of nearest-neighbors of the diffusing atom before the process; n_f = the number of that atom's nearest neighbors after the process. U or V = A or B (for corner or kink processes) or null (for all other other process types).

Table 5.11 Activation barriers (eV) of single-atom processes for both fcc and hcp islands. The index numbers refer to the types of processes illustrated in Figure 5.24. See text for explaination of the notation used to classify the process types.

Index no.	Process type	fcc	hcp
1	$B_2 \rightarrow B_2$	0.454	0.448
2	$B_2 \rightarrow M$	0.821	0.815
3	$C_1B \rightarrow B_2$	0.177	0.173
4	$C_1B \rightarrow M$	0.458	0.455
5	$C_1B \rightarrow A_2$	0.040	0.038
6	$C_1B \rightarrow C_1B$	0.540	0.585
7	$C_1B \rightarrow M$	0.811	0.809
8	$A_2 \rightarrow M$	0.795	0.794
9	$A_2 \rightarrow A_2$	0.326	0.307
10	$C_2A \rightarrow C_1B$	0.399	0.397
11	$C_2A \rightarrow M$	0.787	0.785
12	$B_2 \rightarrow K_3B$	0.415	0.298
13	$K_3A \rightarrow A_2$	0.601	0.701
14	$A_2 \rightarrow K_3A$	0.302	0.389
15	$K_3B \rightarrow B_2$	0.729	0.597
16	$K_3B \rightarrow C_1B$	0.731	0.787
17	$K_3B \rightarrow M$	1.138	1.150
18	$K_3B \rightarrow C_1B$	0.820	0.759

For example, process 1, $B_2 \rightarrow B_2$, is a single-atom B-step edge process in which the diffusing atom has 2 nearest-neighbors before and after the process. Process 3, $C_1B \rightarrow B_2$, is a corner rounding process towards a B-step, the diffusing atom starting on the corner of a B-step with one nearest-neighbor and ending up on the B-step with two nearest-neighbors. In process 10, $C_2A \rightarrow C_1B$, the diffusing atom begins on the corner of an A-step having two nearest-neighbors and ends up on the corner of a B-step with only one nearest-neighbor.

5.3 Diffusion Coefficients and Effective Energy Barriers

We start our SLKMC simulations with an empty database. Every time a new configuration (or neighborhood) is turned up, SLKMC-II finds on the fly all possible processes using the drag method, calculates their activation barriers and stores them in the database as the simulation proceeds. Calculation of energetics occurs at each KMC step during initial stages of the simulation when the database is empty or nearly so, and ever less frequently later on. Recall that the types of processes and their activation barriers are dependent on island size, each one of which requires a separate database that cannot be derived from that for islands of other sizes.

We carried out 10^7 KMC steps for each island size at temperatures 300K, 400K, 500K, 600K and 700K. We calculated the diffusion coefficient of an island of a given size using Einstein Equation[92]: $D = \lim_{t\to\infty}\langle R_{CM}(t) - R_{CM}(0)]^2\rangle/2dt$, where $R_{CM}(t)$ is the position of the center of mass of the island at time t, and d is the dimensionality of the system, which in our case is 2.

5.3.1 Ni Islands

For the case of Ni islands on Ni(111), the diffusion coefficients obtained for island sizes $1-10$ at various temperatures are summarized in Table 5.12.

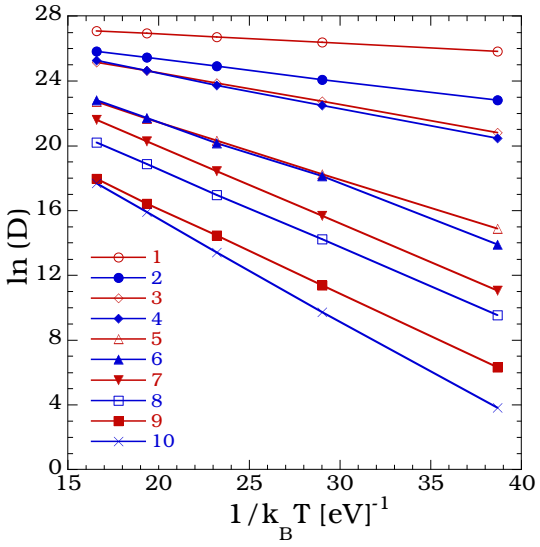

Figure 5.25 Arrhenious plots for 1−10 atom Ni islands.

At 300 K, diffusion coefficients range from 1.63×10^{11} Å^2/s for a monomer to 8.66×10^{01} Å^2/s for a decamer. Effective energy barriers for islands are extracted from their respective Arrhenius plots (Figure 5.25) and also summarized in Table 5.12. Figure 5.26 plots effective energy barrier as a function of island size. It can be seen that the effective energy barrier increases almost linearly with island size. Note that small deviations from linear dependence in Figure 5.26 are interesting. For example, there is small difference in the effective energy barriers for a trimer and a tetramer but then a pronounced increase for a pentamer. Similarly, the heptamer and the octamer have almost the same effective energy barriers.

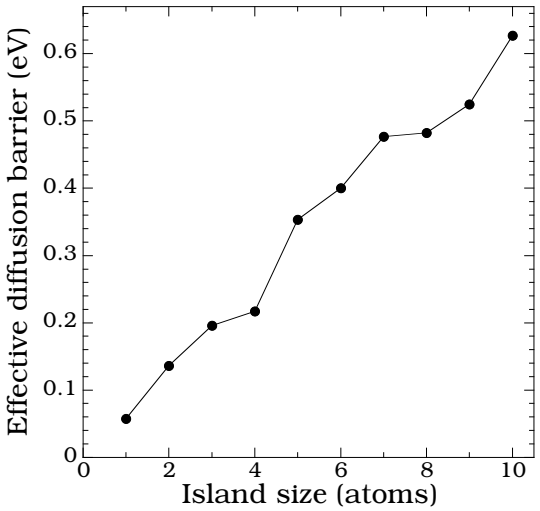

Figure 5.26 Effective energy barriers of 1−10 atom Ni islands as a function of island size.

Table 5.12 Diffusion coefficients ((Å^2/s) at various temperatures, effective energy barriers and effective prefactors for Ni islands.

Size(N)	300K	400K	500K	600K	700K	E_{eff} (eV)	$\nu_{eff}(s^{-1})$
1	1.63×10^{11}	2.85×10^{11}	3.99×10^{11}	5.00×10^{11}	5.87×10^{11}	0.058	7.40×10^{11}
2	8.14×10^{09}	2.88×10^{10}	6.54×10^{10}	1.13×10^{11}	1.64×10^{11}	0.136	7.60×10^{11}
3	1.09×10^{09}	7.42×10^{09}	2.30×10^{10}	5.00×10^{10}	8.23×10^{10}	0.196	1.05×10^{11}
4	7.64×10^{08}	5.83×10^{09}	2.02×10^{10}	4.91×10^{10}	9.93×10^{10}	0.217	15.7×10^{11}
5	2.90×10^{06}	8.42×10^{07}	6.59×10^{08}	2.55×10^{09}	7.36×10^{09}	0.353	11.9×10^{11}
6	1.08×10^{06}	7.39×10^{07}	5.66×10^{08}	2.69×10^{09}	8.12×10^{09}	0.400	31.1×10^{11}
7	6.24×10^{04}	6.40×10^{06}	1.01×10^{08}	6.37×10^{08}	2.37×10^{09}	0.477	21.4×10^{11}
8	1.38×10^{04}	1.50×10^{06}	2.31×10^{07}	1.57×10^{08}	5.91×10^{08}	0.482	8.40×10^{11}
9	5.48×10^{02}	8.77×10^{04}	1.89×10^{06}	1.35×10^{07}	6.23×10^{07}	0.525	1.80×10^{11}
10	8.66×10^{01}	2.25×10^{04}	7.20×10^{05}	7.97×10^{06}	4.95×10^{07}	0.627	7.10×10^{11}

5.3.2 Ag Islands

Table 5.13 reports the diffusion coefficients obtained for island sizes $1-10$ at various temperatures are summarized for Ag islands on Ag(111). At 300 K, diffusion coefficients range from 2.11×10^{11} Å^2/s for a monomer to 2.15×10^{02} Å^2/s for a decamer. Effective energy barriers, extracted from the Arrhenius plots (Figure 5.27) are summarized in Table 5.13. Figure 5.28 plots effective energy barrier as a function of island size. Note that the

effective energy barrier increases almost linearly with island size, with the exception for the island sizes 7, 8 and 9, for which effective energy barrier is almost constant.

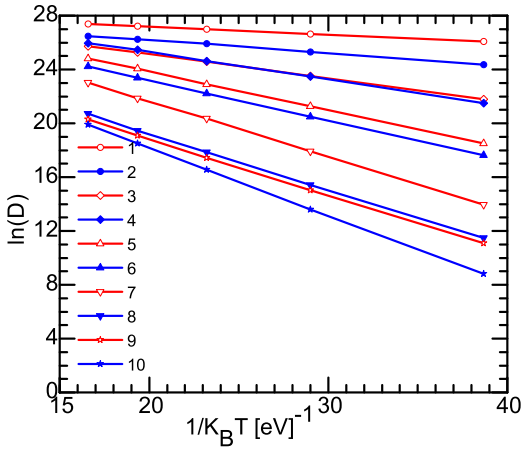

Figure 5.27 Arrhenius plots for 1−10 atom Ag islands.

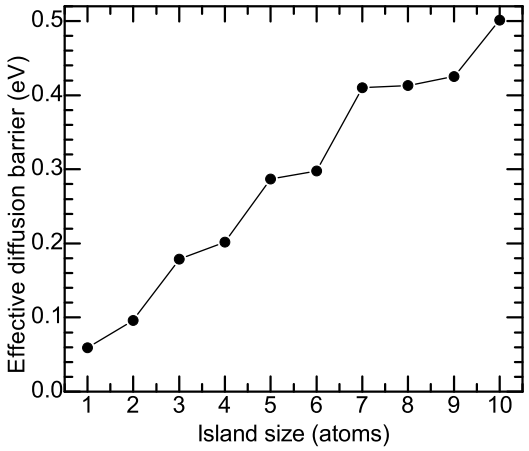

Figure 5.28 Effective energy barriers of 1−10 atom Ag islands as a function of island size.

Table 5.13 Diffusion coefficients (($Å^2$/s) at various temperatures and effective energy barriers for Ag islands.

Island Size	300K	400K	500K	600K	700K	E_{eff} (eV)
1	2.11×10^{11}	3.74×10^{11}	5.27×10^{11}	6.62×10^{11}	7.79×10^{11}	0.059
2	6.33×10^{10}	1.68×10^{11}	2.79×10^{11}	4.13×10^{11}	5.29×10^{11}	0.096
3	2.94×10^{09}	1.62×10^{10}	4.72×10^{10}	9.51×10^{10}	1.49×10^{11}	0.179
4	2.20×10^{09}	1.57×10^{10}	4.88×10^{10}	1.14×10^{11}	1.86×10^{11}	0.202
5	1.08×10^{08}	1.72×10^{09}	8.73×10^{09}	2.83×10^{10}	6.01×10^{10}	0.287
6	4.50×10^{07}	7.87×10^{08}	4.36×10^{09}	1.45×10^{10}	3.29×10^{10}	0.298
7	1.14×10^{06}	6.14×10^{07}	6.90×10^{08}	3.07×10^{09}	1.01×10^{10}	0.410
8	9.55×10^{04}	4.99×10^{06}	5.64×10^{07}	2.81×10^{08}	1.00×10^{09}	0.413
9	3.48×10^{04}	2.07×10^{06}	2.51×10^{07}	1.90×10^{08}	7.12×10^{08}	0.425
10	2.15×10^{02}	7.49×10^{04}	2.51×10^{06}	2.57×10^{07}	1.29×10^{08}	0.501

5.3.3 Cu Islands

Different than Ni and Ag, Cu islands on Cu(111) have higher diffusion coefficients and lower effective energy barriers for island sizes $1-10$ at various temperatures, as summarized in Table 5.14.

At 300 K, diffusion coefficients range from 5.66×10^{11} $Å^2$/s for a monomer to 1.21×10^{05} $Å^2$/s for a decamer (values in brackets are from Ref [1]). Effective energy barriers for islands are extracted from their respective Arrhenius plots (Figure 5.29) and also summarized in Table 5.14. Figure 5.30 plots effective energy barrier as a function of island size. Figure 5.30 also shown the effective energy barrier data from [1]. It can be seen that the effective energy barrier increases almost linearly with island size. It can be seen from Figure 5.30 that effective energy barriers obtained from [1] are higher that results obtained from our simulations. This difference arises mainly because in [1], fcc to hcp concerted processes were included in an approximate way, where as in SLKMC-II [19], all these processes and their energy barriers are treated exactly.

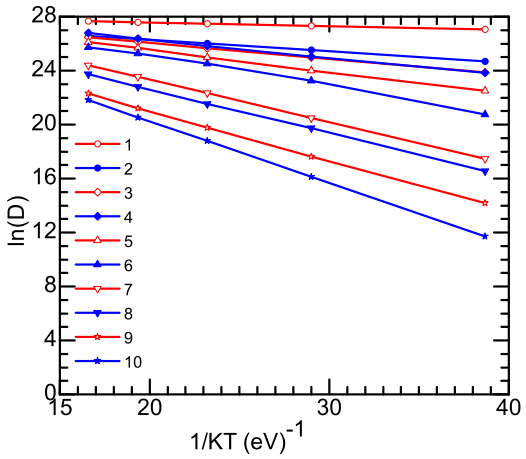

Figure 5.29 Arrhenius plots for 1−10 atom Cu islands.

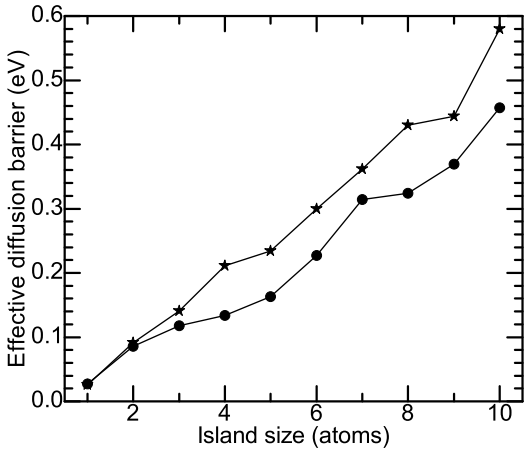

Figure 5.30 Effective energy barriers of 1−10 atom Cu islands as a function of island size. a) Filled circles represents results from our simulations using SLKMC-II. b) Filled stars represents results from [1].

Note that in this work, for all three systems, we have assumed the same diffusion prefactor for all processes. Some changes in the calculated energy barriers are also to be expected when more accurate methods (based on *ab initio* electronic structure calculations)

are employed. We leave a more sophisticated analysis of the island size dependence on the effective energy barriers for the future.

Table 5.14 Diffusion coefficients (($\AA^2$/s) at various temperatures and effective energy barriers for Cu islands.

Island Size	300K	400K	500K	600K	700K	E_{eff} (eV)
1	5.66×10^{11}	7.37×10^{11}	8.63×10^{11}	9.59×10^{11}	1.03×10^{12}	0.027
	(5.70×10^{11})	–	(8.50×10^{11})	–	(1.02×10^{12})	(0.026)
2	5.18×10^{10}	1.23×10^{11}	2.02×10^{11}	2.72×10^{11}	3.44×10^{11}	0.086
	(1.68×10^{11})	–	(6.90×10^{11})	–	(1.24×10^{12})	(0.091)
3	2.32×10^{10}	7.12×10^{10}	1.40×10^{11}	2.29×10^{11}	3.17×10^{11}	0.118
	(4.89×10^{10})	-	(3.27×10^{11})	-	(1.22×10^{12})	(0.141)
4	2.24×10^{10}	7.43×10^{10}	1.64×10^{11}	2.80×10^{11}	4.36×10^{11}	0.134
	(4.19×10^{09})	-	(1.06×10^{11})	-	(4.60×10^{11})	(0.211)
5	5.90×10^{09}	2.66×10^{10}	6.92×10^{10}	1.42×10^{11}	2.23×10^{11}	0.163
	(7.81×10^{08})	-	(2.87×10^{10})	-	(1.40×10^{11})	(0.234)
6	1.01×10^{09}	1.25×10^{10}	4.47×10^{10}	9.36×10^{10}	1.50×10^{11}	0.227
	(7.57×10^{07})	-	(8.15×10^{09})	-	(5.60×10^{10})	(0.300)
7	3.87×10^{07}	8.00×10^{08}	5.01×10^{09}	1.69×10^{10}	3.88×10^{10}	0.314
	(2.40×10^{07})	-	(5.80×10^{09})	-	(7.60×10^{10})	(0.360)
8	1.54×10^{07}	3.68×10^{08}	2.23×10^{09}	8.01×10^{09}	2.03×10^{10}	0.324
	(2.10×10^{06})	-	(1.65×10^{09})	-	(2.59×10^{10})	(0.430)
9	1.38×10^{06}	4.36×10^{07}	3.86×10^{08}	1.66×10^{09}	4.77×10^{09}	0.369
	(7.72×10^{04})	-	(7.20×10^{07})	-	(1.45×10^{09})	(0.444)
10	1.21×10^{05}	1.01×10^{07}	1.47×10^{08}	8.28×10^{08}	2.96×10^{09}	0.457
	(1.65×10^{03})	-	(1.37×10^{07})	-	(7.02×10^{08})	(0.580)

5.4 Further Discussion and Conclusions

To summarize: we have performed a systematic study of the diffusion of small islands (1-10 atoms) on fcc(111) for Ni, Ag and Cu, using a self-learning KMC method with a newly-developed pattern recognition scheme (SLKMC-II) in which the system is allowed to evolve through mechanisms of its choice on the basis of a self-generated database of single-atom, multiple-atom and concerted diffusion processes (each with its particular activation barrier) involving fcc-fcc, fcc-hcp and hcp-hcp jumps. We find that concerted diffusion processes contribute the most to the displacement of the center of mass (i.e., to island diffusion),

while single-atom processes contribute the least. As for multi-atom processes (reptation or shearing): while these produce more displacement than the latter, they are hardly ever selected. Though the energy barriers for reptation processes are small compared to those for concerted diffusion processes, reptation occurs only when an island is transformed into a non-compact shape, as happens only rarely in the temperature range to which our study is confined. In contrast, though shearing occurs with close-to-compact shapes (which appear more frequently than do non-compact shapes, but with islands of certain sizes), the barriers for these processes are higher than those for reptation.

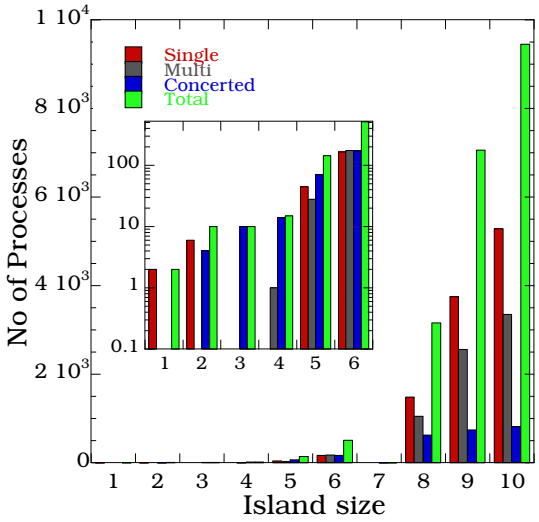

Figure 5.31 Distribution of single-atom, multi-atom, concerted and total processes for 1-10 atom islands (Ni islands) accumulated in the database during SLKMC simulations. Inset shows the log-linear plot for up to the 6-atom island.

Finally, although for all island sizes for the three systems studied here, island diffusion is primarily dominated by concerted diffusion processes, the frequency of occurrence of both

single-atom and multi-atom processes does increase with increase in island size, owing to increase in the activation barrier for concerted diffusion processes with island size.

Figure 5.31, Figure 5.32 and Figure 5.33 shows the number of each type of diffusion process (single-, multi-atom and concerted) collected during our SLKMC-II simulations for each island size (1-10), together with the total number of processes of all types for each island size. (For the sake of clarity, the insert (in case of Figure 5.31) shows a log-linear plot of these quantities for island sizes 1-6). It can be seen that the number of processes accumulated increases with island size, and significantly so beyond the tetramer. It can also be seen from Figure 5.31 that the overall increase in number of processes with island size is constituted predominantly by significant increases in single-atom processes and (to a lesser degree) multi-atom processes. Meanwhile the number of concerted processes accumulated in the database increases at a much slower pace with island size.

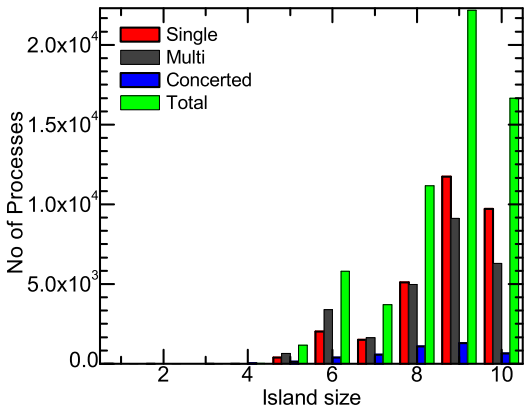

Figure 5.32 Distribution of single-atom, multi-atom, concerted and total processes for 1-10 atom islands (Ag islands) accumulated in the database during SLKMC simulations.

This significant increase in single-atom processes is mainly due to the use of 10 rings to identify the neighborhood of an atom. Use of 10 rings corresponds to inclusion of 5 nearest-neighbor fcc-fcc or hcp-hcp interactions. Elsewhere we show that 6 rings (which corresponds to 3 nearest-neighbor interactions) offer a range of interaction sufficient for accurately calculating the activation barriers for single-atom processes [51]. But it is essential to include the long-range interaction (and hence 10 rings) if one aims to accurately take into account multi-atom and concerted processes, the latter of which predominate in small-island diffusion. This significant increase in the number of processes with island size also justifies resorting to an automatic way of finding all the possible processes during simulations instead of using a fixed (and thus necessarily preconceived) list of events.

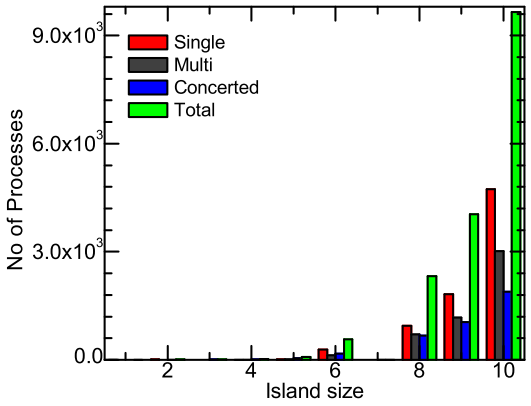

Figure 5.33 Distribution of single-atom, multi-atom, concerted and total processes for 1-10 atom islands (Cu islands) accumulated in the database during SLKMC simulations.

As mentioned earlier, with increasing island size not only does the number of accumulated single-atom processes and multi-atom processes increase but also their frequency of occurrence. Still island diffusion is primarily due to concerted diffusion processes, since it is

these that produce largest displacement of center of mass. This can be easily observed by comparing, for each island size, the effective diffusion barriers given in Table 5.12 with the activation barriers in the tables given in Sect. 7.3 for concerted diffusion processes: effective diffusion barriers more or less closely follow activation barriers for concerted diffusion processes – except for the 9-atom island, in which the contribution of single-atom processes to the island's diffusion is significantly larger than for other island sizes. Similar conclusions hold for the case of Ag and Cu islands.

In conclusion, self-diffusion of small-islands in the case of Ni, Ag and Cu on fcc(111), diffusion proceeds via concerted processes, even though the frequency of their occurrence decreases with increase in island size.

CHAPTER 6
ADSORBATES ON BIMETALLIC NANOSTRUCTURES: INSIGHTS FROM DFT CALCULATIONS

6.1 Introduction

High reactivity of nanoparticles in general and Au nanoparticles in particular, in contrast to gold bulk, towards various reactions [93] can be explained on the basis of various factors including, their size, support and geometry [94, 95]. Similarly, bimetallic systems have been reported to exhibit activity different from that of pure metals. This ability of the impurity metal to promote the desired catalytic activity and selectivity have been subject of many studies [96–99]. Much interest in basic understanding of the chemical activity on bimetallic surfaces is to develop catalysts with properties that can be tuned by changing compositions. Various reactions can be promoted by bimetallic clusters due to the electronic effects associated with the formation of new metal-metal bonds which alter surface chemical properties, such as adsorbate adsorption strength etc [99]. As a step towards understanding some of the electronic structure changes brought about by the elemental constituents in bimetallic nanostructures, we have carried out DFT calculations of Ni-Au and Pt-Au systems. We are particularly interested in the effect of adsorbates (CO for Ni-Au and CH_3O for Pt-Au system) with specific questions in mind which have been motivated by the experiments in the Chen's group.

Low Energy Ion Scattering (LEIS) studies of Ni-Au bimetallic clusters on $TiO_2(110)$ surface suggests [15] that the bimetallic clusters form a core shell structure with Au as shell and Ni staying in the interior sites. It has been observed that at room temperature CO does not adsorb on $TiO_2(110)$ or pure Au clusters whereas the molecular desorption of CO from the 0.25 ML Ni clusters on $TiO_2(110)$ occurs at 400K. As the fraction of Au in the 0.25 ML Ni clusters is increased (resulting Ni-Au clusters are core shell with Au on the surface), the intensity of molecular desorption peak from the Ni-Au clusters decreases. However a significant amount of CO desorbed from the Ni-Au clusters with Au fractions of >50 % suggesting that these clusters have Ni atoms at the surface of the Ni-Au clusters. Given the fact that Ni-Au clusters are core shell structures, it was proposed that presence of CO might have influence the electronic structure of the bimetallic cluster in such a way that Ni migrates to the surface.

In another experiment of the reaction of methanol on Pt-Au bimetallic clusters (with 100% Au atoms on the surface of bimetallic cluster) on $TiO_2(110)$, it was observed that methanol reaction on pure Pt clusters produces CO and H_2 as the major products, while reaction on pure Au clusters yields formaldehyde as the main product rather than CO. However, for the bimetallic clusters, the pure Au surface modified by Pt in the bulk exhibit activity for methanol decomposition that is almost identical to that of pure Pt, which is surprising.

Below we present some results of our DFT calculations will help answer some of the questions raised in the above experiments.

6.2 Computational Details

Scalar relativistic density functional theory (DFT)[21] calculations were carried out with the VASP code [85, 86] using the generalized gradient approximation with the Perdew-Burke-Ernzerhof (PBE) functional [88] to describe the exchange-correlation effects. The plane-wave pseudo potential method implemented in the VASP package with the projected-augmented-wave (PAW) pseudo potentials [86, 87] was used to describe the electron-ion interaction. The kinetic energy cutoff for the plane-wave expansion was set to 350 eV (for Ni-Au case) and 450 eV (for Pt-Au case), and the conjugate-gradient algorithm was used to relax the structure by requiring all force components acting on each ion to be less than 0.01 eV/A. The Brillouin zone was sampled with one Γ-point using a non-shifted 1 x 1 x 1 Monkhorst Pack k-point mesh.

Similarly for the case of Ni-Au nanocluster, *ab initio* molecular dynamics (MD) simulations were also carried out for 13-atom clusters using the VASP code and PAW-PBE potentials with energy cut offs of 700 eV for carbon and oxygen, 270 eV for Ni, and 230 eV for Au; the cell size was 20 x 20 x 20 $\mathring{A}^3$, allowing 13.14 - 16.40 Åof vacuum between clusters in the imposed periodic boundary conditions. Two cube-octahedral structures for

$Au_{12}Ni$ (one with Ni at the center and the other with Ni at the surface) were optimized so that the forces on each atom were less than 2 x 10^{-3} eV/Å. The interaction of CO and the lower energy isomer, which was the one with Ni at the center, was then studied to examine the effect of CO on migration of Ni from the core to the surface. For all simulations, the time step was 3 fs, and the system was allowed to evolve over 366 steps (1 ps).

For the case of Pt-Au system, slab calculations were done using a slab size of 5x5x4 layers and for 13 atoms and 52 atoms nano-cluster studies, we used super cell of 18x18x18 $\mathring{A}^3$ and of 25x25x25 $\mathring{A}^3$ with and without adsorbates. We relax all surface structures, using the conjugate-gradient algorithm [89], until all force components acting on each atom are smaller than 0.02 eV/Å. To get spin-polarized energies, we did have performed one self-consistent calculation for the relaxed structures. In calculating reaction barriers and searching transition states, we first use the Nudged Elastic Band (NEB) method [31] for preliminarily determining a minimum energy path, then apply a Climbing Image Nudged Elastic Band (CI-NEB) [32] calculation. This way of doing NEB and CI-NEB calculations is found to be more efficient for searching transition states than performing CI-NEB alone. Here in, we use the term "(CI-)NEB" to refer a combination of NEB and CI-NEB calculations. In all NEB calculations, we used 7 images in each case. Results for the reaction energetics are all from non-spin polarized calculations.

6.3 Effect of CO on Ni-Au nanoclusters

In order to distinguish whether the proposed Ni migration is due to the presence of CO molecule or factors such as temperature induced mobility, we have performed a DFT study of the Ni-Au clusters, including the case of CO-conjugated particles.

6.3.1 Results of Total Energy Calculations

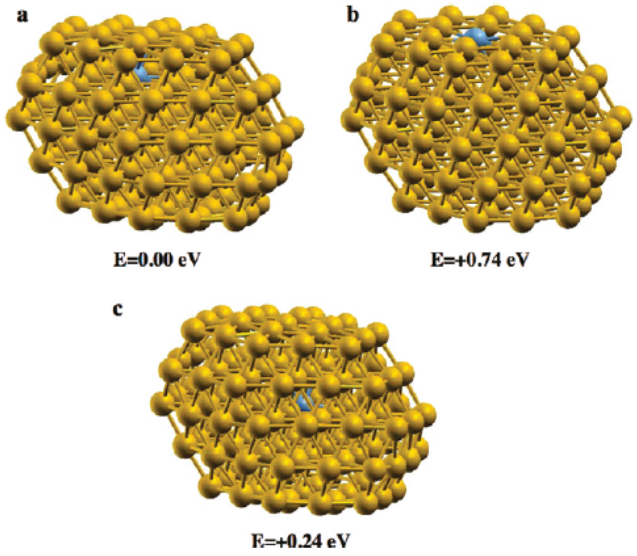

Figure 6.1 Optimized structures for the unsupported Ni_1Au_{121} clusters with the Ni atom in the (a) second layer, (b) first layer, and (c) third layer. Relative energies calculated by density functional theory are given below each cluster. Au atoms are shown in yellow and Ni in blue.

In our analysis, the DFT calculations were carried out on unsupported 122-atom clusters with varying Ni-Au compositions. In the first case the structure of Ni_1Au_{121} clusters is determined by optimizing the fcc structure for a pure Au_{122} cluster terminated by (111)

facets, incorporating a single Ni atom, and then reoptimizing the structure of the resulting bimetallic cluster. The lowest energy structure is the one in which the Ni atom resides in the second layer from the surface (Figure 6.1(a) & Table 6.1), whereas the cluster with the Ni atom at the surface (Figure 6.1(b) & Table 6.1) is 0.74 eV higher in energy. This result is consistent with the greater surface free energy of Ni compared to Au, causing Ni to prefer the interior sites in the cluster. Furthermore, incorporation of the Ni atom into the third layer (Figure 6.1(c) & Table 6.1) results in a structure with an energy 0.24 eV higher than that of the cluster with Ni in the second layer. It has been suggested by DFT calculations that Ni can donate charge to Au in small (3-8 atom) Ni-Au clusters [100]. Thus, the Ni atom may prefer to occupy the second layer from the surface because charge transfer can be maximized when the nearest Au atoms are at the surface, where the atoms can accommodate greater charge due to their lower coordination number.

Table 6.1 Total energy difference (in eV) for various configurations of AuNi-CO nanoclusters, with (column 2) and without CO (column 1).

Position of Ni atom	ΔE	ΔE
In top layer	0.74	0.0
In first layer	0.0	1.260
In second layer	0.24	1.263

Ni atoms also prefer to occupy the subsurface sites for higher Ni concentrations in Ni_2Au_{120} and $Ni_{38}Au_{84}$ clusters. Calculations for the Ni_2Au_{120} clusters suggest that there is no strong tendency for Ni atoms to aggregate within the interior of the cluster. The structure in which the two Ni atoms are in the nearest neighbor positions in the same layer is 0.003

eV lower in energy than when the atoms are in the second nearest neighbor positions in the same layer, and 0.072 eV lower in energy than when the Ni atoms are in adjacent layers. For a relaxed $Ni_{38}Au_{84}$ cluster, all of the Ni atoms are found in the interior of the cluster; note that the $Ni_{38}Au_{84}$ clusters correspond to the maximum number of Ni atoms in which the surface layer for the clusters can still consist only of Au atoms. For both the Ni_2Au_{120} and $Ni_{38}Au_{84}$ clusters, the energy required to bring one Ni atom to the surface of the cluster is approximately 0.7 eV.

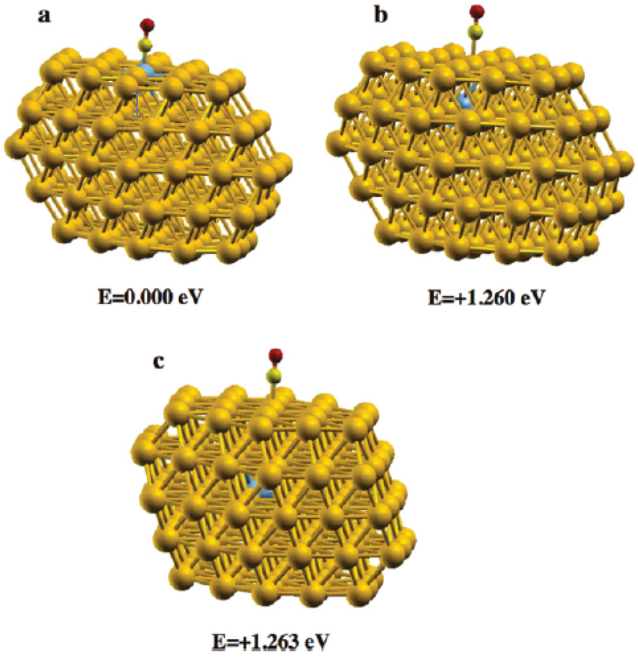

Figure 6.2 Optimized structures of the unsupported Ni_1Au_{121} clusters with a CO molecule adsorbed on the surface and Ni in the (a) first layer, bound to CO, (b) second layer, (c) third layer. Relative energies calculated by density functional theory are given below each cluster. Au atoms are shown in yellow and Ni in blue.

In contrast, when a single CO molecule is adsorbed on the surface of the Ni_1Au_{121} cluster, the lowest energy configuration is the one in which the Ni atom is at the cluster surface and binds to the CO molecule (Figure 6.2 & Table 6.1). When the Ni atom is in the second or third layer with CO bound to surface Au atoms, the energy of the system is $\sim$ 1.26 eV higher. Therefore, it is thermodynamically favorable for Ni to reside at the surface in the presence of CO in order to form the strong Ni-CO bond.

6.3.2 Results of Molecular Dynamics Simulations

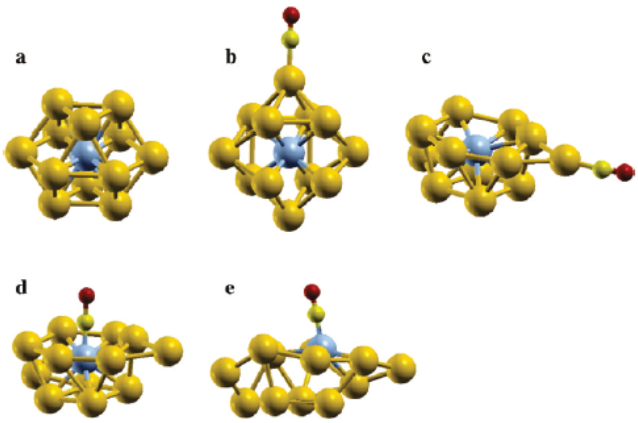

Figure 6.3 Optimized structures for the unsupported Ni_1Au_{12} clusters used in molecular dynamics (MD) simulations: (a) the initial structure without CO; (b) the initial structure with one CO molecule bound to a surface Au atom; (c) the final structure at 300 K after 366 steps (3 fs/step) in the MD simulation; (d) the initial structure from (c) with CO bound to the Ni atom instead of a Au atom; (d) the final structure at 300 K after 366 steps (3 fs/step) in the MD simulation. Au atoms are shown in dark yellow, Ni atoms in blue, carbon atoms in light yellow, and oxygen atoms in red.

Given that it is energetically favorable for Ni to exist at the surface of the bimetallic clusters in the presence of CO, it is also important to understand the kinetics of Ni diffusion

to the surface of the bimetallic clusters. To address this issue, *ab initio* molecular dynamics simulations were carried out on unsupported Ni_1Au_{12} clusters. Although the lowest energy configuration for Ni_1Au_{12} is a flat structure, simulations were carried out on the next lowest energy structure shown in Figure 6.3 (a) in order to model the behavior of three dimensional clusters. In the relaxed Ni_1Au_{12} structure, the Ni atom is initially situated in the interior of the cluster. MD simulations at 300 K show rearrangement of atoms in the cluster upon substitution of the Ni atom, but no diffusion events are recorded. Simulations at higher temperatures demonstrate that the cluster dissociates at 1000 K before revealing any Ni migration to the surface.

In the presence of a single CO molecule, the MD simulations illustrate that the Ni_1Au_{12} cluster undergoes significant restructuring. Figure 6.3 (b) shows a CO molecule bound to a Au surface atom in the relaxed Ni_1Au_{12} structure. Over the course of the MD simulation at 300 K, restructuring of the cluster brings Ni to the cluster surface (Figure 6.3 (c)), and CO eventually desorbs from Au at longer times. Furthermore, if CO is then adsorbed on the Ni atom at the surface of the resulting structure (Figure 6.3 (d)), the Ni atom remains at the surface after the MD simulation at 300 K (Figure 6.3 (e)). The results of these simulations indicate that migration of Ni to the cluster surface is possible even at room temperature, with the strong Ni-CO bonding as the driving force for the cluster restructuring. In the absence of CO, there is no such driving force for Ni migration to the cluster surface, and even at high temperatures (1000 K) Ni diffusion to the surface does not

occur. Therefore, the presence of CO must induce diffusion of Ni to the cluster surface, and the Ni atoms are then trapped at the surface by the formation of strong Ni-CO bonds.

6.3.3 Charge Transfer Analysis

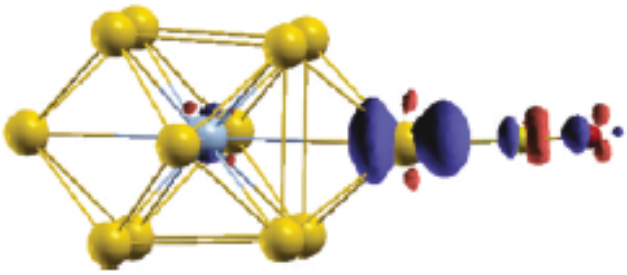

Figure 6.4 Density functional theory results for the change in the electron charge density in the Ni_1Au_{12} system after CO adsorption onto a surface Au atom. The blue and red regions indicate the extra and the missing charge density, respectively. Au atoms are shown in yellow (larger balls), Ni atoms in blue, carbon atoms in light yellow (smaller balls), and oxygen atoms in pink.

An electron charge-transfer mechanism might contribute to CO-induced Ni atom diffusion presented above. Because both Ni [100] and CO [101] donate charge when bound to Au, when CO approaches the gold atom its donor charge will try *to push out* the charge donated by the Ni atom, which may lead to reduction of the Ni-Au bond strength and increase the probability for Ni atom migration. A Ni atom at the surface is more stable because of the strong Ni-CO bond, and the Ni atom donates charge to the CO molecule, contrary to the Au-CO case [102]. DFT calculations have been carried out on the Au_{12}Ni-CO clusters used in the MD simulations in order to investigate these possibilities. One significant

change in the system after CO adsorption is substantial charge redistribution (Figure 6.4). Charge flow from the CO molecule causes the charge on the bimetallic cluster to increase by 0.17 electrons, and most of this charge ($\sim$ 0.1 electrons) accumulates on the Au atom interacting with CO. A second more striking result is a dramatic increase in Ni-Au bond length from 2.66 $\mathring{A}$ to 3.34 $\mathring{A}$ after the CO molecule is adsorbed on the Au atom. This change is also accompanied by an increase in the C-O bond length from 1.135 $\mathring{A}$ to 1.146 $\mathring{A}$. Thus, a possible mechanism for CO-induced diffusion of Ni may involve both charge transfer and an increase in Ni-Au bond length. When CO approaches a Au atom, the charge donated by the CO may weaken metal-metal bonding between the Au atom and a nearest neighbor Ni atom, increasing the probability for Ni diffusion. The slight preference observed in DFT calculations for Ni to occupy the first subsurface layer rather than deeper layers facilitates CO-induced diffusion of the Ni atoms to the surface. Furthermore, an increase of the Au-Ni bond length may lead to an instability of the Ni atoms that stimulates their migration to the surface.

6.4 CH_3O Adsorption on Bimetallic Au, Pt and Pt-Au Surfaces

In experiments on methanol reaction it is already known that in the case of TiO_2 supported Au clusters, H bond is easily broken at the interfacial sites [103]. It is the product methoxy (CH_3O) whose characteristics on the bimetallic Pt-Au nanoclusters is the subject

of investigation. As mentioned earlier, the experimental data from the Chen group suggest the presence of Pt in the surface layer of the Pt-Au nanocluster on titania, in the presence of methoxy. We have carried out DFT calculations for the methoxy-Pt-Au system, along the lines discussed in chapter 6.3, to find that methoxy does induce the diffusion of Pt atom to the surface from the interior. To get further insights we have carried out DFT calculations of methoxy chemisorbed on Au5x5x4(111), Pt5x5x4(111), single layer of Au on Pt(111) (hereafter represented by AuPtPtPt(111)) and on a Pt atom exchanged with a Au atom (hereafter represented by Au(Pt1)Pt(Au1)PtPt(111)) in the second layer.

6.4.1 Results of Total Energy Calculations

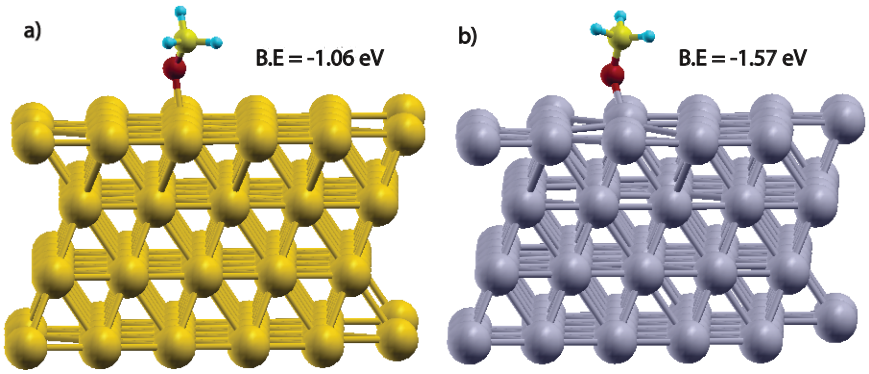

Figure 6.5 Optimized structures of (a) Au(111) and (b) Pt(111) surface. CH_3O is adorbed on-top site for both cases. Au atoms are shown in yellow, Oxygen in red, Carbon in light yellow and H in blue

DFT calculations for the binding energy of methoxy on 4-layer slabs with a 5x5x4 unit cell for pure Pt, pure Au and a single Au layer on a 3-layer Pt slab (Au-Pt-Pt-Pt) are shown in Figure 6.5 & Figure 6.6.

Table 6.2 Binding energy of Methoxy (in eV) on Au5x5x4(111), Pt5x5x4(111), AuPtPtPt(111) and Au(Pt1)Pt(Au1)PtPt(111) slabs.

System	B.E
Au5x5x4(111)	-1.06
Pt5x5x4(111)	-1.57
AuPtPtPt(111)	-0.90
Au(Pt1)Pt(Au1)PtPt(111)	-1.44

We find that methoxy binds more strongly on a pure Pt slab (-1.57 eV) than on a pure Au slab (-1.06 eV), which is consistent with the expected stronger adsorption to Pt compared to Au (see Figure 6.5(a) & (b) & Table 6.2) [104]. For the AuPtPtPt(111) surface, the methoxy binding energy is -0.90 eV, whereas for the case when one Pt atom from the third layer is switched with a Au layer (Figure 6.6(a) & (b)) shows that methoxy binding to this Pt atom in the environment of Au atoms is -1.44 eV which is lower than the case of pure Pt(111) slab. Total energy calculations for AuPtPtPt(111) and Au(Pt1)Pt(Au1)PtPt(111) (see Table 6.3) show that Au(Pt1)Pt(Au1)PtPt(111) is 0.40 eV less stable than AuPtPtPt(111), suggesting that Pt prefer to stay in the sub-surface sites. However, when a single CH_3O molecule is adsorbed on Pt atom in Au(Pt1)Pt(Au1)PtPt(111), it is 0.420 eV more stable than CH_3O adsorbed on Au atom in AuPtPtPt(111) as shown in Table 6.3. Therefor it is thermodynamically more favorable for Pt atom to be in the surface Au layer (Au(Pt1)Pt(Au1)PtPt(111)) to bind to CH_3O.

Table 6.3 Total energy difference (in eV) for the AuPtPtPt(111) and Au(Pt1)Pt(Au1)PtPt(111) systems, without (column 1) and with CH_3O (column 2).

Position of Ni atom	ΔE	ΔE
AuPtPtPt(111)	0.0	0.0
Au(Pt1)Pt(Au1)PtPt(111)	0.40	-0.42

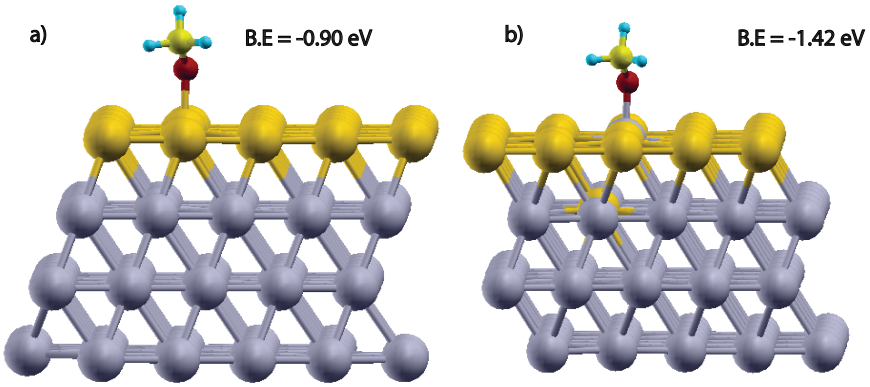

Figure 6.6 Optimized structures of (a) AuPtPtPt(111) and (b) Au(Pt1)-Pt-Pt-Pt-Pt(111) surface. CH_3O is adsorbed on-top site for both cases. Au atoms are shown in yellow, Oxygen in red, Carbon in light yellow and H in blue

Thus, there is a thermodynamic driving force that cause Pt to migrate to the surface in order to make system more stable, which is consistent to what is observed for CO-induced migration of Pt to the surface of Pt-Au clusters.

6.4.2 CH_3O Decomposition on $Au_{12}Pt_1$ Cluster

We have also investigated the CH_3O dissociation to CO and various intermediates along with their geometries, bond lengths and reaction barriers on unsupported $Au_{12}Pt_1$ nanocluster. Figure 6.7 show the adsorption geometry of CH_3O on pure Au_{13} cluster. On

pure Au_{13} cluster, methoxy binds to the Au-top site with O-Au bond length of 2.02 $\mathring{A}$, bond angle $\angle(AuOC) = 118.05°$ and binding energy of E_b = -1.367 eV.

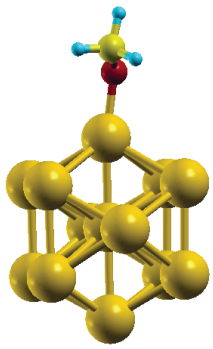

Figure 6.7 Adsorption geometry of CH_3O on Au_{13} cluster. Au atoms are shown in yellow, Oxygen in red, Carbon in light yellow and H in blue.

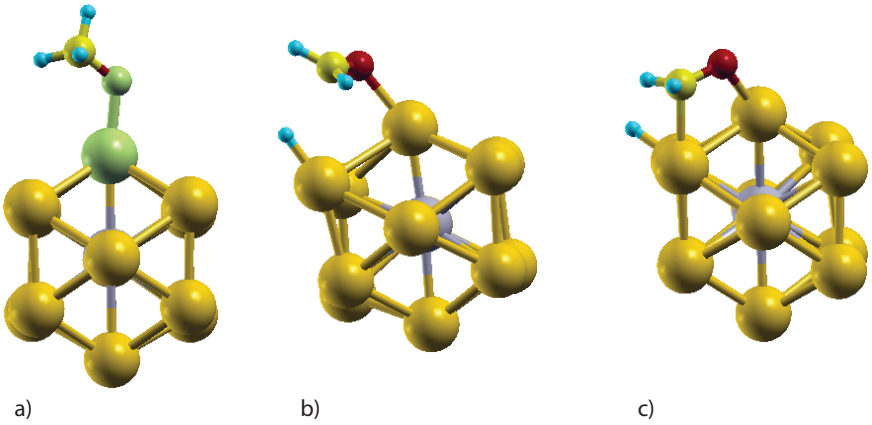

Figure 6.8 (a) Initial, (b) Transition and (c) Final states for $CH_3O \Rightarrow CH_2O + H$ reaction. Au atoms are shown in yellow, Oxygen in red, Carbon in light yellow and H in blue.(See text for details)

Methoxy on $Au_{12}Pt_1$ cluster binds through O atom with a binding energy of E_b = -2.38 eV, O-Au bond length is 2.02 $\mathring{A}$ and $\angle(AuOC) = 119.44°$. Figure 6.8(a) shows the geometry of the initial state of the CH_3O dehydrogenation reaction. At transition state, first one C-H bond is broken and dissociated H atom makes bond with neighboring Au atom as shown in Figure 6.8(b). At transition state, Au-H bond length is 2.20 $\mathring{A}$, whereas O-Au bond length is 2.19 $\mathring{A}$. Finally, in the final state, H-atom diffuses to the neighboring Au atom and bond length between O-Au and C-Au of the resulting formaldehyde is 2.15 $\mathring{A}$ and 2.25 $\mathring{A}$ as shown in Figure 6.8(c). This reaction is slightly endothermic (0.014 eV) and energy barrier for this reaction is 0.38 eV (reverse barrier is 0.366 eV).

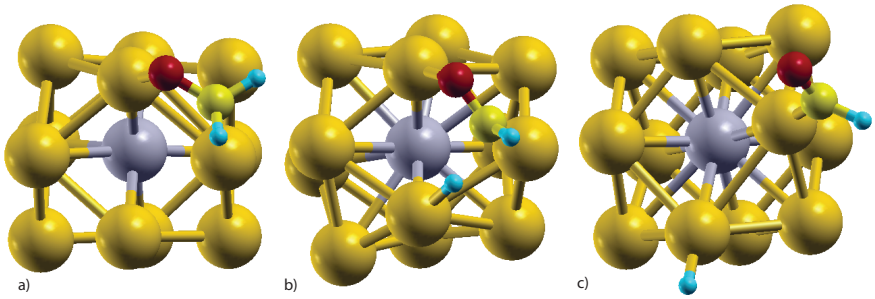

Figure 6.9 (a) Initial, (b) Transition and (c) Final states for $CH_2O \Rightarrow CHO + H$ reaction. Au atoms are shown in yellow, Oxygen in red, Carbon in light yellow and H in blue.(See text for details)

The next step in CH_3O dehydrogenation is stripping of the second H atom from CH_2O to form CHO and H. Binding energy for CH_2O bonded to Au atom on $Au_{12}Pt_1$ cluster is -0.454 eV. This reaction is an exothermic reaction by -0.584 eV. Initial, transition and final states of this reaction are shown in Figure 6.9(a-c). CH_2O adsorbs on the Au atom in

$Au_{12}Pt_1$ with O-Au bond length of 2.14 $\mathring{A}$ and C-Au bond length of 2.23 $\mathring{A}$. At transition state, bond of one hydrogen atom from CH_2O is broken and it forms bond to the neighboring Au atom, with Au-O and C-Au bond lengths of 2.38 $\mathring{A}$ and 2.08 $\mathring{A}$ respectively. In the final state, CHO rotates by breaking O bond from Au atom and finally adjusting in the vertically up form as shown in Figure 6.9(c). CHO binds through C atom to the Au cluster with C-Au bond length of 2.03 $\mathring{A}$ as shown in Figure 6.9(c). Energy barrier for this process is 0.591 eV, with a reverse barrier of 1.175 eV.

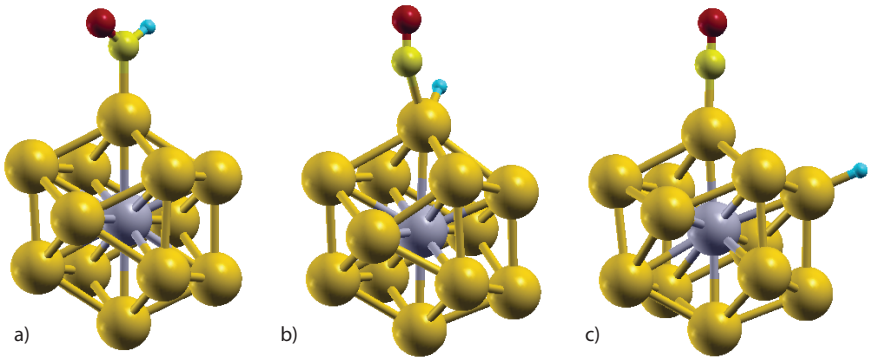

Figure 6.10 (a) Initial, (b) Transition and (c) Final states for CHO ⇒ CO + H reaction. Au atoms are shown in yellow, Oxygen in red, Carbon in light yellow and H in blue.(See text for details)

Final step in CH_3O dehydrogenation is the removal of last Hydrogen atom from CHO to form CO and H. CHO binds to Au atom through C atom of CHO. It has strongest adsorption energy of -3.267 among all intermediates of CH_3O, with C-Au bond length of 2.04 $\mathring{A}$. In this case, reaction center is the Au atom where CHO is adsorbed. First H bond breaks and H atom adsorbs on the same Au atom where resulting CO is adsorbed (see

transition state in Figure 6.10(b)). Next this hydrogen atom diffuses to the neighboring Au atom in the final state as shown in Figure 6.10(d), resulting CO molecule is co-adsorbed on Au atom with C-Au bond length of 1.92 $\mathring{A}$. Energy barrier for this reaction is 1.29 eV and reverse barrier is 1.393 with reaction being exothermic by 0.103 eV. This reaction is the only reaction with highest barrier of 1.29 eV among all dehydrogenation steps of CH_3O dissociation towards CO formation.

CHAPTER 7
A COMBINED DFT+KMC STUDY OF SELECTIVE OXIDATION OF NH_3 ON RUTILE RUO_2(110) SURFACE AT AMBIENT PRESSURE

We have carried out combined density functional theory (DFT) and kinetic Monte Carlo (KMC) simulations for ammonia oxidation on RuO_2(110) at ambient pressure. We have used a database of 25 reaction processes (36 processes if reverse process is separately counted), and find N_2 as the major product instead of NO under ambient conditions in contrast to UHV, thus confirming the presence of pressure gap in ammonia oxidation on RuO_2(110).

7.1 Introduction

Catalytic ammonia oxidation via Ostwald process is an industrially important reaction in order to produce nitric acid, which is largely used for production of fertilizers and is itself an important inorganic intermediate for synthesis of other chemical products such as explosives [105]. Platinum-Rhodium (with 5 - 10% Rh content) is used as a catalyst for catalytic ammonia oxidation at temperature range of 1070 - 1220 K in high pressure. The high cost of Pt-Rh catalyst and frequent replacement of the catalyst (every 3 - 6 month depending on operating pressure) are the major drawbacks. On the other hand, RuO_2 is known as an

excellent oxidation catalyst (A detailed review on the recent development of research and application of RuO_2 is available [106]). Rather recently, $RuO_2(110)$ was shown in experiments undertaken in UHV conditions to be an excellent catalyst for ammonia oxidation so much so that its NO selectivity was found to be as high as that of Pt-Rh catalysts at a much lower temperature of 530 K[17]. Since then, RuO_2 has attracted a considerable interest as a possible substitute for the expensive platinum-based catalysts used in industry [17]. A recent ambient-pressure experiment [16] on polycrystalline rutile RuO_2 samples, however, showed a surprisingly result that N_2 rather than NO, is the dominant product with selectivity of about 80%, suggesting that there is a pressure and also possible a material gap- active RuO_2 phase or facet other than (110) - in ammonia oxidation on RuO_2 [16]. In our previous DFT +

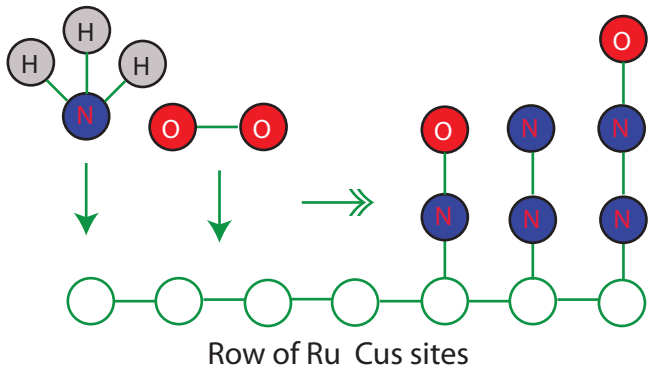

Figure 7.1 Adsorption and desorption reaction steps in NH_3 oxidation on $RuO_2(110)$

KMC study of NH_3 oxidation on $RuO_2(110)$, mimicking UHV conditions [18] we showed that NO selectivity was almost perfect, in agreement with the experiment of Jacobi et al's [17]. Since then, five publication have appeared on similar topics [16, 107–110], some of which use total energy DFT methods to calculate the adsorption geometry and reaction energetics for

either NH_3 or NO on the $RuO_2(110)$ surface. Very briefly, the conclusions from these later publications are: 1) NO adsorption is the rate-limiting step, 2) the contribution of bridge sites in the reaction is negligible, and 3) the lack of N_2O formation in UHV is attributed to slow diffusion of N species[16, 107, 111]. Furthermore, N_2 dominance in experiments performed under ambient pressure is attributed to the facile decomposition of N_2O species to N_2. These conclusions, like many others in the literature, are based only on comparisons of the system total energy. They are thus restricted to considerations thermodynamics at zero-temperature and zero-pressure and do not include any effects of reaction kinetics.

Needless to say, reactivity and selectivity of a catalytic process cannot be judged only in terms of energy barriers of a few key reaction steps. Rather, consideration of competition among various processes, both key and intermediate ones, is essential. Stoichiometric rutile $RuO_2O(110)$ is one of the systems on which KMC simulations have been performed extensively for CO oxidation[112]. Part of the reason is that the surface exhibits a confinement of reaction sites along the one-dimensional rows of under coordinated Ru sites (Figure 7.2) and thus accurate description of localized pair interactions are sufficient. The KMC simulations by Reuter et al have shown that experimental TOF can be reproduced by KMC simulations (only with a small shift of the maximum TOF to a higher ratio of $CO:O_2$) and CO oxidation occurs mainly by reaction of CO_{cus} and O_{cus}[113]. Recent KMC simulations by Farkas et al using experimental reaction constants showed that CO_{br} also plays a significant role in CO oxidation on $RuO_2(110)$[114]. In many aspects NH_3 oxidation on $RuO_2(110)$ is similar

to CO oxidation such that reaction steps mostly occur along the linear chain of Ru_{cus}, but with a significant contribution from the bridge oxygen atoms. With the above background we have carried out KMC simulations of ammonia oxidation reactions using rates calculated with DFT for a set of 36 reactions so as to include the intermediates found in experiments performed under ambient conditions. In this article, we present temperature and pressure dependencies of product selectivity in ammonia oxidation on $RuO_2(110)$ using not only our database of activation energies but also those that are available in the literature and discuss the rationale behind the product selectivity. Note that apart from the inclusion of a larger number of reaction intermediates, we have also included in the present work the role of bridge oxygen atoms. The model and results presented here thus differ substantially from those in our earlier work[18].

7.2 Some Theoretical Details

7.2.1 Modal System

We present a stick-and-ball model for the stoichiometric rutile $RuO_2(110)$ surface in Figure 7.2. In the bulk, the coordination of Ru atoms is six while that of the O atoms is three. The $RuO_2(110)$ surface exposes rows of undercoordinated Ru (Ru_{cus}) and O atoms (O_{br}) (Figure 7.2), both of which have unpaired bonds along the surface normal. Shown in Figure

7.2 are also fully-coordinated Ru and O atoms. NH_3 adsorbs on Ru_{cus} sites and O_2 adsorbs dissociatively with O atoms occupying Ru_{cus} sites on $RuO_2(110)$ surface. Decomposition (or dehydrogenation)of NH_x occurs on the $RuO_2(110)$ via reaction with surface O species: O_{cus} adsorbed on top of Ru_{cus} and O_{br} adsorbed on top of Ru_{br}. Reaction of NH_x with the O species produces NO, N_2, N_2O and H_2O. Some of the elementary reaction steps of theses reactions are shown in Figure 7.1

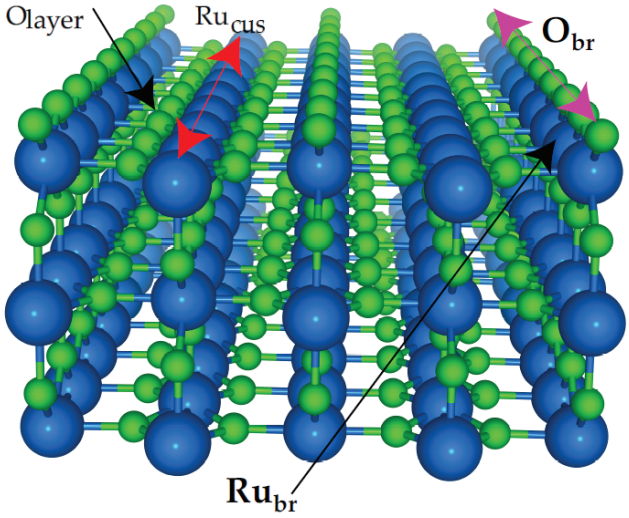

Figure 7.2 A stick-and-ball model of the stoichiometric rutile $RuO_2(110)$ surface

7.2.2 DFT Calculations

We have performed scalar-relativistic, spin-polarized DFT calculations in the ultra-soft pseudo potential scheme [115] and the plane wave basis set to calculate the structures and energetics for the ammonia decomposition reactions on $RuO_2(110)$. We first obtain geometries using non-spin-polarized calculations and then perform the spin-polarized cal-

culations based on the non-spin-polarized geometries. We use the Quantum Espresso [116] code. Our slab consists of three O - RuO - O trilayers of Ru and O atoms, separated by 18 of vacuum. NH_3 and other molecules were adsorbed on one side of the slab only. All atoms in the supercell are fully relaxed. To simulate reaction process of the type A + B = C, we used (3 x 1) surface unit cell of dimension 9.60 x 6.56 $Å^2$, which includes three Ru_{cus} sites. Details of the calculational setup can be found elsewhere [18].

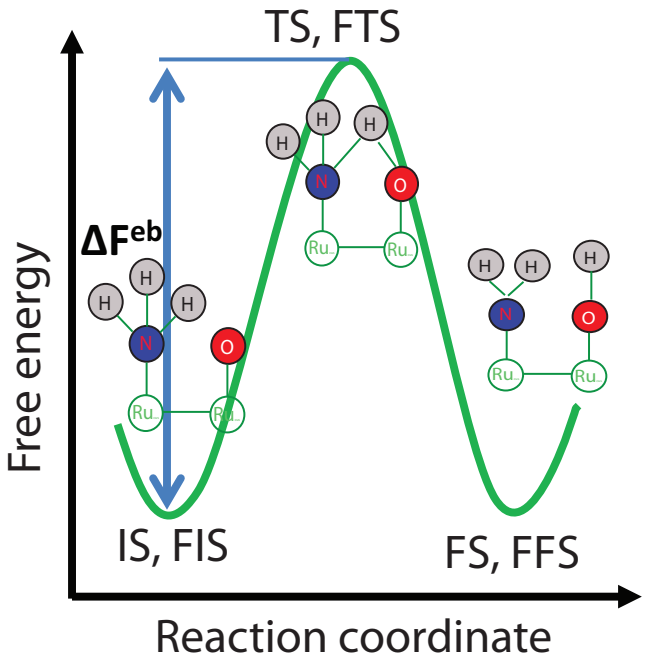

Figure 7.3 Potential energy surface and KMC energy barriers

7.2.3 KMC Algorithm

We evaluate reaction rate of a reaction process on the basis of kinetic expressions derived from transition state theory (TST) [117]. As shown in Figure 7.3, the minimum

(free) energy path (MEP) of reaction process consists of the initial state (IS), transition state (TS), and final state (FS). TS is the saddle point in the MEP; the TST reaction rate, r^{TST}, is the rate of forward crossing of the TS and has the form: $r^{TST} = Ae^{-(\Delta F^{eb})/kT}$, where A and ΔF^{eb} are, respectively, prefactor and activation energy (relative free energy of TS with respect to IS, see Figure 7.3). We evaluate adsorption rate of ammonia and oxygen using: $r^{ads} = (sP/\sigma\sqrt{(2\Pi mKT)})$, where s, P, σ, m, k, and T are the sticking coefficient, partial pressure of ammonia or oxygen, site density, mass of ammonia or oxygen, Boltzmann constant, and temperature, respectively. Flowchart of our KMC algorithm can be found in our previous study [18].

7.2.4 Calculations of Activation Barriers and Prefactors

We have employed climbing image Nudged Elastic Band (CI-NEB) method [32] to calculate minimum energy path (MEP). We have used 8 images for each reaction. During NEB calculations we fix atoms in the bottom tri-layers at their bulk positions while we relax atoms in the topmost layer and molecules. In order to obtain spin-corrected total energy for the initial, transition and final states, we perform a spin-polarized self-consistent calculation for each of the fully relaxed initial, transition and final state geometries from non-spin polarized calculations. Total energies of the IS, FS and TS are then subjected to zero-point corrections. Energy barrier (ΔF^{eb}) for the forward reaction equals to F_{TS} - F_{IS} and that for the reverse reaction equals to F_{TS} - F_{FS}. Total energy difference ΔF (between

initial and final states) is simply F_{FS} - F_{IS}. For a spontaneous process, we set energy barrier for the forward process to zero whereas we set the activation energy for reverse process to total energy difference ΔF. We use a simplified formula for the evaluation of prefactor[30]: A $= \frac{\Pi_i^{3N}(\omega_i^{IS})}{\Pi_i^{3N-1}(\omega_i^{TS})}$, where ω_i are the harmonic vibrational frequencies. For some of the processes (including spontaneous process), we use the standard prefactor (10^{13} s^{-1}).

7.2.5 Databases of Reaction Processes

In this study, we carry out KMC simulations using three databases, one from our own calculations and one each from Wang et al[108] and Perez et al[16]. Our own database for NH_x decomposition on RuO_2(110) consists of 25 processes (36 process if reverse processes are separately counted), which is presented in Table 7.1.

Wang et al's database of NH_x decomposition on RuO_2(110) is presented in Table 7.2, which consists of 20 processes (34 process if reverse processes are separately counted). This database includes reaction steps involving O_{br} species. Perez et al's database which is presented in Table 7.3, consists of 12 processes (process 1 and 2 are added by us to their original database) for each of RuO_2(110) and RuO_2(101) surface. Note that Perez et al's database includes only N and O recombination steps and their resulting secondary reaction steps. It does not have the NH_x dehydrogenation steps. Therefore, KMC simulations of this database cannot be directly compared with the other databases. Since Perez et al and Wang

et al do not report values of prefactors for the reaction rates, we have used the standard prefactor (10^{13} s^{-1}) for all processes in their databases for KMC simulations.

Table 7.1 Our database of 25 processes.

Total energy change (ΔE), energy barrier (E_a), negative frequency (ν), and prefactor (A) are shown. Value in parenthesis is for reverse process.

no.	Reaction	ΔE (eV)	E_a(eV)	ν(meV)	A($10^{13}s^{-1}$
1	$NH_3(gas) \rightarrow NH_{3cus}$	-1.46	0.0	-	1.0
2	$O_2 \rightarrow O_{cus} + O_{cus}$	-1.26	0.0	-	1.0
3	$NH_{3cus} + O_{cus} \rightarrow NH_{2cus} + HO_{cus}$	0.34	0.55	30.74	0.23(0.51)
4	$NH_{2cus} + HO_{cus} \rightarrow NH_{cus} + H_2O_{cus}$	0.48	0.71	-	1
5	$NH_{2cus} + O_{cus} \rightarrow N_{cus} + H_2O_{cus}$	-0.41	0.37	-	1
6	$NH_{cus} + HO_{cus} \rightarrow N_{cus} + H_2O_{cus}$	-0.65	0.0	-	1
7	$NH_{cus} + O_{cus} \rightarrow N_{cus} + OH_{cus}$	-0.82	0.0	-	1
8	$H_2O_{br} \rightarrow H_2O$(gas)	-	0.85	-	1
9	$H_2O_{cus} \rightarrow H_2O$(gas)	-	1.30	-	1
10	$N_{cus} + O_{cus} \rightarrow NO_{cus}$	-2.89	0.18	11.47	0.28(0.226)
11	$NO_{cus} \rightarrow NO$(gas)	1.72	1.72	-	1
12	$N_{cus} + N_{cus} \rightarrow N_2$(gas)	0.27	0.27	44.77	0.4
13	$NO_{cus} \rightarrow NO_{cus}$(diffusion)	0.00	1.42	8.50	0.22
14	$N_{cus} \rightarrow N_{cus}$(diffusion)	0.0	1.13	14.37	0.35
15	$O_{cus} \rightarrow O_{cus}$(diffusion)	0.0	1.05	12.38	0.31
16	$OH_{cus} \rightarrow OH_{cus}$(diffusion)	0.0	0.91	8.01	0.19
17	$NH_{cus} + O_{br} \rightarrow N_{cus} + OH_{br}$	-2.02	0.0	-	1
18	$OH_{br} + O_{br} \rightarrow O_{br} + OH_{br}$	0.0	2.23	-	1
19	$OH_{br} + OH_{br} \rightarrow H_2O_{br} + O_{br}$	2.21	0.0	-	1
20	$O_{cus} \rightarrow_{br}$(diffusion to O_{br} vacancy)	-1.37	0.66	-	1
21	$NO_{cus} + N_{cus} \rightarrow N_2O_{cus}$	-1.34	0.79	30.45	0.087/0.168
22	$N_{2cus} + O_{cus} \rightarrow N_2O_{cus}$	1.02	0.0	-	0.1
23	$N_2O_{cus} \rightarrow N_2O$(gas)	0.47	0.0	-	1
24	$N_2O_{cus} \rightarrow O_{cus} + N_2$(gas)	1.02	0.81	67.56	0.09
25	$N_{2cus} + O_{cus} \rightarrow O_{cus} + N_2$(gas)	-	0.58	-	1

Table 7.2 Wang et al's database.

Total energy change (ΔE), energy barrier (E_a) and negative frequency (ν). Value in parenthesis is for reverse process.

no.	Reaction	ΔE (eV)	E_a(eV)	ν(meV)
1	$NH_3(gas) \rightarrow NH_{3cus}$	1.56	-	-
2	$O_2 \rightarrow O_{cus} + O_{cus}$	1.26	-	-
3	$NH_{3cus} + O_{cus} \rightarrow NH_{2cus} + HO_{cus}$	0.62	0.71(0.09)	157
4	$NH_{2cus} + HO_{cus} \rightarrow NH_{cus} + H_2O_{cus}$	0.31	0.31(0.0)	679
5	$NH_{2cus} + O_{cus} \rightarrow NH_{cus} + HO_{cus}$	0.34	0.48(0.14)	897
6	$NH_{cus} + HO_{cus} \rightarrow N_{cus} + H_2O$	-0.93	0.0(0.93)	-
7	$NH_{cus} + O_{cus} \rightarrow N_{cus} + OH_{cus}$	-0.82	0.0(0.82)	-
8	$NH_{2cus} + O_{br} \rightarrow NH_{cus} + OH_{br}$	0.11	0.86(0.75)	255
9	$NH_{cus2} + O_{br} \rightarrow N_{cus} + OH_{br}$	-0.78	0.00(0.78)	-
10	$N_{cus} + O_{cus} \rightarrow N_{cus}O$	-1.82	0.47(2.29)	610
11	$N_{cus} + O_{br} \rightarrow NO$cus	0.03	0.89(0.86)	568
12	$N_{cus}O + N_{cus} \rightarrow N_{cus}$NO	-0.98	0.85(1.83)	444
13	$N_{cus} + N_{cus} \rightarrow N_{2cus}$	-3.79	0.20(3.99)	579
14	$N_{cus}O \rightarrow NO$(gas)	-	2.09	-
15	$H_2O_{cus} \rightarrow H_2O$(gas)	-	1.22	-
16	$H_2O_{br} \rightarrow H_2O$(gas)	-	0.70	-
17	$N_{2cus} \rightarrow N_2$(gas)	-	0.53	-
18	$N_{cus}NO \rightarrow N_2O$(gas)	-	0.52	-
19	$OH_{br} \rightarrow OH_{br}$	-	2.25	-
19	$NH_{cus} + OH_{br} \rightarrow N_{cus} + H_2O_{br}$	0.47	0.48	-

7.3 Results and Discussion

We discuss the structure and energetics of the reaction steps of NH_x decomposition on RuO_2(110) and compare them with other studies (See Table 7.4 & Table 7.5). Discussion of KMC results and their implications follow.

Table 7.3 Perez et al's database.

Total energy change (ΔE), energy barrier (E_a) and negative frequency (ν). Value in parenthesis are for (101)surface.

no.	Reaction	ΔE (eV)	E_a(eV)	ν(meV)
1	$\cdot_{cus} + N(gas) \rightarrow N_{cus}$	0.0(0.0)	-(-)	-(-)
2	$\cdot_{cus} + O(gas) \rightarrow O_{cus}$	0.0(0.0)	-(-)	-(-)
3	$N_{cus} + N_{cus} \rightarrow N_2$(gas)	-3.41(-4.41)	1.11(0.58)	80(56)
4	$N_{cus} + O_{cus} \rightarrow NO$cus	-1.87(-2.18)	1.01(0.72)	75(66)
5	$N_{cus} + O_{cus} \rightarrow ON_{cus}$	-0.98(-0.82)	1.01(0.72)	76(66)
6	$NO_{cus} \rightarrow NO$(gas)	-	1.78(1.49)	-
7	$ON_{cus} \rightarrow NO$(gas)	-	0.31(0.11)	-
8	$O_{cus} + O_{cus} \rightarrow O_2$	0.50(0.67)	1.11(0.96)	585(537)
9	$O_{2cus} \rightarrow O_2$(gas)	-	0.67(0.23)	-
10	$NO_{cus} + N_{cus} \rightarrow N_2O_{cus}$	-1.16(-1.42)	1.30(1.23)	48(16)
11	$N_2O_{cus} \rightarrow N_2O$(gas)	-	0.26(0.11)	-
12	$NO_{cus} + N_{cus} \rightarrow NNO_{cus}$	-0.85(-0.68)	1.04(0.76)	30(52)
13	$NNO_{cus} \rightarrow O_{cus} + N_2$(gas)	-1.42(-1.31)	0.31(0.21)	66(57)
14	$NO_{cus} \rightarrow ON_{cus}$ (rotation)	1.45(1.37)	1.63(1.66)	62(21)

Table 7.4 Geometrical parameters (in angstrom) of various species on RuO_2(110) surface.

Species	This study d(Ru-X) (X=N, O)	d(N-X) (X=N, O) for N_aO_b(a, b=0-2) (X=H for NH_3)	d(Ru-X) (X=N, O)	[1] d(N-X) X = N, O
NO_{cus}	1.81	1.16	-	-
$NO(O)_{cus}$	1.84	1.16	1.78	1.17
$NO(N)_{cus}$	1.85(1.81)	1.16	-	-
NO_{2cus}	1.85(1.71)	1.16	-	-
N_2O_{cus}	2.19, 2.19, 3.06	1.32, 1.21	-	-
NH_3	2.13	1.14	2.06	1.14
N_2	2.18	1.03	-	-

[1] = Ref [111] (VASP/PW91).

7.3.1 Structure and Energetics of NH_x Oxidation Steps on $RuO_2(110)$

Many of the reaction steps of NH_x on $RuO_2(110)$ were discussed in our previous study [18]. Thus, in this section, while we still present the description for some key processes, we mostly present non-overlapping results. In all figures involving reaction geometries, Ru atoms are green colored, Oxygen atoms are represented in blue color, Nitrogen atoms in gray color whereas hydrogen atoms are represented by light blue color.

Table 7.5 Comparison of calculated energy barriers of key reaction steps

Reaction	This study (QE/PBE)	[1]	[2]	[3]	[4]
$N_{cus} + O_{cus} \rightarrow NO_{cus}$	0.18	0.47	0.79	0.70	1.01
$N_{cus} + N_{cus} \rightarrow N_2$(gas)	0.27	0.20	-	0.80	1.11
$NO_{cus} + N_{cus} \rightarrow NNO_{cus}$	0.79	0.85	-	1.22	1.30
$NNO_{cus} \rightarrow O_{cus} + N_2$(gas)	0.58	1.35	-	0.31	
NO (diffusion)	1.42	-	1.80	1.67	
N (diffusion)	1.05	-	-	2.0	

[1] = Ref [111] (VASP/PW91).
[2] = Ref [107] (VASP/PBE).
[3] = Ref [109] (VASP/PW91).
[4] = Ref [16] (VASP/RPBE).

7.3.2 H-Abstraction Processes Via O_{cus}

The entire process of NH_3 decomposition on $RuO_2(110)$ can be summarized in a single step: $4NH_3 + 3O_2 \rightarrow 4N + 6H_2O$. The three H atoms of NH_3 can be dehydrogenated either in three sequential steps or in two concerted steps. The final product is N regardless of the routes. In both routes, the initial step is H abstraction by O_{cus}. The energy barrier of this

initial step is 0.55 eV. This step is an endothermic reaction with the energy deficiency of 0.34 eV. The IS, TS and FS for this reaction are presented in Figure 7.4. The corresponding energy barrier reported by Wang et al is 0.71. In the successive dehydrogenation route, the second step is the activation of NH_2 by HO_{cus} with energy barrier of 0.71 eV. This is also an endothermic reaction ($\Delta E = 0.48$ eV). The resulting final products are NH_{cus} and H_2O_{cus}. TS and FS of this step are shown in Figure 7.5. The corresponding barrier obtained by Wang et al is 0.31 eV. In the final step of the successive dehydrogenation route, NH_{cus} reacts with either OH_{cus} or O_{cus}. Regardless of reaction counterpart, they are both spontaneous and down-hill.

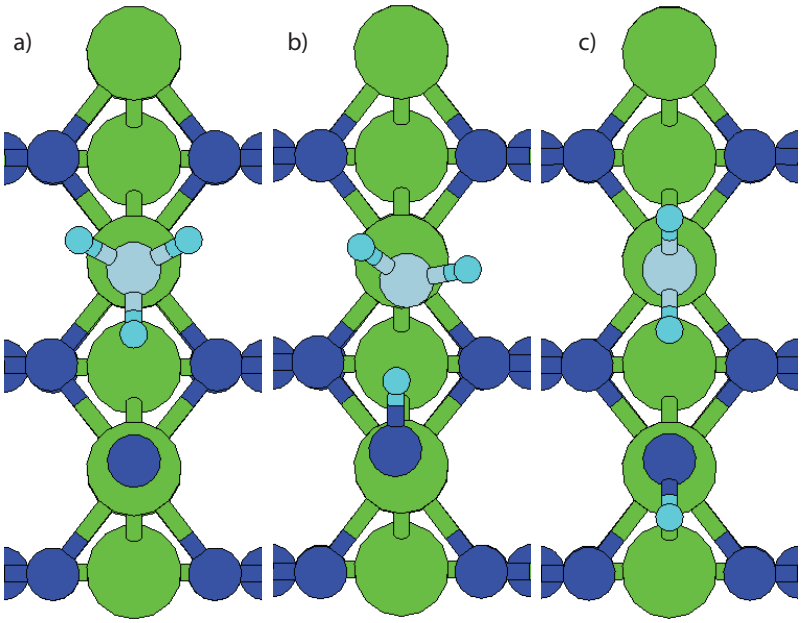

Figure 7.4 Optimized geometries for (a) Initial, (b) Transition and (c) Final states for NH_3+O $\rightarrow$ NH_2+OH reaction.

In the concerted dehydrogenation route, two H abstraction events occur by O_{cus} in a concerted motion, which is shown in Figure 7.6. In this motion, the moment the first H is transferred to O_{cus}, the second H turns by 90 degree. Finally, the rotated H makes bond with the just formed HO_{cus}. This step is an exothermic reaction ($\Delta E = 0.41$ eV) with energy barrier of 0.37 eV.

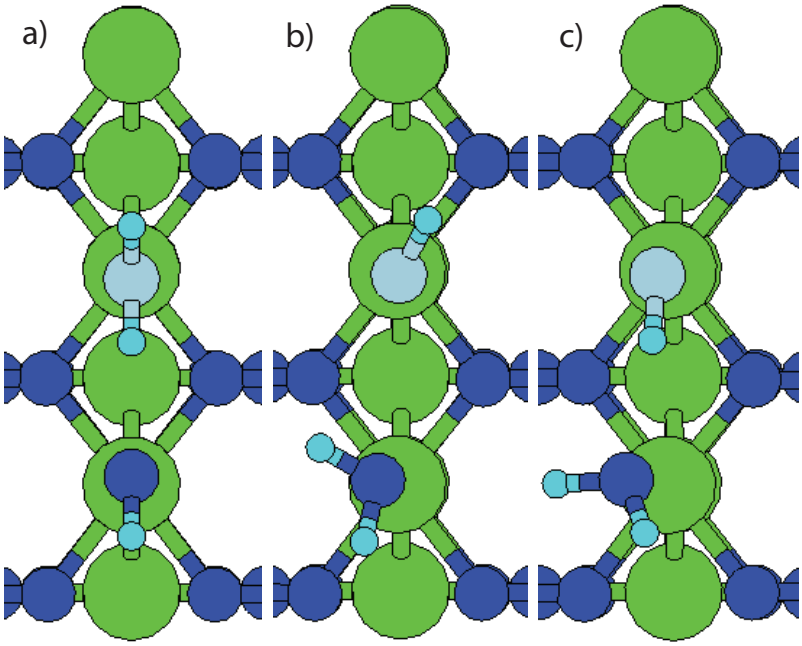

Figure 7.5 Optimized geometries for (a) Initial, (b) Transition and (c) Final states for NH_2+OH $\rightarrow$ NH+H_2O reaction.

7.3.3 H-Abstraction Processes Via O_{br}

In principle, NH_x can also be dehydrogenated by bridge O species (i.e. by O_{br} and HO_{br}). We find that the barrier by O_{br} is 0.47 eV for forward reaction and 0.09 eV for

reverse reaction. Similarly, Wang et al find them to be 0.44 eV and 0.01 eV, respectively. However, our KMC simulations find that the contribution of this route to NH_3 decomposition is effectively zero in agreement with experiment, such that NH_3 does not react on the stoichiometric $RuO_2(110)$ surface [18, 108]. Similarly, dehydrogenation of NH_2 by O_{br} species is also ignorable. (For this reason we do not include them in our actual simulations.) However, O_{br}-induced decomposition of NH species is different and significantly contributes to N_{cus} formation as shall be discussed later.

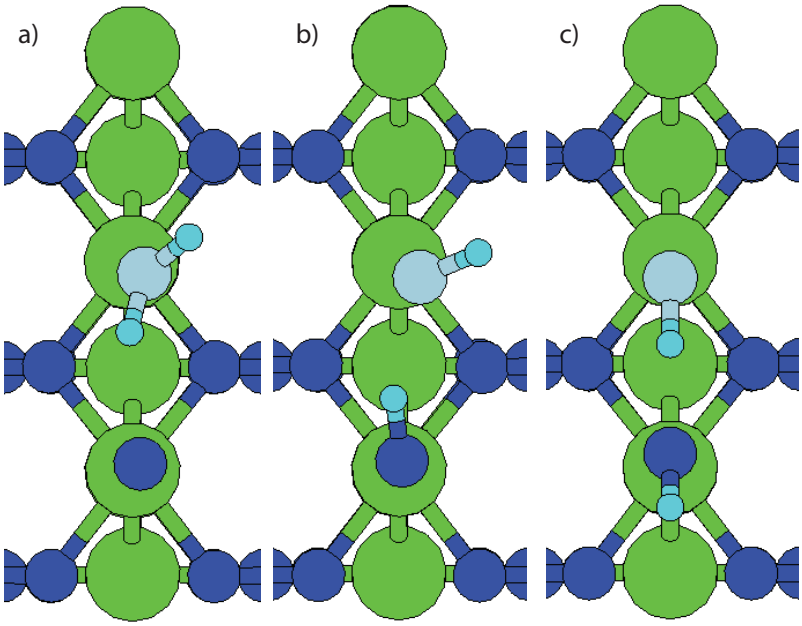

Figure 7.6 Optimized geometries for (a) Initial, (b) Transition and (c) Final states for NH_2+O $\rightarrow$ N+H_2O, concerted dehydrogenation reaction.

7.3.4 NO and N_2 Formation

Using CINEB we recalculated the energy barrier of N+O recombination (i.e. NO formation) to find almost the same energy barrier of 0.18 eV (0.13 eV without zero-point correction) as in the previous study[18]. Nevertheless, other studies report a higher energy barrier in range of 0.47 and 1.01 eV (See Table 7.5). IS, TS, and FS for this step is presented in Figure 7.7. The reverse barrier is 3.07 eV. The final product NO binds vertically to Ru_{cus} with the bond length, d(Ru-N), of 1.84 and with the intramolecular bond length, d(N-O), of 1.78 (See Table 5). Its desorption barrier is very large, 1.72 eV (2.16 eV without zero-point correction). Wang et al[108] and Schneider et al [109] reports a desorption energy of 2.09 and 2.21 eV, respectively, similar to our uncorrected one. On the other hand, Perez et al [16] reports a rather smaller adsorption energy of 1.78 eV.

The energy barrier for N_2 formation via N + N recombination, is 0.27 eV. We find that once formed it spontaneously desorbs. The IS, TS, and FS are as shown in Figure 7.8.

7.3.5 N_2O Formation

Once NO_{cus} is formed, it can either desorb as NO or recombine with N_{cus} to form N_2O_{cus}. (Another possibility is to recombine with O_{cus} to form NO_2. However, NO_2 is never observed in experiment.) TS and FS for the latter step are presented in Figure 7.9. Recombination of NO_{cus} with N_{cus} is an exothermic reaction with an energy barrier of

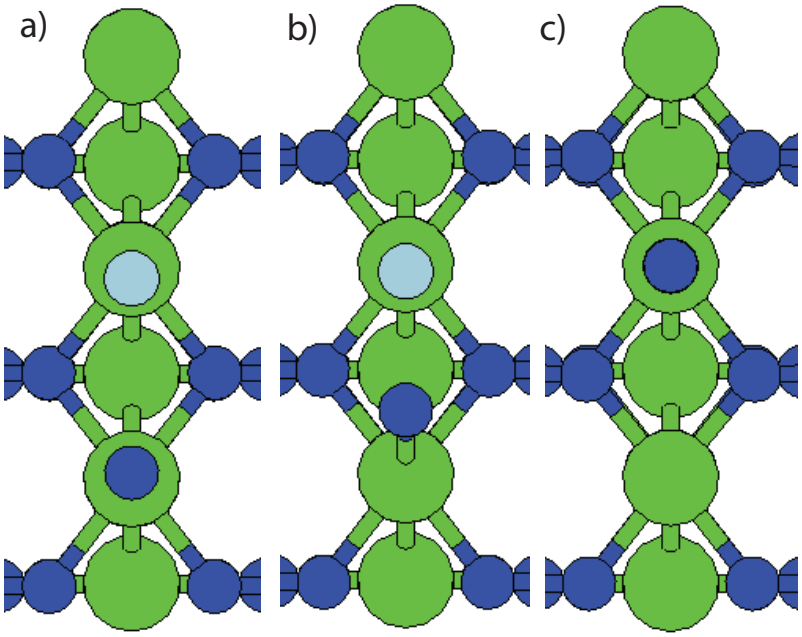

Figure 7.7 Optimized geometries for (a) Initial, (b) Transition and (c) Final states for NO formation reaction.

0.76 eV (0.79 eV with zero point correction. See Table 7.1). In this reaction, horizontal N_2O species (Figure 7.9(b)) forms as an intermediate. While it has a lower energy than IS (Figure 7.9(a)) by 1.33 eV, its energy is higher than vertical N_2O by 0.26 eV. The horizontal N_2O is unstable and converts to the stable vertical N_2O (Figure 7.9(c)), which is FS. Our calculated energy barrier for the whole reaction is 0.76 eV and is in close agreement with that of Wang et al. (0.85 eV) whereas Schneider et al and Perez et al report quite a larger energy barrier (1.22 and 1.30 eV, respectively). See Table 7.5. Other notable difference is the energy difference between IS and FS. Ours is -1.59 eV, but other studies report a smaller value in the range of -0.56 eV [109] and -1.16 eV [16]. In terms of the geometry of N_2O, our calculated structural parameters are in good agreement with those of Wang et al (see Table

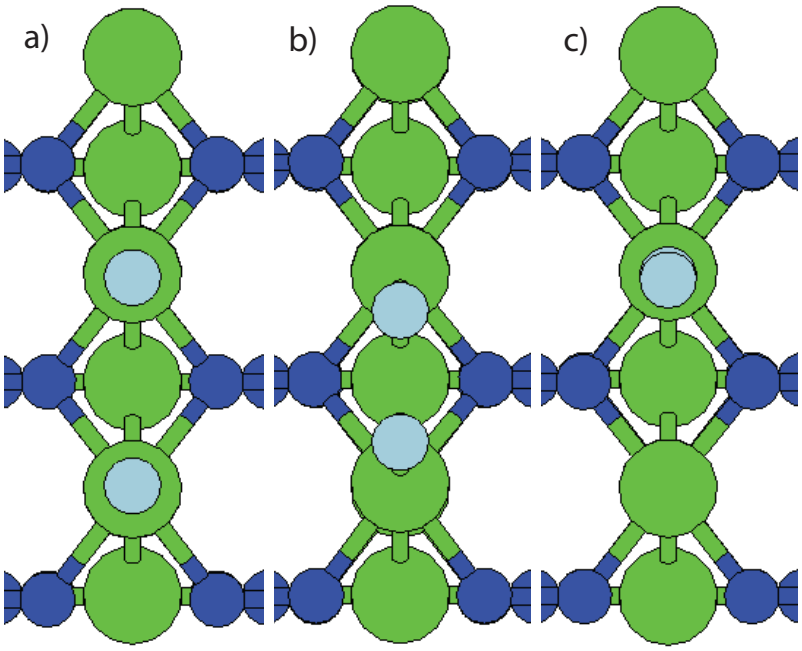

Figure 7.8 Optimized geometries for (a) Initial, (b) Transition and (c) Final states for N+N recombination reaction.

7.4) in addition to the monodentate, vertical N_2O species. Their bidentate N_2O is similar to our horizontal N_2O in Figure 7.9(b) and thus binds to two neighboring Ru_{cus} atoms via both N and O ends. However, none of other studies has found such bidentate N_2O. Thus, the (stable) horizontal, bidentate N_2O species is unique in Perez et al's calculations.

7.3.6 N_2O Decomposition and Desorption

N_2O on $RuO_2(110)$ can either desorb as N_2O or decompose to N_2. For desorption, it needs to overcome energy barrier of 0.47 eV in good agreement with that of Wang et al (0.52 eV) whereas Perez et al reports a smaller desorption barrier (0.26 eV). In the decomposition

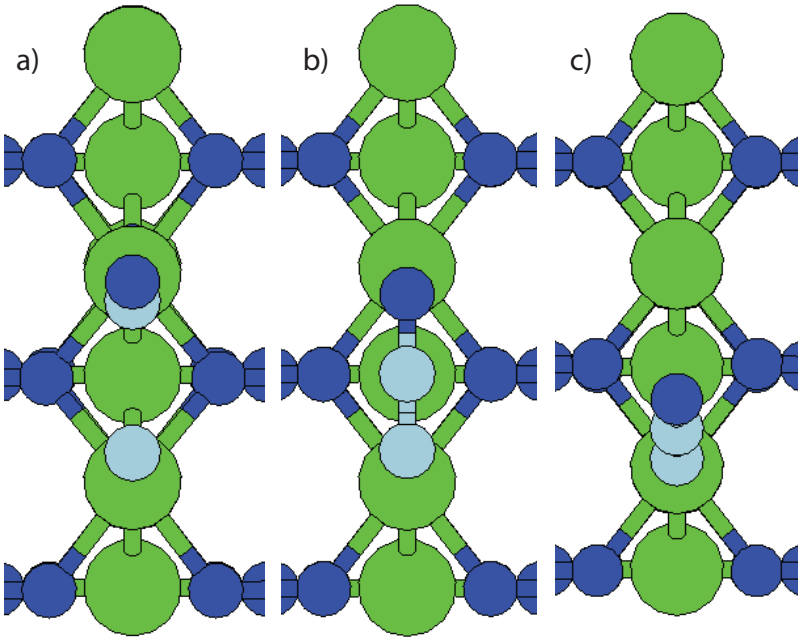

Figure 7.9 Optimized geometries for (a) Transition state, (b) Horizontal final state and (c) Vertical final state for NO+N recombination reaction.

route to N_2 (Figure 7.10), it needs to overcome energy barrier of 0.55 eV. We find this step to be exothermic by 0.47 eV with the reverse energy barrier of 1.02 eV and is an important route for N_2 formation on $RuO_2(110)$.

In contrast, Wang et al reports a much larger N_2O decomposition barrier (1.83 eV), which they attribute to a large separation of N_2O from the $RuO_2(110)$ surface. However, we believe that the large separation is not the cause since the rotation of the vertical N_2O (Figure 7.10(a)) to horizontal N_2O (Figure 7.10(b)) only takes 0.26 eV. Thus, we believe that there may be another reason for the large barrier. In fact we find that their large barrier could be an artifact of NEB calculations. In fact, we could reproduce the energy barrier if we use NEB images generated by direct interpolation of IS (Figure 7.10(a)) and FS (Figure

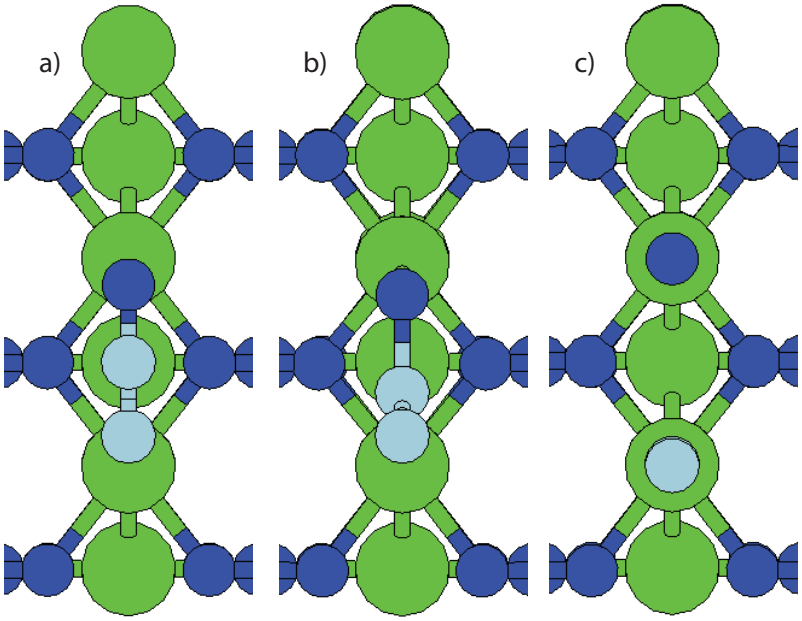

Figure 7.10 Optimized geometries for (a) Initial (b) Transition and (c) Final state for N_2O decomposition reaction.

7.10(d)) because they do not follow the MEP. Such NEB route is found to elongate the stiff N-O bond length and thus causes a large TS energy. Our workaround for the problem is to use the horizontal N_2O as IS. Then, NEB yields a much smaller barrier of 0.55 eV. On the other hand, Perez et al reports a remarkably small decomposition barrier of 0.26 eV. In fact, this is the energy barrier for the horizontal, bidentate N_2O, which is similar to that in Figure 7.10(b). They do not report an energy barrier for the direct decomposition of vertical N_2O to N_2.

7.3.7 Diffusion Processes

For N diffusion from one Ru_{cus} to the nearest neighbor Ru_{cus}, we find a diffusion barrier of 1.13 eV. We also find energy barrier for O diffusion from Ru_{cus} to the nearest neighbor Ru_{cus} to be 1.05 eV, similar to that of N diffusion. For NO diffusion from Ru_{cus} to Ru_{cus}, we find a barrier of 1.42 eV. There exists substantial discrepancy among theories regarding N, O, and NO diffusion (SeeTable 7.5). Basically, other studies find (much) higher diffusion barrier for them. Energy barrier for OH diffusion along the linear chain of Ru_{cus} is 0.91 eV. TS for the diffusion of N, O, and NO along the linear chain of Ru_{cus} are shown in Figure 7.11 (a), (b) & (c).

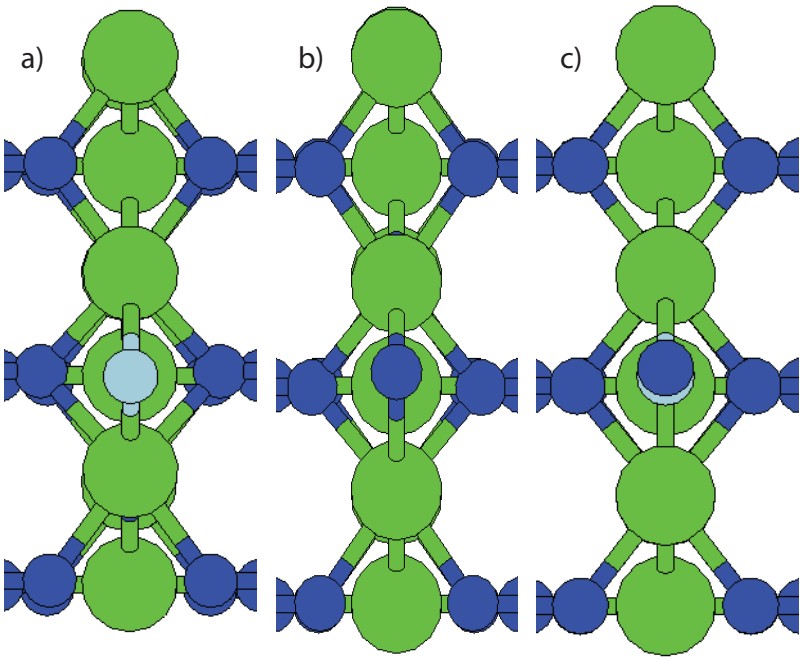

Figure 7.11 Optimized geometries for the transition state of the diffusion processes of (a) N (b) O and (c) NO.

For H to Diffuse along the linear chain of O_{br} it needs to overcome a large energy barrier of 2.23 eV. Similarly, H diffusion from O_{br} to the nearest neighboring HO_{br}, which leads to the formation of H_2O_{br} species, has a large energy barrier of 2.21 eV with the reverse energy barrier of 1.20 eV. Thus, the formation of H_2O_{br} via H diffusion along the linear chain of O_{br} is a rare event. This result indicates that O-vacancy formation on $RuO_2(110)$ during the reaction is rare.

7.3.8 KMC Simulations: Reaction Rate and Selectivity

We present KMC results from our and Wang's databases for UHV conditions in Figure 7.12 and then discuss the ambient results in comparison.

7.3.8.1 UHV Results

In our previous study, we found more than 93% NO selectivity in good agreement with the UHV experiment by Jacobi et al [17]. However, in that study, we employed a few approximations and adjustments. For example, we treated H_2O desorption as spontaneous and we did not include N_2O- and O_{br}-involving processes. In this study we not only exclude such adjustments but also include these secondary reaction processes in our simulations. We present these KMC results in Figure 7.12(a). First of all, the results for 630K are in good agreement with our previous result. Basically, NO selectivity reaches nearly 100 % at 630K (see Figure 7.12(a)).

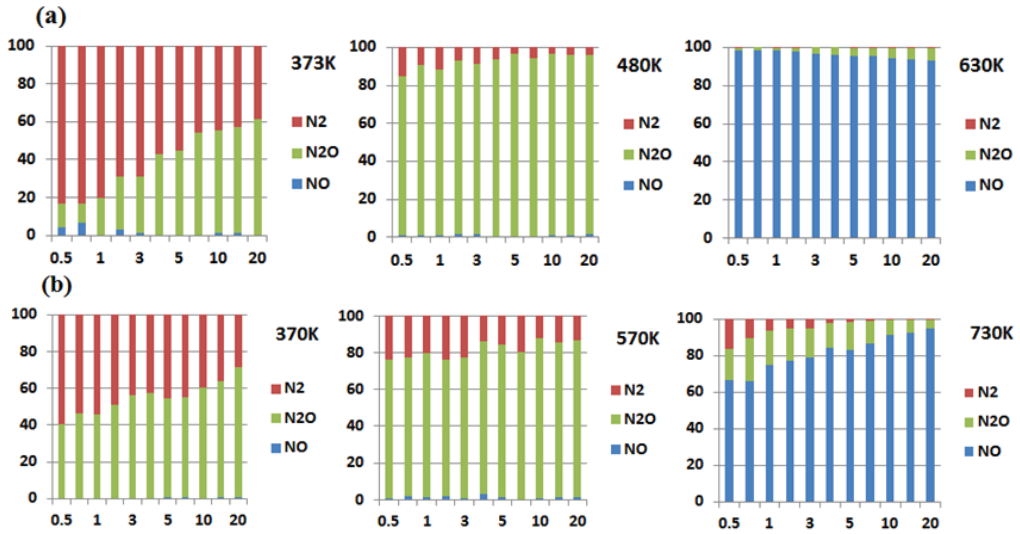

Figure 7.12 Selectivity of N_2, N_2O and NO on $RuO_2(110)$ in UHV conditions obtained using: (a) our database, (b) Wang et al's database.

However, inclusion of N_2O related processes drastically changes the landscape of product selectivity at lower temperatures. The dominant product changes from N_2 at low temperatures to N_2O at intermediate temperatures, to NO at high temperatures (630K). Not only temperature but pressure also has strong impact on product selectivity, particularly in the low temperature range. At 373K, N_2 is the dominant product only for $O_2/NH_3 < 5$, but for higher O_2/NH_3, N_2O becomes the dominant product owing to the fact that at higher O_2/NH_3, as the surface coverage of Ocus increases, NOcus formation increases, which is the necessary condition for N_2O formation on $RuO_2(110)$. N_2O dominance with arising temperature in all O_2/NH_3 range, is a result of the activation of the secondary reaction of $NO_{cus} + N_{cus}$. Our simulations show that thus-formed N_2O does not decompose to N_2 in UHV condition. As a result, every N_2O desorbs as N_2O. On the other hand, NO high

selectivity at 630K and beyond is a result of thermal activation of NO_{cus} desorption. A similar trend is obtained for Wang's database. Note that the peak NO desorption occurs around 750K in Wang et al's database (NO desorption barrier: 2.09 eV). Regarding participation of O_{br} in ammonia oxidation reaction on $RuO_2(110)$, KMC simulations for both databases show that the contribution of O_{br}-induced dehydrogenation of NH_x (x=2,3) species is effectively zero (in agreement with Jacobi et al's UHV experiment) but O_{br}-induced dehydrogenation of NH species, which leads to the formation of N, is not negligible, particularly at low temperature. In sum, NH_x (x=2,3) dehydrogenation can be done only by O_{cus} and OH_{cus}, but NH_{cus} dehydrogenation can be done by both O_{cus} and O_{br} species.

7.3.9 Ambient Pressure Results

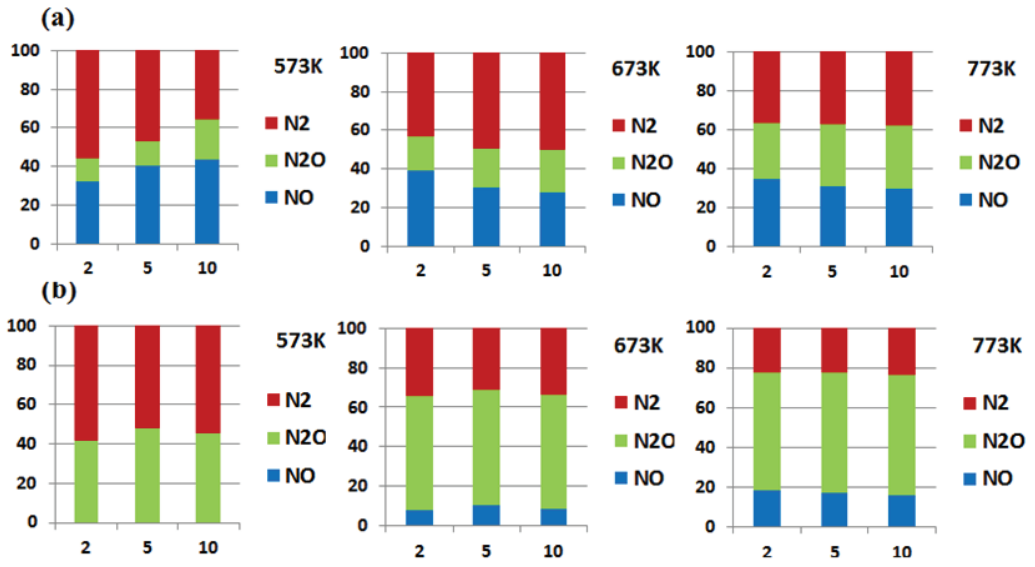

Figure 7.13 Selectivity of N_2, N_2O and NO on $RuO_2(110)$ at ambient condition obtained using: (a) our database (b) Wang et al's database.

In a recent study on ammonia oxidation on polycrystalline RuO_2 samples[16] Perez et al showed in the steady state measurement that NO selectivity is low, below 10% at ambient pressure, in marked contrast to the nearly 100% selectivity in UHV case. Instead, they showed that N_2 is the dominant product with more than 80% selectivity, thus indicating a pressure gap in ammonia oxidation on $RuO_2(110)$. Moreover, as the experiment was done for polycrystalline RuO_2 samples, the reported high selectivity of N_2 could indicate a material gap as well if the selectivity strongly depend on the surface orientation. Here we present the ambient pressure KMC results in Figure 7.13.

7.3.9.1 KMC Results Using Our Database

We present KMC results from our database in Figure 7.13(a). We find that (1) N_2 is the major product in nearly all ranges investigated although N_2 selectivity midly reduces as temperature rises; (2) N_2O selectivity is minor but it increases with temperature, and (3) NO selectivity maintains a substantial portion (28 - 43%). It is remarkable that our KMC calculations predict N_2 to be the major product, despite rather small selectivity(35% - 56%). In experiment, however, N_2 is the dominant product with selectivity of more than 80%. Thus, our results is in qualitative agreement with the experiment. We would like to emphasize that this result is clearly in contrast to the UHV results (Figure 7.12(a)) described earlier, where NO is the dominant species with nearly 100% selectivity in similar temperature and O_2/NH_3 ratios. (absolute pressure differs by 8 orders of magnitude). Thus, our KMC

calculations confirm the experimental finding that there is a pressure gap in the ammonia oxidation reaction on $RuO_2(110)$ surface.

Then, what would be the rationale.? There are two routes for N_2 formation: N_{cus}+N_{cus} recombination and N_2O decomposition. Our KMC simulations show that the dominant route is N_{cus}+N_{cus} recombination and the contribution by N_2O decomposition is negligible. Recall that the same conclusion was obtained for the UHV case. We find that the active N+N recombination is made possible by the abundant supply of N_{cus} species which is a result of active decomposition of NH_x in ambient condition. This finding is in contrast to Perez et al's conclusion that N_2O decomposition is the rationale for N_2 dominance in ambient pressure. In fact, the negligible contribution of N_2O decomposition is a result of the competition with the direct desorption of N_2O. The former is activated by 0.55 eV and the latter by 0.47 eV and the prefactor of the former is smaller than that of the latter by an order of magnitude. These differences causes the majority of N_2O_{cus} to desorb rather than decompose to N_2. Hypothetically if we set the decomposition barrier to a much smaller one 0.31 eV, as reported by Perez et al, then, our KMC simulations predicts that nearly half of N_2O_{cus} would decompose to N_2, but the impact of this adjustment is not remarkable such that improved N_2 selectivity is only about 54% at 773K. Thus, our KMC simulations indicate that N_2O decomposition may not be the dominant cause for N_2 selectivity in ambient pressure. In sum, our KMC simulations do not predict a high N_2 selectivity as observed in the steady state experiment by Perez et al. As a matter of fact, they also reported product selectivity

from pulse experiment with O_{2eff}/NH_3=30 that N_2 was in range of 50% and 60% in all temperature range investigated. Actually our KMC results are in better agreement with the pulse experiment.

7.3.9.2 KMC Results Using Wang et al's Database

We present KMC results from Wang et al's database in Figure 7.13(b). They exhibit similar trends found in our database. However, there are remarkable differences from our database such that (1) N_2 (and NO) are only minor products and (2) N_2O is the dominant product. These major differences arise from different N_2O decomposition barrier (1.35 eV vs. 0.81 eV). The high selectivity of N_2O (and the small selectivity of NO below 20%) in their database is a result of the competition of NO desorption and NO+N recombination. The former is activated by 2.09 eV and the latter by 0.85 eV. Thus, the latter is so much favored than the former so that the majority of NO_{cus} converts to N_2O_{cus}. Thus-formed N_2O can either desorb as N_2O or decompose to N_2. N_2O decomposition to N_2 is, however, negligible because of the high energy barrier of 1.35 eV, as in our database. If we set the decomposition barrier to 0.31 eV as we did for our database, KMC simulations show that nearly half of N_2O_{cus} would decompose to N_2 resulting in an improved N_2 selectivity of 53% at 773K, a similar value obtained for our database. Thus, Wang's database produces similar results to our database once N_2O decomposition barrier is set to same.

7.3.9.3 KMC Results Using Perez et al's Database

A nice aspect of Perez et al's database is that it has processes for both (110) and (101) surfaces, thus giving a chance to compare relative reactivity between different surface orientations. Before we present their results, we would like to emphasize that Perez et al's databases do not include NH_x decomposition processes. Simulation with such a database is not straightforward and requires some adjustments. For example, we assumed that the surface is in contact with the (fictitious) gas mixture of N and O atoms. In fact, this means that we have added the adsorption process of N and O atoms to their original database. On the other hand, we do not know the precise pressure for incident N and O atoms that would represent the formation rate of N and O atoms at the RuO_2 surface. A simple approach we took is to scan both relative and absolute pressure of O and N atoms i.e., we varied O/N ratio from 0.5 to 20 for two absolute pressures: p(N)=10^{-7} (named "UHV" case) and 10^{1} mbar (named "AMB" case). This said, we present results from Perez et al's databases in Figure 7.14. RuO_2(1101) surface give almost identical result as RuO_2(101) surface (Compare Figure 7.14(b) and Figure 7.14(c)). Thus we find no material gap in ambient pressure in agreement with Perez et al. The most surprising result is the NO dominance in nearly all temperature and pressure range. Thus, the KMC simulations of their database indicate no pressure gap, which is in apparent disagreement with their experiment and other databases. On the one hand, this failure may simply reflect the incompleteness of their database. Analysis of the

KMC results for their database reveals that at higher O/N ratio > 3, surface O species poisons the secondary reaction of NO_{cus} (NO_{cus} + N_{cus}). (This is true regardless of the magnitude of absolute pressure of N and O.) As a result, the formation rate of N_2O species effectively reduces by a factor of 2 from O/N= 2 to O/N= 5 and so does N_2 formation. This explains why N2 selectivity drops so quickly as O/N increases. Since diffusivity of O_{cus}, N_{cus}, NO_{cus} and other surface species is zero in Perez et al's database, they occupy their adsorption sites permanently unless "proper" reactants fall from the sky next to them. In case that "improper" species fall, then their sites are permanently blocked. Therefore, the coverage induced poisoning effect is much more dramatic in their database than in our database.

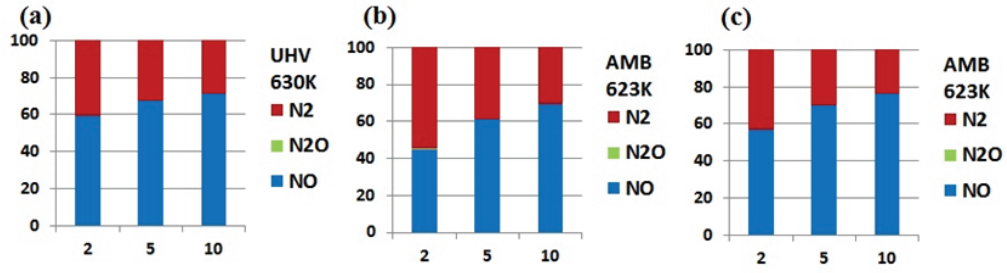

Figure 7.14 Selectivity of N_2, N_2O and NO at: (a) UHV, (b) AMB conditions for RuO_2 (110), (c) AMB conditions for RuO_2 (101) surface obtained using Perez et al's databases.

On the other hand, this is a good example that shows a pitfall of estimation of reactivity (selectivity) solely on the basis of energetics. Since Perez et al's database provides a low-energy barrier N_2O decomposition process (for example, decomposition of NNO_{cus} to N_2 requires only 0.31 eV and is in fact the lowest energy barrier process in the database -

it is true that effectively every NNO_{cus} converts to N_2 in their database) it is easy to draw a conclusion that N_2 is the dominant product because of facile conversion of N_2O to N_2. (This was in fact the conclusion drawn by Perez et al on the basis of the 12 processes in their database.) However, reactions on catalytic surface are inevitably sensitive to the local environment of the catalytic surface such as surface coverage and diffusivity of reactants and site blocking. Therefore, it is important to consider various local interactions between surface species i.e. the competition of all directly and indirectly related reaction processes rather than a few individual reaction steps of interest. In sum, KMC simulations of Perez et al's databases show that simple estimation based on energetics of key processes could lead to a wrong conclusion suggesting the importance of kinetic simulations for reliable description of reaction rate and selectivity of a catalytic system.

7.4 Conclusions

We have performed KMC simulations in ambient conditions for ammonia oxidation in $RuO_2(110)$ surface using available databases, which were proposed by Perez et al and Wang et al as well as our own database of 25 processes. First of all, KMC results for all databases show that NO is the dominant species in UHV conditions at or above the peak NO desorption temperature, confirming the Jacobi et al's UHV results. In contrast, ambient KMC results using our database show that NO_2 is the dominant product in agreement with recent ambient

pressure experiment by Perez et al. Thus, our KMC simulations confirms a pressure gap in the ammonia oxidation reaction on $RuO_2(110)$ surface. However, NO_2 selectivity is at best 50% in contrast to 80% in experiment. The rationale for the pressure gap is the active recombination of N + N owing to the abundant supply of N species in ambient pressure, as a result of active NH_x decomposition by plenty O species on $RuO_2(110)$ surface. Finally, we showed that simple estimation of selectivity based solely on the energetics of some key processes could be unreliable, and thus prediction of selectivity requires consideration of local interaction of all surface species present on catalytic surface.

CHAPTER 8
CONCLUSIONS AND FUTURE DIRECTIONS

8.1 Conclusions

This dissertation describes, using DFT, KMC, SLKMC and SLKMC-II methods, the spatial and temporal evolution of islands and molecules on the surfaces from energetics and kinetics point of view.

KMC simulations are natural choice for the spatial and temporal evolution of adatom islands, molecules and reaction kinetics on surfaces. One of the main issues in such simulations is incompleteness of the processes and their rates for the system under study. To addresses the issue of incompleteness, we have developed and applied a new pattern recognition scheme used in conjunction with KMC simulations (SLKMC-II) to study adatom islands diffusion on surfaces.

Using SLKMC simulations for the coarsening of Ag islands on Ag(111) surface (chapter 3), we have shown that during early stages, coarsening proceeds as a sequence of selected island sizes, creating peaks and valleys in the island-size distribution which is independent of initial conditions and results from the formation of kinetically stable islands (These islands have shapes with a closed-shell structure - one in which every atom on the periphery has at least three nearest neighbors) for certain sizes as dictated by the relative energetics of edge

atom detachment/attachment processes together with the large activation barrier for kink detachment.

In chapter 4, we have shown that the new pattern recognition scheme (used in SLKMC-II) that takes into account both fcc and hcp adsorption sites (top sites are included in the pattern recognition), enables us to find all possible processes and their energetics, including those such as shearing, reptation and concerted gliding, which may involve fcc to fcc, hcp to hcp and fcc to hcp moves, automatically during simulations (SLKMC-II). A systematic study of the self-diffusion (chapter 5) of small 2D islands (Ni, Ag and Cu), consisting of up to 10 - atoms, on fcc(111) surface using SLKMC-II show that, the small islands diffuse primarily via concerted motion. The effective activation energy barriers obtained from the Arrhenius plots of the diffusion coefficients show an almost linear increase with the island size.

Next, using DFT total energy calculations for Ni-Au nanoclusters (chapter 6.3), we show that it is energetically more favorable for CO to adsorb to the surface Ni atom than to the Au atom with Ni inside the nanocluster. This suggests that there is a thermodynamic driving force in the presence of CO and as a result of that Ni diffuses to the surface of Ni-Au nanocluster in the presence of CO on the surface. We confirm this by *ab initio* molecular dynamics simulations.

Our results (chapter 6.4) for the case of CH_3O on Pt-Au nanoclusters and Au(111), Pt(111) and AuPt(111) suggests that CH_3O binds more strongly to Au atom both in the case of Pt-Au nanoclusters and Au modified AuPt(111) surface, than to pure Au and pure Pt nanoclusters and surfaces. Our results for DOS suggests that accumulation of more states near the fermi level for the case of Au modified AuPt(111) surface is responsible for the strong binding of CH_3O to the Au atom in Au modified AuPt(111) surface. Different than Ni-Au nanoclusters with CO case, it is not energetically favorable for CH_3O to bind to Pt atom in Pt-Au nanoclusters and Pt atom surrounded by Au atom in AuPt(111) surface. Our further investigations for the dissociation of CH_3O to CO on Pt-Au nanoclusters suggests that highest barrier is 1.29 eV for the step CHO $\rightarrow$ CO+H. Hence we conclude that strong adsorption of CH_3O to the Au atom in Pt-Au nanoclusters followed by its dissociation to CO might induce diffusion of Pt atom to the surface of the Pt-Au nanoparticles, as it is energetically more favorable for CO to adsorb to a surface Pt atom in the Pt-Au nanocluster.

Finally, our DFT+KMC investigation (chapter 7) of NH_3 oxidation on $RuO_2(110)$ surface under UHV conditions suggests that NO is the dominant product at or above the peak NO desorption temperature. In contrast, ambient KMC results suggests that N_2 (upto 60 %) is the dominant product. The rationale for this is the secondary reaction of NO in ambient pressure i.e. active formation and decomposition of N_2O to N_2, owing to sufficient supply of N species, which is a result of active NH_x decomposition by plenty of O species on $RuO_2(110)$ surface. This study has demonstrated that simple estimation of selectivity

based on energetics may not be reliable. Prediction of selectivity requires consideration of competition of all reaction processes rather than individual processes, thus requiring kinetic simulations such as KMC.

8.2 Future Directions

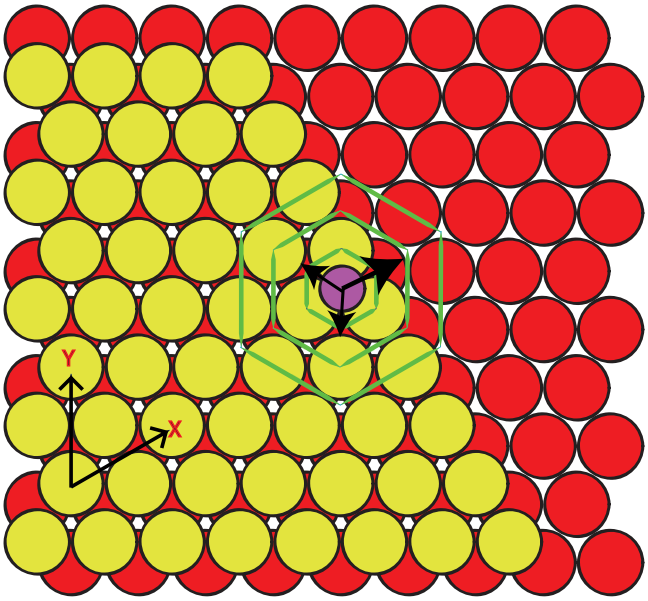

Figure 8.1 Grouping different sites into hexagonal rings on the fcc(111) surface in 3-D

3-D offlattice pattern recognition, as described in Ref [52], can be used to study 2-D hetero-epitaxial as well as 3-D systems, but at the cost of huge computational complexity.

Instead, the 2-D pattern-recognition scheme reported here can be used for, hetero diffusion (for systems with slight mismatch) as well as for 3-D homo epitaxial growth. Similarly more rings can be added to the pattern recognition scheme to include bridge sites as well that will make more suitable for hetero-epitaxial systems. Although this approach would increase computational expense because more rings would be required in order to identify the neighborhood than are required for distinguishing between fcc and hcp occupancy, it would still be faster than carrying out offlattice KMC simulations. We have already included 3-D capability to our 2-D pattern recognition scheme (see Figure 8.1).

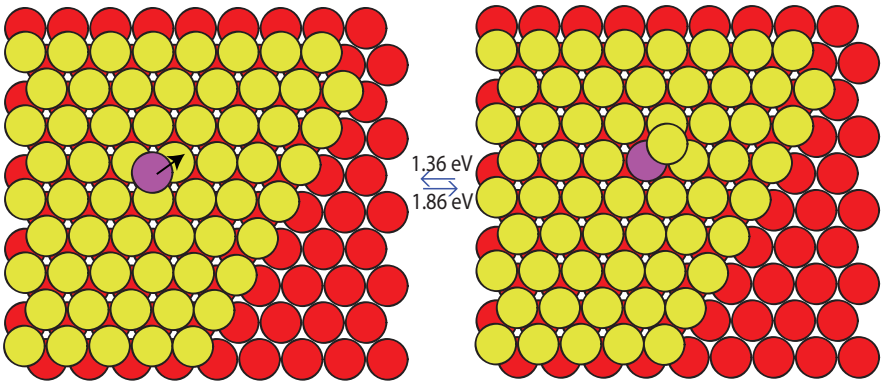

Figure 8.2 Example of exchange process in the case of Cu/Ni(111) surfac. Energy barriers are from spin polarized DFT (CI-NEB) calculations.

We are currently testing it for SLKMC simulations of growth of Cu/Ni(111) surface. Finally, we note that the idea behind the scheme we have described for the study of self-

diffusion on fcc(111) surfaces can be adapted to the study of other surfaces namely (110) and (100).

LIST OF REFERENCES

[1] A. Karim, A. N. Al-Rawi, A. Kara, T. S. Rahman, O. Trushin, and T. Ala-Nissila, Phys. Rev. B **73**, 165411 (2006).

[2] A. B. Bortz, M. H. Kalos, and J. L. Lebowitz, J. Comput. Phys. **17**, 10 (1975).

[3] G. H. Gilmer, J. Crystal. Growth. **35**, 15 (1976).

[4] A. F. Voter, Phys. Rev. B **34**, 6819 (1986).

[5] P. A. Maksym, Semiconf. Sci. Technol. **3**, 594 (1988).

[6] K. A. Fichthorn and W. H. Weinberg, J. Chem. Phys. **95**, 1090 (1991).

[7] J. L. Blue, I. Beichl, and F. Sullivan, Phys. Rev. E **51**, R867 (1995).

[8] G. Henkelman and H. Jónsson, J. Chem. Phys. **115**, 9657 (2001).

[9] G. M. H. Jónsson and K. W. Jacobsen, *Classical and Quantum Dynamics in Condensed Phase Simulations* (World Scientific, Singapore, 1998).

[10] O. Trushin, A. Karim, A. Kara, and T. S. Rahman, Phys. Rev. B **72**, 115401 (2005).

[11] G. Nandipati, Y. Shim, J. G. Amar, A. Karim, A. Kara, T. S. Rahman, and O. Trushin, J. Phys.: Condens. Matter **21** (2009).

[12] G. Nandipati, A. Kara, S. I. Shah, and T. S. Rahman, J. Phys.: Condens. Matter **23**, 262001 (2011).

[13] J. Repp, G.Meyer, K. H. Rieder, and P. Hyldgaard, Phys. Rev. Lett. **91**, 206102 (2003).

[14] C. M. Chang, C. M. Wei, and S. P. Chen, Phys. Rev. Lett. **85**, 1044 (2000).

[15] A. T. Samuel, H. Wei, C. R. Christopher, S. R. Jay, S. Syed Islamuddin, S. S. Ghazal, T. Volodymyr, S. R. Talat, and A. C. Donna, J. Phys. Chem. C **115**, 11112 (2011).

[16] J. Perez-Ramirez, N. Lopez, and E. V. Kondratenko, Journal of Physical Chemistry C **114**, 16660 (2010).

[17] Y. Wang, K. Jacobi, W. D. Schne, and G. Ertl, The Journal of Physical Chemistry B **109**, 7883 (2005).

[18] S. Hong, A. Karim, T. S. Rahman, K. Jacobi, and G. Ertl, Journal of Catalysis **276**, 371 (2010).

[19] S. I. Shah, G. Nandipati, A. Kara, and T. S. Rahman, J. Phys.: Condens. Matter **24**, 354004 (2012).

[20] S. Syed Islamuddin, N. Giridhar, K. Abdelkader, and R. Talat. S, Phys. Rev. B **88**, 035414 (2013).

[21] P. Hohenberg and W. Kohn, Phys. Rev. **136** (1964).

[22] M. S. Daw and M. I. Baskes, Phys. Rev. B **29**, 6443 (1984).

[23] D. R. Hartree, Proc. R. Soc. London **621**, A113 (1928).

[24] J. C. Slater, Phys. Rev. **81**, 385 (1951).

[25] V. Fock, Z. Phys. **61**, 126 (1930).

[26] L. H. Thomas, Proc. Cambridge Philos. Soc. **32**, 542 (1927).

[27] E. Fermi, Z. Phys. **48**, 73 (1928).

[28] P. A. M. Dirac, Proc. Cambridge Philos. Soc. **26**, 376 (1930).

[29] S. M. Foiles, M. I. Baskes, and M. S. Daw, Phys. Rev. B **33**, 7983 (1986).

[30] G. H. Vineyard, J. Phys. Chem. Solids **3**, 121 (1957).

[31] G. Henkelman and H. Jnsson, J. Chem. Phys **113**, 9978 (2000).

[32] G. Henkelman, P. U. Blas, and J. Hannes, J. Chem. Phys **113**, 9901 (2000).

[33] G. Henkelman and H. Jonsson, J. Chem. Phys **111**, 7010 (2000).

[34] D. Johnson, *Kinetic Monte Carlo: Bare Bones and a Little Flesh* (Computational Materials Science Summer School, 2001).

[35] W. Ostwald, Z. Phys. Chem. **37**, 385 (1901).

[36] K. Morgenstern, G. Rosenfeld, and G. Comsa, Phys. Rev. Lett. **76**, 2113 (1996).

[37] K. Morgenstern, G. Rosenfeld, E. Laegsgaard, F. Besenbacher, and G. Comsa, Phys. Rev. Lett. **80**, 556 (1998).

[38] A. Kara, O. Trushin, H. Yildirim, and T. S. Rahman, J. Phys.: Condens. Matter **21** (2009).

[39] G. Henkelman and H. Jónsson, Phys. Rev. Lett. **90**, 116101 (2003).

[40] F. Montalenti, Surf. Sci. **543**, 141 (2003).

[41] H. Yildirim, A. Kara, and T. S. Rahman, Phys. Rev. B **76**, 165421 (2007).

[42] G. Nandipati, A. Kara, S. I. Shah, and T. S. Rahman, (to be published) (????).

[43] K. Morgenstern, G. Rosenfeld, and G. Comsa, Surf. Sci. **441**, 289 (1999).

[44] E. Hristova, V. G. Grigoryan, and M. Springborg, Surf. Sci **603**, 3339 (2009).

[45] H. Yildirim, A. Kara, S. Durukanoglu, and T. S. Rahman, Surf. Sci. **600**, 484 (2005).

[46] V. Chirita, E. P. Munger, J. Greene, and J.-E. Sundgren, Surf. Sci. **436**, L641 (2012).

[47] J. C. Hamilton, M. S. Daw, and S. M. Foiles, Phys. Rev. Lett. **74**, 2760 (1995).

[48] S. C. Wang and G. Ehrlich, Surf. Sci. **239**, 301 (1990).

[49] K. Kyuno and G. Ehrlich, Surf. Sci. **437** (1999).

[50] S. Li and H. Metiu, Surf. Sci. **359**, 245 (1996).

[51] S. I. Shah, G. Nandipati, A. Kara, and T. S. Rahman (to be published).

[52] G. Nandipati, A. Kara, S. I. Shah, and T. S. Rahman, J. Comput. Phys. **231**, 3548 (2012).

[53] G. Antczak and G. Ehrlich, *Surface Diffusion : metals, metal atoms and clusters* (Cambridge University Press, 2010).

[54] A. Zangwill, *Physics at Surfaces* (Cambridge University Press, 1988).

[55] E. Kaxiras, Comput. Mater. Sci **6**, 158 (1996).

[56] D. W. Bassett, J. Phys. C **9**, 2491 (1976).

[57] T. T. TSong and R. Casanova, Phys. Rev. B **22**, 4632 (1980).

[58] S. C. Wang and G. Ehrlich, Surf. Sci. **239**, 301 (1990).

[59] S. C. Wang and G. Ehrlich, Phys. Rev. Lett. **68**, 1160 (1992).

[60] S. C. Wang, U. Kurpick, and G. Ehrlich, Phys. Rev. Lett. **81** (1998).

[61] G. L. Kellogg, Appl. Surf. Sci. **67**, 134 (1993).

[62] J. M. Wen, S.-L. Chang, J. W. Burnett, J. W. Evans, and P. A. Thiel, Phys. Rev. Lett. **73**, 2591 (1994).

[63] W. W. Pai, A. K. Swan, Z. Zhang, and J. F. Wendelken, Phys. Rev. Lett. **79**, 3210 (1997).

[64] M. Giesen and H. Ibach, Surf. Sci. **529**, 135 (2003).

[65] M. Giesen, G. S. Icking-Konert, and H. Ibach, Phys. Rev. Lett. **80**, 552 (1998).

[66] J. Fern, L. Gmez, J. M. Gallego, J. Camarero, J. E. Prieto, V. Cros, A. L. V. de Parga, J. J. de Miguel, and R. Miranda, Surf. Sci. **459**, 135 (2000).

[67] H. A. V. der Vegt, J. Alvarez, X. Torrelles, S. Ferrer, and E. Vlieg, Phys. Rev. B **52**, 17443 (1995).

[68] C. Busse, C. Polop, M. Muller, K. Albe, U. Linke, and T. Michely, Phys. Rev. Lett. **91**, 056103 (2003).

[69] M. Muller, K. Albe, C. Busse, A. Thoma, and T. Michelyi, Phys. Rev. B **71**, 075407 (2005).

[70] C. L. Liu and J. B. Adams, Surf. Sci. **268**, 73 (1992).

[71] R. T. Tung and W. R. Graham, Surf. Sci. **97**, 73 (1980).

[72] T. Y. Fu and T. T. Tsong, Surf. Sci. **454-456**, 571 (2000).

[73] P. G. Flahive and W. R. Graham, Surf. Sci. **91**, 449 (1980).

[74] C. L. Liu, J. M. Cohen, J. B. Adams, and A. F. Voter, Surf. Sci. (1991).

[75] B. M. Rice, C. S. Murthy, and B. C. Garrett, Surf. Sci. **276**, 226 (1992).

[76] P. Stoltze, J. Phys.: Condens. Matter **6**, 9495 (1994).

[77] Y. Li and A. E. DePristo, Surf. Sci. **351**, 189 (1996).

[78] J. J. Mortensen, B. Hammer, O. H. Nielsen, K. W. Jacobsen, and J. K. Norkov, *Elementary Processes in Excitations and Reactions on Solid Surfaces* (Springer-Verlag, Berlin, 1996), chap. Density functional theory study of self-diffusion on the (111) surfaces of Ni, Pd, Pt, Cu, Ag and Au, pp. 173–182.

[79] K. Haug and T. Jenkins, J. Phys. Chem. B **104**, 10017 (2000).

[80] U. Kurpick, Phys. Rev. B **64**, 075418 (2001).

[81] H. Bulou and C. Massobrio, Phys. Rev. B **205427** (2005).

[82] S. Y. Kim, I.-H. Lee, and S. Jun, Phys. Rev. B **74**, 073412 (2006).

[83] A. Karim, A. Kara, O. Trushin, and T. S. Rahman, J. Phys:. Condens. Matter **23**, 462201 (2011).

[84] S. I. Shah, G. Nandipati, and T. S. Rahman (to be published).

[85] G. Kresse, Phys. Rev. B **54**, 11169 (1996).

[86] G. Kresse and D. Joubert, Phys. Rev. B **59**, 1758 (1999).

[87] P. E. Blöchl, Phys. Rev. B. **50**, 17953 (1994).

[88] J. P. Perdew, K. Burke, and M. Ernzerhof, Phys. Rev. Lett. **77**, 3865 (1996).

[89] P. W.H., *Numerical recipes : the art of scientific computing.* (Cambridge Cambridgeshire, New York: Cambridge University Press., 1986).

[90] V. Chirita, E. P. Munger, J. E. Greene, and J.-E. Sundgren, Thin Solid Films **370**, 179 (2000).

[91] V. Chirita, E. P. Munger, J. E. Greene, and J.-E. Sundgren, Surface Science **436**, L641 (1999).

[92] A. Einstein, Ann. Phys. (Leipzig) **17**, 549 (English transl. Investigations on the Theory of Brownian Movement, Dover, New York, 1956) (1905).

[93] M. Haruta, T. Kobayashi, H. Sano, and N. Yamada, Chemistry Letters p. 405 (1987).

[94] M. Valden, X. Lai, and D. W. Goodman, Science **281**, 1647 (1998).

[95] M. Haruta, CATTECH **6**, 102 (2002).

[96] J. A. Rodriguez, Surf. Sci. Rep. **24**, 233 (1996).

[97] J. H. Sinfelt, Acc. Chem. Res. **10**, 15 (1977).

[98] J. H. Sinfelt, *Bimetallic Catalysts. Discoveries, Concepts, and Applications* (John Wiley and Sons, New York, 1983).

[99] J. A. Rodriguez and D. W. Goodman, J. Phys. Chem. **95**, 4196 (1991).

[100] D. W. Yuan, Y. Wang, and Z. Zeng, J. Chem. Phys. **122**, 114310 (2005).

[101] H. T. Chen, J. G. Chang, u. S. P. J, and H. L. Chen, J. Comput. Chem. **31**, 258 (2010).

[102] H. Itoh, Jpn. J. Appl. Phys. **16**, 2125 (1977).

[103] X. Qing, Guo andChenbiao, R. Zefeng, W. Yang, M. Zhibo, D. Dongxu, F. Hongjun, K. M. Timothy, and Y. Xueming, J. Am. Chem. Soc. **134**, 13366 (2012).

[104] I. Hakim, g. Serdar, D. B. Nigel, and M. D. Mark, Surf. Sci. **72**, 081407(R) (2005).

[105] G. Ertl, H. Knozinger, and J. Weitkamp, *Handbook of. Heterogeneous Catalysis* (A Wiley, 1999).

[106] H. Over, Chem. Rev **112**, 3356 (2012).

[107] A. P. Seitsonen, D. Crihan, M. Knapp, A. Resta, E. Lundgren, J. N. Andersen, and H. Over, Surface Science **603**, L113 (2009).

[108] C. C. Wang, Y. J. Yang, J. C. Jiang, D. S. Tsai, and H. M. Hsieh, J Phys Chem C **113**, 17411 (2009).

[109] H. Wang and W. F. Schneider, Catalysis Today **165**, 49 (2011).

[110] C. C. Wang, Y. J. Yang, and J.-C. Jiang, The Journal of Physical Chemistry C **114**, 2816 (2009).

[111] C. C. Wang, Y. J. Yang, J. C. Jiang, D. S. Tsai, and H. M. Hsieh, The Journal of Physical Chemistry C **113**, 17411 (2009).

[112] F. Hess, P. P. T. Krause, S. F. Rohrlack, J. P. Hofmann, A. Farkas, and H. Over, Surface Science **606**, L69 (2012).

[113] K. Reuter, D. Frenkel, and M. Scheffler, Phys. Rev. Lett. **93**, 116105 (2004).

[114] A. Farkas, F. Hess, and H. Over, The Journal of Physical Chemistry C **116**, 581 (2011).

[115] D. Vanderbilt, Physical Review B **41**, 7892 (1990).

[116] G. Paolo, B. Stefano, B. Nicola, C. Matteo, C. Roberto, C. Carlo, C. Davide, L. C. Guido, C. Matteo, D. Ismaila, *et al.*, Journal of Physics:. Condensed Matter **21**, 395502 (2009).

[117] D. G. Truhlar, B. C. Garrett, and S. J. Klippenstein, The Journal of Physical Chemistry **100**, 12771 (1996).